TECHNISCHE UNIVERSITÄT WIEN

PhD Thesis

Molybdenum-based hard nitrides

carried out for the purpose of obtaining the degree of PhD submitted at TU Wien, Faculty of Mechanical and Industrial Engineering, by

DI Dipl.-Phys.Ing. Fedor F. Klimashin

Mat.Nr.: 1228994

Lassallestraße 10/12, 1020 Vienna, Austria

under the supervision of

Univ.Prof. Dipl.-Ing. Dr.mont. Paul Heinz Mayrhofer

Institute of Materials Science and Technology, E308

Vienna, March 2016

Diese Dissertation haben begutachtet

…… ……

This work was supported by the START Program (Y371) of the
Austrian Science Fund (FWF)

Affidavit

I declare in lieu of oath, that I wrote this thesis and performed the associated research myself, using only literature cited in this volume.

Date *Signature*

Моим маме, папе, и брату

Acknowledgements

What a time! I thank from the bottom of my heart for that three fantastic years:

The entire Institute of Materials Science and Technology and especially the entire ~~hard~~ exceptional coatings group, for creating a **magic** atmosphere, filled with **lovely** Austrian dialects, for teaching me skiing, giving every single day plenty of reasons to smile, gifting happy vivid memories!

Particularly Christian **Koller**, Matthias **Bartosik**, Jörg **Paulitsch**, Heribert **Marihart**, Robert **Hollerweger**, Wolfgang **Seidl**, Philipp **Ertelthaler**, Vincent **Moraes**, Stefan **Glatz**, Corinna **Sabitzer**, Helmut **Riedl**, Manfred **Schlögl**, Rainer **Hahn**, Pierre **Wiehoff**, Liangcai **Zhou**, Robert **Raab**, Bernhard **Kohlhauser**, Valentin **Dalbauer**, Elias **Aschauer**, Stefan **Fritze**, Thomas **Scheu**, Stefan **Rißlegger**, Christoph **Fuger**, Thomas **Glechner**, Alexander **Kirnbauer**.

The first-principle guys, Nikola **Kountá**, David **Holec**, Holger **Euchner** for slightly opening the "magic box" and delving into it for the answers, whenever I felt confused about experiments.

David **Holec**, for spending Thursday evenings hypothesizing, convincing, teaching, inspiring, and joking, often risking missing the last train to the fascinating Mon-tan land.

Holger **Euchner**, for the every-day fruitful discussions, for every single communication, for the words of wisdom.

Ylvi, who became a part of me over the past years and who I could rely on anytime, for working in close collaboration on this Thesis and paving the way for the enthralling research.

Paul **Mayrhofer**, for **nothing**! ;) For the live one-way video interview, for giving me a chance to coalesce with your group, for the encouraging teaching, for inspiring with discussions full of perspective insights, for electrifying with ideas. Permanently. For standing by for my two-minutes-to-deadline submissions, including the Thesis, naturally. For letting me made **Fedora**'s acquaintance – thanks to her my life became fairly harder, but not stiffer!

My friends, brother, papa, mama.

"Du hast schon Recht, die N-Leerstelle hat uns viel gelehrt, sie ist aber trotzdem eine Leerstelle"–
lehrte Prof. P. H. Mayrhofer

Table of contents

Abstract

Molybdenum-based cubic-structured nitrides are fascinating materials, predicted by empirical criteria (e.g. valence electron concentration, elastic constants G/B and C_{12}-C_{44}, ionic potential φ) and proved experimentally as self-lubricating hard coatings with improved toughness. The application area is restricted, however, to lower temperatures, since the weak chemical non-metal–metal bonds tend to break at 300–500 °C and, if exposed to an oxygen-containing atmosphere, the volatile MoO_3 can form. Cubic-structured molybdenum nitride is also difficult to synthesise due to its high sensitivity to the nitrogen content present. Hence, to the nitrogen partial pressure used during physical vapour deposition.

The cubic-structured γ-phase of the molybdenum nitride is the high-temperature allotropy of the tetragonal-structured β-phase. The use of non-equilibrium synthesising techniques such as magnetron sputtering allows, however, the deposition of metastable phases. The distinctive feature of the cubic γ-MoN_x, as compared to the majority of B1-structured transition metal nitrides, is the highly defected nitrogen sublattice, being 50% vacant. The experimental results – supported by *ab initio* calculations – suggest that increasing vacancy content at the nitrogen sublattice leads to the formation of coherent domains with high Mo-content (where the interstitial sites are vacant), while decreasing vacancy content at the nitrogen sublattice leads to the formation of coherent domains with partially ordered pseudo-cubic γ'-Mo_3N_2 (actually γ'-$MoN_{0.67}$, where 1/3 of the nitrogen sublattice is vacant). The slightly overstoichiometric γ-$MoN_{0.53}$ (as revealed by elastic recoil detection analysis) was found to exhibit the highest indentation hardness ~33 GPa, which decreases to 28 GPa, when the vacancy content is reduced and partially ordered pseudo-cubic γ'-$MoN_{0.67}$ developed.

To extend the temperature range and further improve the properties of γ-MoN_x-based materials, ternary Mo–Cr–N and Mo–Al–N alloys were developed. Both elements, chromium and aluminium, are well known to significantly improve the oxidation resistance through the formation of dense oxide scales Al_2O_3 or Cr_2O_3, preventing or significantly reduce further metal (e.g., Mo) outward and oxygen inward diffusion.

For the ternary Mo–Cr–N coatings, the nitrogen partial pressure used during magnetron sputtering is crucial to allow the synthesis of single-phase cubic-structured solid solutions along the entire Mo–Cr composition. For a narrow nitrogen partial pressure window, the solid solution follows the $MoN_{0.5}$–CrN quasi-binary tie line and, thus, forms a continuous cubic-structured solid solution. The chemical formula along this tie line can be described with Mo_{1-}

$_x$Cr$_x$N$_{0.5(1+x)}$, indicating that for every vacancy at the nitrogen sublattice that is populated with nitrogen, we need to substitute two Mo-ions with Cr-ions at the metal sublattice. However, high nitrogen partial pressures during deposition favour the formation of fully occupied N-sublattice, Mo$_{1-x}$Cr$_x$N, leading to decreased mechanical properties. The highest hardnesses within the Mo–Cr–N are obtained for coating fcc-Mo$_{0.81}$Cr$_{0.19}$N$_{0.52}$ with ~34 GPa.

The development of ternary Mo–Al–N coatings was guided and accompanied by *ab initio* investigations. These again show the determining role of vacancies at the nitrogen sublattice to form cubic-structured Mo$_{1-x}$Al$_x$N$_y$ solid solutions. Without vacancies at the nitrogen sublattice – i.e., along the MoN–AlN quasi-binary tie line – the hexagonal-structured h-Mo$_{1-x}$Al$_x$N is energetically favoured across the entire concentration range of *x*. Only with the aid of vacancies at the nitrogen sublattice the cubic structure Mo$_{1-x}$Al$_x$N$_y$ solid solutions become energetically favourable up to a threshold Al-concentration. This threshold is at x ≈ 0.45 for compositions along the MoN$_{0.5}$–AlN quasi-binary tie line, and at x ≈ 0.65 for compositions along the MoN$_{0.5}$–AlN$_{0.5}$ quasi-binary tie line, where the nitrogen sublattice is only half populated always. Based on these *ab initio* calculations, we were able to synthesise single-phase cubic-structured Mo$_{1-x}$Al$_x$N$_y$ solid solutions up to x = 0.57 – currently the highest Al-content reported. This coating, Mo$_{0.43}$Al$_{0.57}$N$_{0.80}$ – with a composition close to the MoN$_{0.5}$–AlN quasi-binary tie line (i.e., Mo$_{1-x}$Al$_x$N$_{0.5(1+x)}$) – exhibits with 38 GPa also the highest hardness among all Mo-Al-N coatings studied. Again, the nitrogen partial pressure used during deposition plays the determining role for combining the cubic structure and high Al content. As soon as the hexagonal phase forms, for too high nitrogen partial pressures or Al contents, the hardness drastically decreases to ~22 GPa.

The knowledge gained during the investigation and development of the binary MoN$_y$ and the ternaries Mo$_{1-x}$Cr$_x$N$_y$ and Mo$_{1-x}$Al$_x$N$_y$, allowed the development of quaternary Al-rich (x = 0.5 or even 0.6 depending on the Cr-content) single-phase cubic-structured fcc-Mo$_{1-x-y}$Al$_x$Cr$_y$N$_z$ coatings with hardnesses above 40 GPa. Particularly, fcc-Mo$_{0.39}$Al$_{0.52}$Cr$_{0.09}$N$_{0.98}$ exhibits the highest hardness, *H*, of ~41 GPa among all coatings studied. The combination with a relatively low indentation modulus, *E*, allows for low *H*/*E*- and H^3/E^2–ratios (0.1 and 0.35, respectively). These empirical criteria – related with the elastic strain to failure and resistance to the plastic deformation, respectively – suggest for excellent wear protection and a high potential for severe applications.

Summarizing, the combining of experimental and computational materials science provides deeper insights into the complex nature of the substoichiometric nitrides (nitrogen/metal-ratio < 1). Especially the development of Mo-based nitride materials requires a knowledge-driven tuning of the deposition process, due to the determining role of the nitrogen vacancies (and vacancies in general). The study clearly shows that the understanding of atomic scale processes is needed for the development of new high-performance materials.

Kurzfassung der Dissertation

Im Rahmen der vorliegenden Dissertation wurden neue unterstöchiometrische Molybdän-basierende Mehrkomponentennitride entwickelt. Hier wurde besonderes Augenmerk auf die fundamentale Erforschung der atomaren Zusammenhänge zwischen Phasenbildung und mechanischen Eigenschaften gelegt. Molybdännitride im Speziellen und unterstöchiometrische Nitride generell, sind gegenwärtig noch wenig erforschte Materialien, denen aber eine große Bedeutung in den immer herausfordernderen industriellen Anwendungen zugeschrieben werden.

Molybdännitrid mit kubischer NaCl-Kristallstruktur ist eine faszinierende Nitridkeramik mit hervorragenden Eigenschaften. Im Gegensatz zu den meisten kubisch strukturierten Übergangsmetallnitriden kristallisiert Mo–N mit 50% Leerstellen am Stickstoff-Untergitter, γ-$MoN_{0.5}$. Die Eigenschaften von Mo-N werden sehr stark vom Stickstoffgehalt und folglich vom N_2-Partialdruck während des Magnetron Sputterns (der verwendeten Phyiscal Vapour Deposition (PVD) Beschichtungstechnik für diese Arbeit) beeinflusst. Die thermische Stabilität von Mo-N ist durch Aufbrechen der Mo–N-Bindungen bei Temperaturen bereits unter 500 °C stark limitiert. Außerdem bildet sich sehr leicht das flüchtige MoO_3-Oxid. Deshalb ist es entscheiden welchen Einfluss die Leerstellen sowie weitere Legierungselemente (wie vor allem Al und Cr) auf die Phasenentwicklung und die damit einhergehenden Änderungen der mechanischen Eigenschaften der MoN_x-basierenden PVD-Schichten ausüben. Das Hauptaugenmerk wurde dabei auf die Herstellung der einphasigen kubischen Strukturen gerichtet, die in der Regel bessere mechanische Eigenschaften und Oxidationsbeständigkeit aufweisen. Basierend auf den Ergebnissen der Berechnungen mittels Dichtefunktionaltheorie und den experimentellen Untersuchungen sind zwei wichtige Punkte hervorzuheben:

A. Die Schlüsselrolle der Stickstoffleerstellenkonzentration

Der Existenzbereich des einphasigen kubischen γ-MoN_x reicht von ~20 bis 34 at.% N (x = 0.33 – 0.53) und zeigt somit die Neigung zur Bildung der unterstöchiometrischen Nitride. Die weitere Besetzung der N-Leerstellen in γ-MoN_x (x > 0.53) führt zu einer partiellen Ordnung im Stickstoffuntergitter und zur Bildung von kohärenten Domänen der weitgehend unerforschten pseudokubischen γ‘-MoN_x-Phase. Die *ab initio* berechnete Bildungsenergie von γ‘-MoN_x deutet darauf hin, dass γ‘-MoN_x einen sehr engen Existenzbereich hat (sozusagen eine Strichphase ist) und als γ‘-$MoN_{0.67}$ betrachtet werden kann (demnach eine 3:2 Stöchiometrie besitzt). Zwar ist

die resultierende Stöchiometrie in beiden Fällen dieselbe (3:2), allerdings bildet sich γ'-$MoN_{0.67}$ ausschließlich mit Leerstellen am Stickstoffuntergitter (mit ~33% Leerstellen, die geordnet sind) und **nicht** mit Leerstellen in beiden Untergittern (mit jeweils 25% und 50% Leerstellen im Metall- und Stickstoffuntergitter, Mo_3N_2), wie ursprünglich vermutet.

Beim Legieren von γ-$MoN_{0.5}$ mit *Me*N (*Me* = Cr, Al) erfolgt die Entwicklung der Elementzusammensetzung im Einklang mit dem quasibinären Schnitt $MoN_{0.5}$–*Me*N, der mit $Mo_{1-x}Cr_xN_{0.5(1+x)}$ zu beschreiben ist. Folglich müssen für jede Stickstoffleerstelle, die mit N gefüllt wird, zwei Mo-Ionen mit zwei Cr- oder Al-Ionen substituiert werden. Bei der Herstellung mittels PVD ist äußerste Sorgfalt hinsichtlich des verwendeten N_2-Partialdruck notwendig, da bei zu hohen Partialdrücken das Stickstoffuntergitter, vor allem bei höheren Cr-Gehalten, sehr schnell vollgefüllt wird, wodurch sich die mechanischen Eigenschaften verschlechtern.

Die ausgewählten Legierungselemente, Cr und Al, bewirken ein unterschiedliches Verhalten. Im Gegensatz zum kubischen CrN, welches eine vollständige Löslichkeit mit dem kubischen γ-$MoN_{0.5}$ erlaubt, kann AlN (das eigentlich hexagonal kristallisieren möchte) nur bis zu einem gewissen Anteil in der γ-$MoN_{0.5}$-Phase unter Bildung von fcc-$Mo_{1-x}Al_xN_y$ gelöst werden. Unsere Dichtefunktionaltheorie Berechnungen zeigen, steht die maximale Löslichkeit von Al in fcc-$Mo_{1-x}Al_xN_y$ direkt mit der vorhandenen Stickstoff-Leerstellenkonzentration verbunden ist. Desto höher die Konzentration der Stickstoffleerstellen ist, desto mehr Al kann die fcc-$Mo_{1-x}Al_xN_y$-Phase aufnehmen. Damit ist es uns auch experimentell gelungen, bis zu ~57 at.% Al am Metalluntergitter innerhalb der kubischen Phase zu lösen, fcc-$Mo_{0.43}Al_{0.57}N_{0.80}$. Dies stellt den bisher höchsten Al-Gehalt in fcc-$Mo_{1-x}Al_xN_y$ dar, bei noch höheren Al-Gehalten bildet sich die auf hexagonalem AlN-basierende Phase aus.

Die gewonnenen Ergebnisse aus den ternären Mo–Cr–N und Mo–Al–N Systemen ermöglichte die Entwicklung von einphasigen kubisch flächenzentrierten quaternären Mo–Al–Cr–N-Schichten. Auch hier unterliegt die Besetzung der Stickstoffleerstellen der Abhängigkeit entlang der quasibinären Schnitte $MoN_{0.5}$–*Me*N, d.h. fcc-$Mo_{1-x-y}Al_xCr_yN_{0.5(1+x+y)}$. Die maximale Al-Löslichkeit, *x*, in fcc-$Mo_{1-x-y}Al_xCr_yN_z$, variiert (je nach Cr-Gehalt) zwischen 0.5 und 0.6.

B. Die maßgeschneiderten mechanischen Eigenschaften

Basierend auf den Dichtefunktionaltheorie Berechnungen und den experimentellen Ergebnissen lässt sich schließen, dass der maximale Al-Gehalt in kubischen γ-MoN_x-basierenden Schichten des Mo–Al–Cr–N-Stoffsystems mit einer maximal möglichen Konzentration an Stickstoffleerstellen einhergeht. Die mechanischen Eigenschaften von $Mo_{1-x-y}Al_xCr_yN_{0.5(1+x+y)}$ Schichten, wie z.B. Härte, *H*, erreichen ein Maximum wenn die Schichten einphasig kubisch kristallisieren, und neben einem maximalen Al-Gehalt auch geringe Mengen an Chrom enthalten. Die höchsten Härtewerte der binären, ternären und quaternären Schichten wurden mit 33 GPa für γ-$MoN_{0.53}$, 34 GPa für fcc-$Mo_{0.81}Cr_{0.19}N_{0.52}$, 38 GPa für fcc-$Mo_{0.43}Al_{0.57}N_{0.80}$ und 41 GPa für fcc-$Mo_{0.39}Al_{0.52}Cr_{0.09}N_{0.98}$ erreicht. Die Kombination mit moderaten Elastizitätsmoduli, *E*, erlaubt auch ausgezeichnete H/E- oder H^3/E^2-Kriterien, die unseren γ-MoN_x-basierenden Schichten ausgezeichnete Bruchzähigkeit und tribologische Eigenschaften attestieren, die sie für viele anspruchsvolle Anwendungsbereiche auszeichnen.

Introduction

The constantly growing demands for higher cutting speeds in the machining industry and resulted temperature growth in the contact zone between cutting tool and work piece up to 1000 °C (and even above) raise continuously the requirements to protective coatings for hard metal cutting tool. The highly stable and inert nitrides of transition metals (materials with developed metallic, covalent, and ionic characters) and especially single-phase cubic-structured solid solution $Ti_{1-x}Al_xN$, which also became a model system in fundamental investigations of the transition metal nitrides, are extensively used in the industry over the past decades. Our developed fascinating molybdenum-based cubic-structured hard nitrides (also predicted by empirical criteria to exhibit improved toughness and tribological properties) present a very promising alternative to $Ti_{1-x}Al_xN$.

Combining computational and experimental materials science, we have carried out comprehensive investigations on the γ-$MoN_{0.5}$-based coatings, using aluminium and chromium as alloying elements due to their ability to improve oxidation resistance and thermal stability. Besides the industry-oriented aspects, our study attracts a great attention from the viewpoint of fundamental research, since not so many reports exist on the effect of substoichiometry for nitrides.

We have started investigating the impact of vacancies and vacancy ordering on the evolution of phase composition and mechanical properties of binary (γ cubic-structured) MoN_x (see **Publication #1**). Alloying with chromium, we put the main emphasis on population of inherent structural vacancies in MoN_x at different nitrogen partial pressures used during deposition and the accompanied composition-induced alteration of mechanical properties of these mutually soluble VI group TMNs (see **Publication #2**). Alloying with aluminium, we studied the correlation between maximum aluminium solubility in the cubic structure and nitrogen vacancy as well as related changes in mechanical properties (see **Publication #3**). Finally, governed by the accumulated knowledge, we were aiming at synthesising Al-rich super-hard quaternary Mo–Al–Cr–N coatings (see **Publication #4**). Additionally, inspired by the power of nothing, we fused two materials with inherent driving force to crystallize with vacancies on different sublattices, γ-MoN_x and δ-Ta_xN, and investigated complex development of structure and related mechanical properties, combining experiments and *ab initio* calculations (see **Publication #5**).

1. Theoretical background

1.1. The billion dollar industry – thin film coatings

Surface engineering, and particullaly thin film coatings technology, is a constantly growing industry, which is aimed at improving material performance and efficiency. Its value added growth continuously and exceeds, for instance, in Germany $20 billion per annum [1], which corresponds to ~0.5% of GDP in 2014 [2]. Generally and in more specific cases, the global market exceedes, e.g., $7.5 billion alone for optical thin films (2010) or $8 billion for thin film solar panels (as estimated by 2030) [3], where the global market for only PVD-produced coatings is $0.7 billion (2010) [1] (note that Asian market is hard to estimate). Such high market values are evidentely accomponaied by the high investments in the research and development sector of the surface engineering, e.g. the expenditures of the United States Department of Energy and China exceed $24 and $10 billion, respectively [3].

Particularly, such high investments are a result of economic hardships of the developed countries, described in "Damit Rost und Verschleiß nicht Milliarden fressen" (literally "so that wear and rust do not eat the billions") [1, 4]. According to this statistic, friction and wear cause the costs to the tune of 1-2% of GDP, i.e., hurt the national economics of USA to $150-350 billion, China – $100-200, Germany – $40-80 billion, Russia – $20-40 billion, Austria – $5-10 billion, (2014) [2]. Moreover, the use of the health-endangering lubricants, which utilization costs inflate the expenses up to 400% of the tool costs, is often not justified [5]. An even more unpleasant plague – corrosion – demands up to 4% of GDP [1], dobbling, hence, the upper limit of the damage coasts caused by friction and wear.

The use of the functional protective coatings contributes to an extraordinary costs reduction and productivity improvement. For instance, in the machining, and particularly cutting tool industry, a wear-resistant protective coatings can extend the tool life by a factor 3-8 [3], while the concept of self-lubricating coatings represents one of the successful pathways to the dry machining, i.e., the renunciation of lubricants [6]. The understanding of the corrosion processes and the countermeasures against it promote the damage coast reduction by 30% [1].

1.2. Thin film deposition

There are a lot of possibilities to divide the bright spectrum of depositions techniques into groups. Generally, depending on, whether the reaction occurring is physical or chemical, one distinguishes between Physical Vapour Deposition (PVD) and Chemical Vapour Deposition (CVD) techniques. Both techniques (with an array of their variations) are currently widely used for deposition of functional coatings finding their application in various sectors of industry, for instance, machining, aerospace and automotive industries as well as decorative coatings and consumer goods. Each technique has its advantages as well as drawbacks.

The CVD technique stands out particularly due to the high pressure deposition (>1 mbar) and the coatings formation principle: chemicals in gaseous form (precursors) flow through the reaction chamber and react on or near the substrate's surface [7, 8]. In order to overcome the activation energy for this reaction substrate must be heated to high temperatures (700 - 1200 °C), which result in excellent adhesion, but significantly restrict the choice of substrate material at the same time. Other drawbacks are related to pollution through the reaction products and to the film growth with residual tensile stresses (0.1 - 0.4 GPa). The letter one is highly undesirable, for instance, for the interrupted machining. The benefits of the CVD technique are low process costs, large volume of the reaction chamber, uniformity of the coatings, high coating rate and possibility to deposit thick coatings (up to 15 - 20 µm).

Unlike CVD technique, a high vacuum is usually used during the PVD process [3, 7, 8]. Moreover, from the gas phase should be generated plasma. It causes the high process costs but allows applying low temperatures (200 - 500 °C) to the substrate as compared to the CVD method. The deposited films are characterized by the high residual compressive stress (0.1 - 0.4 GPa). The maximum thickness limited by approximately 5 µm. The resulting film properties such as hardness, density, adhesion to the substrate etc., strongly depend on the process parameters. For instance, a high bias voltage applied to the substrate contributes to formation of a dense structure, improves coating adhesion, but also causes substrate heating.

Among the wealth of particular deposition techniques, hereafter the emphasis is laid on PVD and specifically magnetron sputtering. According to the publication and patent databases [3], sputtering is the most popular PVD technique nowadays, applied on laboratory as well as industry scales. Magnetron Sputtering allows to sputter any material and control precisely the film chemical composition. The simplified sputtering process, similar to other PVD deposition techniques, involves three main steps: first, ejection of the cathode (target) material, followed by its transfer through the gaseous phase towards the substrate surface, where it finally condenses, forming a films. The process begins by generating the vacuum and introducing a working gas (usually argon) into the deposition chamber (schematically shown in Fig. 1a). The electrons, trapped by the magnetic field (Fig. 1b), collide with the working gas atoms, causing their ionisation. The positively charged Ar^+-ions become attracted by the negatively charged cathode material, accelerate towards its surface, and, if the energy is sufficient to break the atomic bonds, the target material becomes ejected (sputtered).

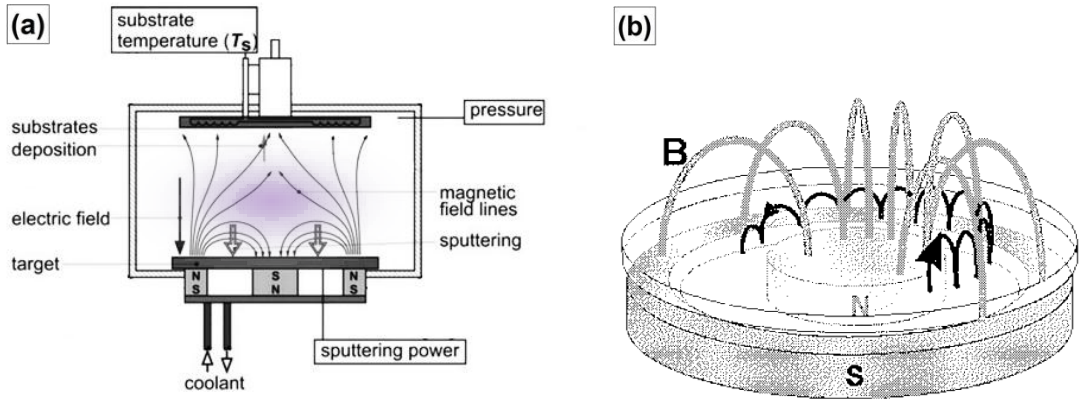

Fig. 1. Schematic illustration of an magnetron sputtering process (a) [9] and planar magnetron with the permanent magnets (b) [10], trapping the electrons (the path is indicated by the solid black line) and increasing the collision probability with the working gas in the vicinity of the target surface.

The measure of sputtering rate for different elements is the sputtering yield, *Y*, indicating the amount of the ejected (sputtered) target atoms pro one impinging Ar^+-ion (Figs. 2a and b).

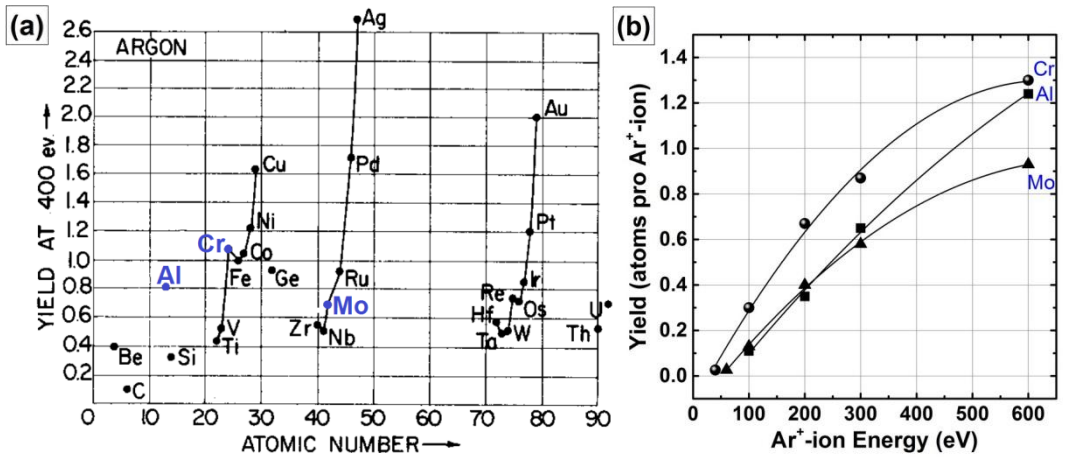

Fig. 2. Representative sputtering yield curves at 400 eV Ar^+ for 28 elements (a) as well as at Ar^+ varying from 50 to 600 eV for Al, Cr, and Mo based on the results of Laegreid [11]. The highlighted elements are of particular interest in the framework of the current thesis.

The target's surface bombardment (the interaction events are shown in Fig. 3a) is associated with momentum transfer process. About 10% energy of the impinging Ar^+-ions transforms to the kinetic energy of the sputtered species (atoms, molecules, clusters), which is comparable with (or even larger than) the bond energies. The energies of the sputtered species are, hence, in the order of magnitude of tenths of electron volts (10-40 eV [12]) – enormous amount of energy, roughly equal to 10^5 K of the thermal energy [3, 13]. Arriving on the substrate surface, heated usually to several hundred degrees Celsius, the sputtered particles experience the rapid cooling (10^{13} $K \cdot s^{-1}$ [14]) similar to the quenching process. The high kinetic energy of the sputtered particles transforms mainly to the heat, transported away by cooling. The adatom mobility and especially bulk diffusion are constrained by reduced temperatures and result, hence, often in formation of phases, which do not obey the tangent rule, e.g. high-temperature allotropic modification, and may form with an extended homogeneity range [12].

The adatom surface diffusion may be, however, controlled by the substrate temperature (homologous temperature, see chapter 1.2.).

If a reactive gas (nitrogen, oxygen) introduced into the deposition chamber, metal-non-metal compounds (nitrides, oxides) may be formed. Although the path of the sputtered species to the substrate and at low working/reactive gas pressures is nearly collisionless, reactive sputtering results ordinarily in lower deposition rates because of target the target poisoning effect, i.e., formation of the non-conductive compounds on the target surface [15].

Additionally to the briefly described main stages of sputtering process, it is important to take a little closer look at the interaction events happening on the surface-close regions on the target and substrate (see Figs. 3a and b). In general, most of the interaction events presented in Fig. 3a may also be applied to that occurring on the substrate surface during plasma etching (e.g. gas desorption or amorphisation, which is crucial for the microstructure during initial growth), or during deposition, though in a lesser extent, since kinetic energy of arriving sputtered species is less than a tenth of that of Ar^+-ions. High energetic Ar^+-ions can, however, contribute to the interaction effects, when applying a high bias voltage to the substrate (usually in the range 50-100V) and, hence, attracting them. Arriving sputtered particles with the energies of tenths of electron volts, 10-40 eV, result in a nearly equal probability of incorporation and energetic spikes. The energy transfer may cause the collisional cascades and generate point defects, which play determining role in the microstructure and properties of the growing film. The particles with higher kinetic energies cause re-sputtering of deposited coating or implantation effects (Fig. 3b).

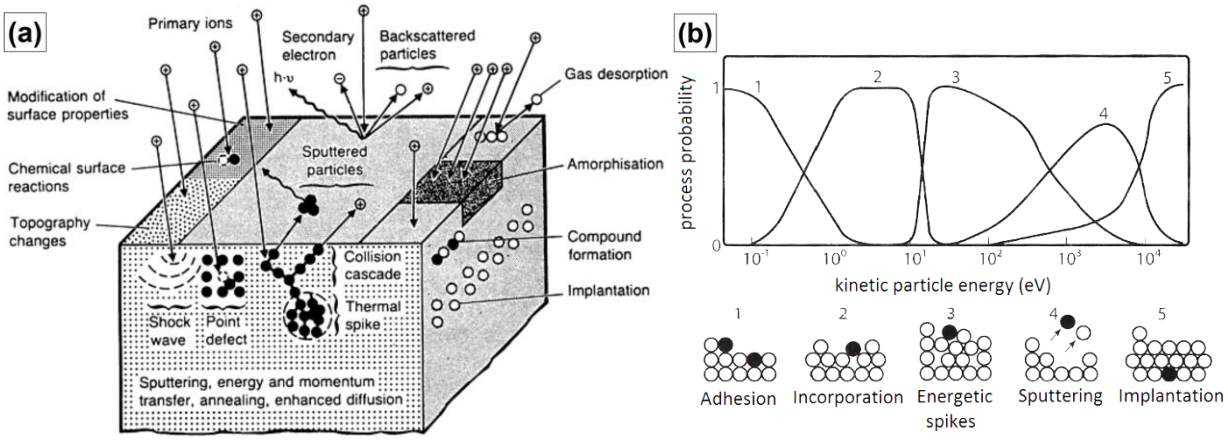

Fig. 3. Interaction events on the target surface during bombardment with highly energetic Ar^+-ions [16] (a) and interaction of the arriving sputtered species with the growing film depending on their kinetic energy [1, 17] (b).

Controlling energy of the arriving species (sputtered particles or biased Ar^+-ions) allow, for instance, tuning the defect density in the growing film, aiming at the defect-free structures (lowering the energy of arriving particles, see 1, adhesion, in Fig. 3b) for e.g. microelectronic and optical properties, or highly defected structures, improving mechanical and thermodynamic characteristics.

1.2. Thin film microstructural growth

The fundamental phenomena occurring during the film growth can be divided into a few main stages (Fig. 4a, stages 1-5) [17-19]. The arriving sputtered particles adsorb of the substrate surface (adatoms), migrate over it until the low-energy lattice site is found, hence, primarily describing the primary *nucleation* process (1). The adatoms migration, accompanying the film growth during the entire deposition process, and primary nucleation occur during the second stage as well, which is, however, mainly characterized by formation of the first *crystals* (2). With further growth, two neighbouring crystals experiencing a collision *coalesce*, driven by the inherent force to minimize the interface and surface energy, and form a new single crystal, i.e., *grain* (*primary coalescence*) (3). The primary coalescence is determinative with respect to the preferential growth orientation. The third stage is furthermore accompanied by the secondary nucleation – nucleation on the surface of the already formed grain, interrupting, hence, its further growth – and bulk diffusion, if allowed by kinetic. The merged crystals may further coalesce (*secondary coalescence*) causing the grain coarsening, or, if crystal disorientation is pronounced, a grain boundary, resulting, hence, in polycrystalline film growth (4). Finally, a continuous structure develops and further *thickness growth* (5) repeats the main growth stages.

The deeper insights into the adatoms mobility offer molecular dynamics simulations, showing, for instance, faster growth of the low-diffusivity (100)-oriented grains competing with the (111) orientation (Fig. 4b), or as it was also successfully shown on example of TiN thin films [20].

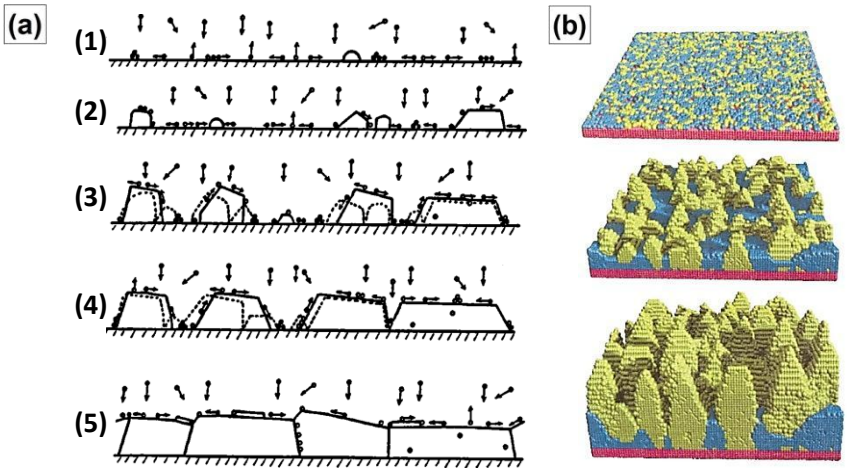

Fig. 4. Illustration of the fundamental processes of the coating's microstructure formation [18, 19] (a) and Monte Carlo simulation of the low-temperature (100) and (111) competitve growth of Al-film [21] (b).

The morphology of the growing film is strongly determined by the surface and bulk diffusion, which in turn closely related to the homologous temperature, T/T_m, where T and T_m are the substrate temperature and melting point of the deposited material, respectively. The

growth morphology can be predicted using the Structure Zone Model (SZM) proposed by Movchan and Demchishin [22], and modified by Thornton [23], who described it not only as a function of the homologous temperature T/T_m, but as that of sputtering gas (argon) pressure as well (Fig.5, the generalized Thornton's SZM suggested by Anders [24]). The low-temperature Zone 1 with T/T_m < 0.3 is characterized by retarded surface diffusion and pronounced shadowing effects, resulted in highly defected structure (e.g. dislocation density > 10^{12} cm^{-2}), rough surface and loose fibrous morphology with open boundaries. Increase of the temperature to 0.3< T/T_m < 0.5 (Zone 2) significantly increases adatoms mobility and enables volume diffusion, resulting in the dense wide columns and surface smoothing. The temperatures above T/T_m > 0.5 (Zone 3) are associated with the recrystallization process with resulted non-columnar, coarse equiaxed grain structure. The transition Zone T (defined by Thornton between the zones one and two [23]) provides the adatoms an increased surface mobility leading to filling of voided boundaries and, hence, to the structure densifications as well as the surface smoothing, which are desirable characteristics in a variety application fields.

The kinetic impact (associated with higher E^*-values in Fig.5) is another important factor in controlling the film microstructure. For instance, the densification of the growing film, i.e., suppression of the Zone 1, may be achieved by applying a negative voltage (bias [25]) to the substrates, bombarding the substrates by attracting the positively charged working gas ions, or lowering the argon pressure used during sputtering deposition, increasing so the mean free path of the sputtered species.

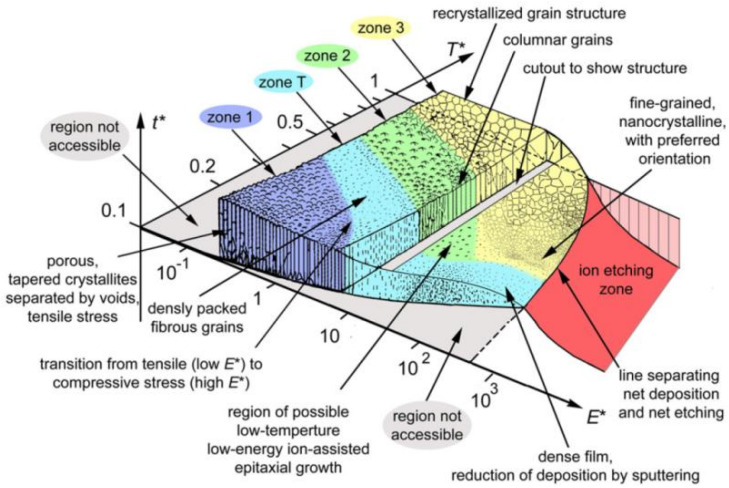

Fig. 5. The generalization of the Thornton's Structural Zone Model for the film growth [23, 24].

Concluding, being in tune with the SZM and fundamental phenomena during thin film growth in general helps significantly in microstructure prediction and resulted macroscopic properties of the coating, e.g., strengthening by mechanism of grain refinement in accordance with the Hall-Petch relationship [26-28] (which is, however, more complex for ceramic-like coatings than for metallic coatings [29]) for different homologous temperatures and working gas pressures. Undoubtedly, the microstructure has a more complex nature and other microstructure-related characteristics, e.g., phase composition, structural defects or impurities play also crucial role in its formation as well.

1.3. Structural defects: impurities and point defects

The PVD techniques with high cooling rates combined with low homologous temperatures (usually 0.2-0.3) result in limited adatoms surface mobility and strongly retarded volume diffusion. Due to this fact, structural defects of the thin films in general and of the reactively sputtered transition metal nitrides (TMNs) in particular are generated in large volume and, hence, their impact on the film microstructure and resulted macroscopic properties cannot be neglected. A variety of material properties – e.g., electrical, magnetic, superconducting [30], mechanical [31, 32] – is vastly influenced by the structural defects. The vacancy-containing structures became the subject of great interest after discovering the high-temperature superconductivity [33].

Depending on the defects spatial dimension, they can be divided as follows: point (zero dimensions, e.g. vacancies, interstitials, impurities, Frenkel and Schottky defects), line defects (one dimension, e.g. dislocations), area defects (two dimensions, e.g. grain and phase boundaries, stacking faults), and volume defects (three dimensions, e.g. cracks, voids, inclusions). Despite the fact that all structural defects significantly contribute to the (strength and hardness are directly related to the dislocation density and their mobility) and even interact closely (being microstructural obstacles, other defects and particularly vacancies inhibit the dislocation motion), we were mainly focused on the investigation of the point defects and, more particularly, vacancy-rich structures.

Small nitrogen atoms, fulfilling the Hägg's rule ($0.41 < r_N/r_{TM} < 0.59$), occupy the octahedral voids at the face-centered cubic TM parent sublattice, forming interstitial solid solution. Ideal stoichiometry in these interstitial TMNs is particularly complex to achieve [34]. Depending on synthesis conditions, formation of quenched-in vacancies [35] (as well as other aforementioned defects) at both, metal and non-metal sublattices is more prevalent. Many TMNs are berthollides, i.e., exhibit a large homogeneity range towards substoichiometric compositions [36, 37], which arise from the vacant sites on the nitrogen sublattice, while overstoichiometric TMNs exhibit a more sophisticated nature. The calculated formation energies of various defected overstoichiometric structures reveal that fcc-$Ti_{0.5}Al_{0.5}N$ prefers metal vacancies [38], while for fcc-CrN vacancies on metal sublattice together with nitrogen on interstitial and anti-sites positions are energetically equal probable [39]. Vacancies have a great impact on the macroscopic mechanical properties. The deficient non-metal sublattice can significantly improve the structural stability [40], lead to hardness deterioration, as e.g. for the group IVA TMNs, as well as to its improvement, as e.g. for the group VA TMNs [31, 41]. Vacancies at the metal sublattice lead, in contrast, mostly to material softening (see **Publication #5**).

An important role in emergence of the nonstoichiometric compound properties is ascribed to the structural ordering. The substoichiometric TMNs with a large vacancy fraction at the non-metal sublattice show a tendency to structural long-range ordering, and, hence, appearance of the ordering phases (superstructures), enriching the phase diagrams [33]. The formation of atomic ordering (associated with lowering of the free energy) occurs when attraction forces

between vacancies and nitrogen are greater than the interaction of the similar lattice constituents (e.g. neighboring nitrogen vacancies were found to repel each other [40]). The ideal superstructures are described with $TM_{2t}N_{2t-1}$ [33] and accompanied by small lattice distortion, lowering the crystal symmetry, e.g., from cubic or hexagonal to orthorhombic and trigonal structures [34, 42].

This knowledge is especially important for the cubic molybdenum nitride known to crystallize with 50% vacancies on the nitrogen sublattice, i.e., 2:1 stoichiometry (see chapter 1.7). Strictly speaking, 50% of vacancies on the nitrogen sublattice represent *structural vacancies*, related directly to the chemical composition of γ-$MoN_{0.5}$. They perform the same functions as the present nitrogen atoms and, hence, the sublattice can be considered as substitutional solid solution of atoms and vacancies [33]. In turn, the alloying-induced population of the structural vacancies is characterized by *constitutional vacancies* [43].

The concentration of impurities, in particular oxygen content, plays a crucial role in film microstructure and properties. Using PVD technique, a high film purity can be reached when depositing in ultra-high vacuum and using a liquid-nitrogen trap [44] (the monolayer formation time can be increased a hundredfold from 0.2 to 20 s, when improving the vacuum from 10^{-3} to 10^{-5} Pa, cf. Fig. 6). The interstitial TMNs are extremely sensitive to the structural impurities (e.g. oxygen). Impurities segregate on the grain surface interrupts its further growth, preventing from coarsening during coalescence. Since the fastest oxygen segregation occurs at (111) surfaces, the film growth is dominated by the competing (100) and (110) oriented grains. The related considerable alteration of the microstructure significantly infuses the macroscopic properties. For instance, within the super-hard nanocomposites nc-TiN/Si_3N_4 at already 2000 ppm, i.e., 0.2 at.%, weaken the SiN_x and dramatically deteriorates the hardness [45], as it also was recently observed for $Ti_{50}Al_{50}N$ at ~1.3 at.% [46].

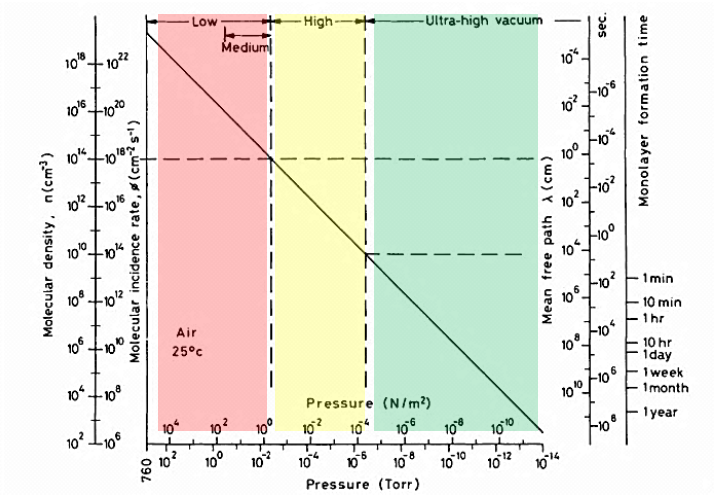

Fig. 6. Formation time of residual gas monolayer on the substrate and target surfaces as a function of the chamber base pressure [47].

Therefore, structural defects are essential in emergence of the material properties, and atomic-scale understanding of their behaviour allows tuning the coating performance.

1.4. Thin film functionality and material selection

The continuously growing demand for the high-functional materials is one of the driving forces in the development of new material systems as well as in the improvement on the already existing ones. The attracted attention to the transition metal nitrides (TMN) is primarily due to their versatile outstanding properties (e.g. high thermal stability, hardness, chemical inertness) resulting from their complex bonding structure, composed of covalent, metallic and, to a lesser extent, ionic bonding types (Fig. 7a). The transition metal nitrides along with other technical ceramics exhibit the lowest wear rate among many other materials, showing at the same time the highest hardness values (cf. Fig. 7b). The wear rate can further be significant reduced by controlling the friction, i.e., tuning the tribological properties.

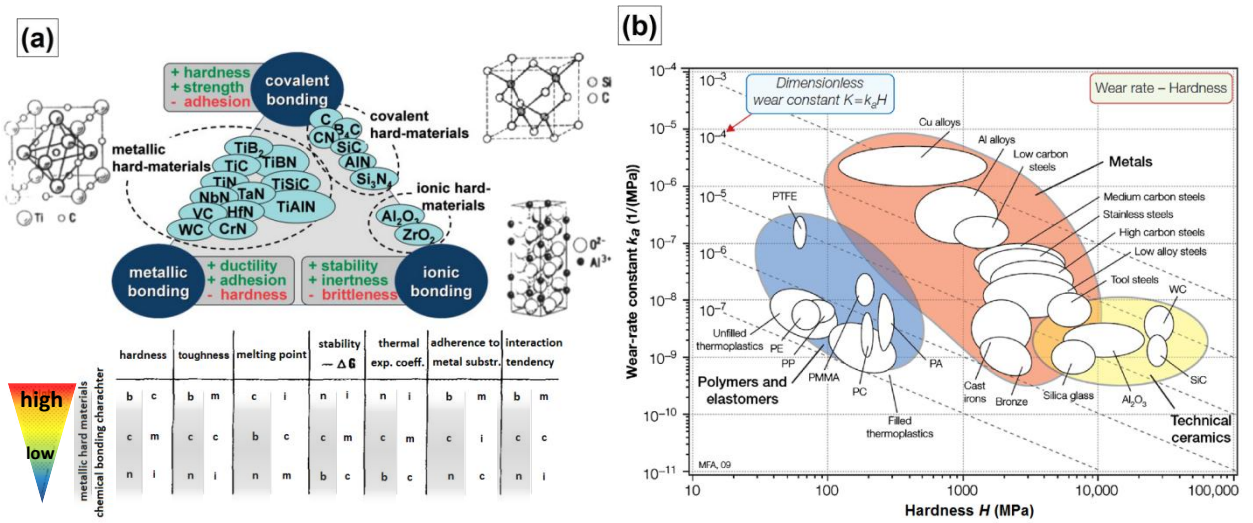

Fig. 7. Classification of hard ceramic materials (n/b/c – nitrides/borides/carbides) depending on chemical bonding character (m/c/i – metallic/covalent/ionic), and their performance, showing the relevance for particular applications [17, 31, 48, 49] (a). A qualitative guidance chart for the interrelation hardness – wear rate [50, 51].

Hardness enhancement promotes though the resistance against abrasion wear, cannot, however, prevent an early failure due to, e.g., cracks or coating delamination, if material is brittle. Hence, synthesis of a hard material with improved toughness – a measure of a threshold energy that can be absorbed without leading to material failure – is still one of the greatest challenges faced by scientists nowadays. Evidently, the key to synthesis of the properties-tuned high-performance materials is the understanding of the mechanical and tribological properties at a fundamental level, using i.a. some established empirical criteria.

One of them, made for carbonitrides [52] – and, as expected and proved later experimentally, suitable for B1-structured TM alloys – is the dependence of the material shear modulus and hardness on the valence-electron concentration (VEC, i.e., the number of electrons in the valence band per unit cell [34, 53]). According to this observation, the highest hardness was found at the nearly the same VEC-value as the calculated maximum of the shear modulus, namely at VEC ≈ 8.4 [31] (fully occupied non-metal–metal while vacant metal-metal

bonding states). Hence, a high hardness of TMN is related to the high shear modulus, resulted in turn from the filling of the shear-resistive bonding states between the non-metal *p* and metal *d* orbitals [32, 52]. Though it was also proven for a specific vacancy concentration resulting in VEC ≈ 8.4, the VEC-theory seems to have a limitation for some strongly substoichiometric compounds with apparently altered electronic structure [52], as referred to [31, 41]. Indeed, for the group IV TMs, TiN_x and ZrN_x, (VEC = 9 for x =1), the vacancy-related decrease of VEC leads to a continuous hardness deterioration [31, 32], while for the group V TMs, NbN_x and TaN_x [31] (VEC = 10 for x =1), the vacancy-related decrease of VEC enhances the hardness when approaching VEC of 8.4. The observed strengthening/softening may be related to the lower/higher degree of population of shear-sensitive metallic d-d states [32].

Another important material feature – toughness – is often characterized in terms of elastic constants G/B-ratio (Pugh, 1954 [54]) and Cauchy pressure C_{12}-C_{44} (Pettifor, 1992 [55]), suggesting that a ductile material exhibit the values $G/B < 0.5$ and C_{12}-$C_{44} > 0$ [56, 57] (Fig. 8a). Interestingly, the both toughness-related criteria, similar to shear moduli and hardness, were observed to depend on VEC as well, increasing, however, continuously (and nearly linearly) with rising VEC without showing their maxima at a certain value [56, 57]. The shift of the Cauchy pressure from the negative to positive values alters the bonding type from the directional covalent towards metallic, the toughness enhancement can be referred to the population of the shear-sensitive metallic d-d states [56]. Upon shearing, causing the bending of the shear-resistive non-metal-metal bonding states, the overlapping shear-sensitive metal-metal orbitals become increased causing the formation of a layered electronic structure with a pronounced difference in the bonding strength, i.e., strong/weak/strong, as, for instance, Mo–Mo/Mo–N/V–N in Fig. 8b [56]. Such layered electronic structure activates the slip system, promoting the dislocations glide and, hence, the plastic deformation. The plastic flow contributes, finally, to relaxation of intrinsic stresses, as also proved experimentally [58].

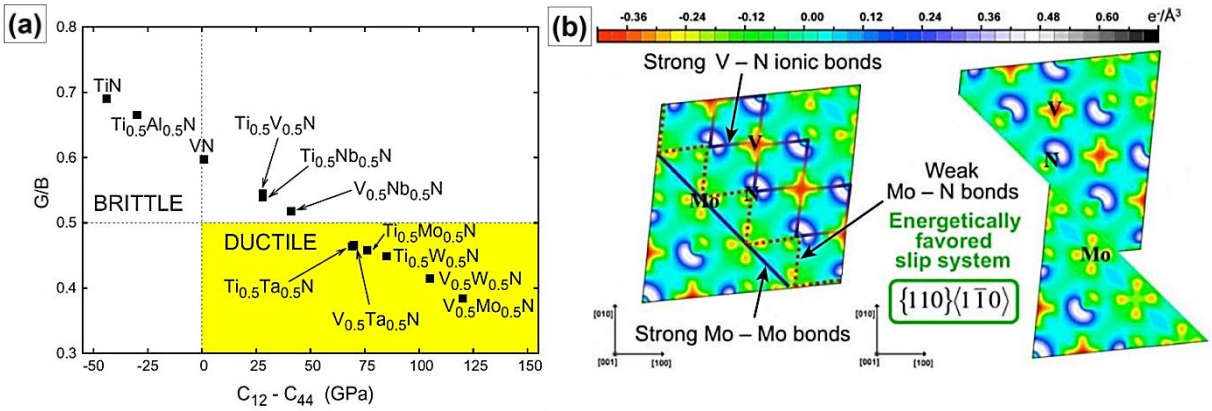

Fig. 8. The Pettifor and Pugh criteria [56] (a) for different Ti- and V-based TMNs and the slip system upon shearing in the high-VEC ordered $V_{0.5}Mo_{0.5}N$ [59].

The tribological behaviour of the oxide-forming materials can be described in terms of crystal chemistry using ionic potential, φ, [60, 61]:

$$\varphi = Z/r \quad (1)$$

Here, Z is the formal cationic charge and r is the cation radius. Generally, the higher is the ionic potential of the forming oxides, the lower is their friction coefficient [61]. The extent to which a cation is surrounded by anions (screening effect) determines the bonding strength with the neighbouring cation. For a low ionic potential (large, weakly charged cations), the screening effect of the anions is insignificant allowing the neighbouring cations, thus, to interact form strong covalent and ionic bonds. Such oxides (e.g. Al_2O_3) are usually shear-resistive (even at high temperatures). Rise of the ionic potential (small, strongly charged cations) results, in contrast, in improved screening effect, preventing the interaction of the neighbouring cations and forming shear-sensitive, lubricious oxides with low melting point (e.g. MoO_3, CrO_2 [62]). Consequently, chemical elements with a high ionic potential (e.g. Re, W, Mo) due to formation of lubricious oxides on the coating surface at elevated temperatures. For a multicomponent system, combination of the element forming oxides with considerably different ionic potentials was observed to improve the tribological behaviour [61].

Based on the aforementioned empirical criteria, the molybdenum-based nitrides appear to be multifunctional materials suitable for high-demanding applications. Specifically, the comprehensive theoretical studies reveal the supertoughening effect of molybdenum-containing nitride materials [56, 63]. Secondly, The simple calculation of VEC for the cubic-structured molybdenum nitride with the half-occupied N-sublattice yields the value of 8.5, suggesting, therefore, the close-to-maximum hardness value within the Mo–N system. Finally, due to small ionic radius, high oxidation state and resulted high ionic potential, φ, Mo-based compounds should form lubricious oxides (besides the lubricious Magnéli phases [64, 65]) on the coating surface at elevated temperatures (for instance, during dry machining process).

There are certainly a plenty of other approaches in material selection and functionality improvement. For instance, a structural way in designing material properties, by applying the mechanisms of strengthening (grain refinement as well as solid solution, precipitation and strain hardening), toughening (dissipation of accumulated energy, e.g., through grain refinement, stress concentration scattering, alternation of strain and stress fields) or, as shown in chapter 1.5., altering the material architecture and manipulating microstructure evolution (e.g. grain refinement, texturing, column growth prevention) [48, 66]. Another one is functional, implying combination of materials showing different properties [48].

1.5. Advanced thin film concepts

One of the approaches in synthesis of sought-after multifunctional coatings is based on the coating architecture, designing which one can combine the advantages and overcome the drawbacks of the single monolithic coatings. Certainly, such artificial structures can only be obtained when limiting the growth kinetic, e.g. by rapid cooling (typical for non-equilibrium PVD techniques) and lowering the homologous temperatures.

Conjunction of hard and soft materials results in "load-adaptive coatings" with improved tribological properties and extended lifetime (Fig. 9a) [6, 67, 68]. The concept of nanocomposites contributes to the mechanical and tribological properties enhancement and is often used to synthesise the ultra-hard coatings with the hardness over 70 GPa (Fig. 9b) [6, 45, 67, 68]. Formation of additional interface volume, designing, e.g., multilayered structures, is ideal tool against crack propagation (e.g. by its deflection or energy dissipation and resulted internal stress relaxation) and improved hardness and toughness (Fig. 9c) [6, 48]. A particular case of the multilayer coatings are superlattices, i.e., combination of the isostructural materials with similar lattice constants and a single layer thickness of a few nanometers, which are endowed with unique properties (Fig. 9d) [6, 48, 69]. The concept of gradual transition from metallic adhesion layer into a functional outer compound is used in the gradient layers (Fig. 9e) [14].

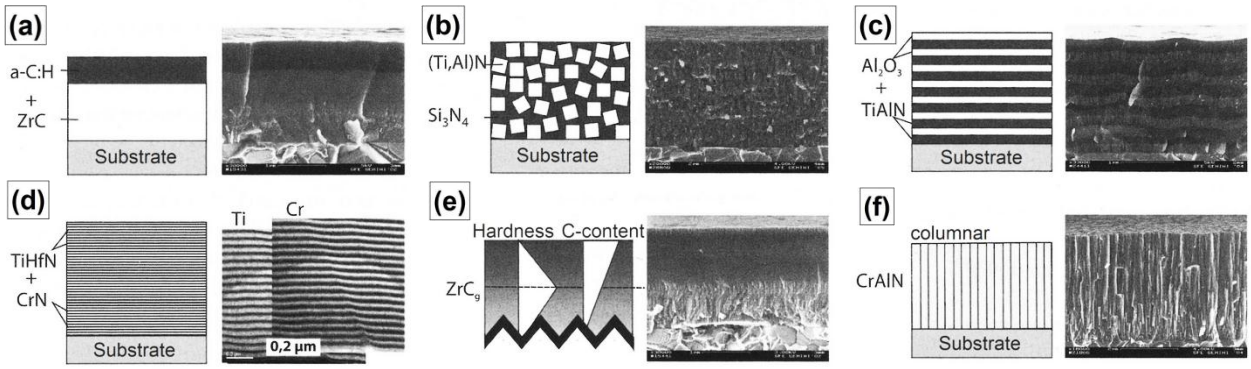

Fig. 9. Various coating architectures: hard/soft combination (a), nanocomposite (b), multilayer (c), superlattice (d), gradient (e), and metastable (f) [1, 70].

One of the most important groups aiming at improving coating performance is formed by metastable solid solutions (Fig. 9f) from materials, which differ significantly in bonding character (and other properties) and, hence, cannot be synthesised in the thermodynamic equilibrium [6]. An excellent example are the Al-containing cubic transition metal nitrides [71] and particularly cubic-structured $Ti_{1-x}Al_xN$ [72-77]. The inherent high mixing enthalpy of such supersaturated metastable materials implies high driving force to decomposition into thermodynamically stable constitutes. The material selection is often directed towards the constitutes, tending to the isostructural (spinodal) decomposition at elevated temperatures, which further improves the properties by formation of the coherently strained domains [6].

1.6. Quantum-mechanical materials science

This thesis represents the *ab initio*-guided and -supported experimental investigations. Computational materials science, and particularly density functional theory (DFT) [78], is essential in prediction as well as providing thorough insights into the origin of the experimental phenomena by using a quantum-mechanical approach, i.e., solving the Schrödinger equation using different approximations [79]. The PVD deposited thin films are known to crystallize in supersaturated solid solutions and, hence, in a region of the phase diagram, where for bulk material in equilibrium phase segregation would take place. However, due to kinetic limitations resulted from the high cooling rates during PVD and homologous temperatures in the range 0.2-0.3 allow for the formation of metastable phases far from the thermodynamic equilibrium. Since an *ab initio* treatment of a representative thermodynamic ensemble is not feasible even nowadays, we used the SQS approach („Special Quasi-random Structures“) for calculation of random alloys – a well-suited method when treating random alloys and vacancy/defect-containing structures (including covalent interactions) due to its local character (e.g. relaxation of the structure). Previous investigations on many nitride-based systems yielded an excellent agreement with experiments showing its suitability for the study of formation energies and lattice parameter [58, 80-85]. In all these studies, DFT simulations, using the SQS approach, have significantly contributed to the understanding of experimental results.

1.7. Material Systems – State of the art

Technological progress is closely related to development of new high-performance materials. In the framework of this thesis, a comprehensive investigation of the Mo-based material system Mo–Al–Cr–N, supported by *ab initio* calculations, was carried out. The emphasis was placed on Mo-based compounds mainly due to several empirical criteria, e.g., G/B and C_{12}-C_{44}, VEC, and φ, suggesting supertoughening effect, enhanced hardness and tribological properties, respectively, of Mo-containing TMNs [56, 63-65].

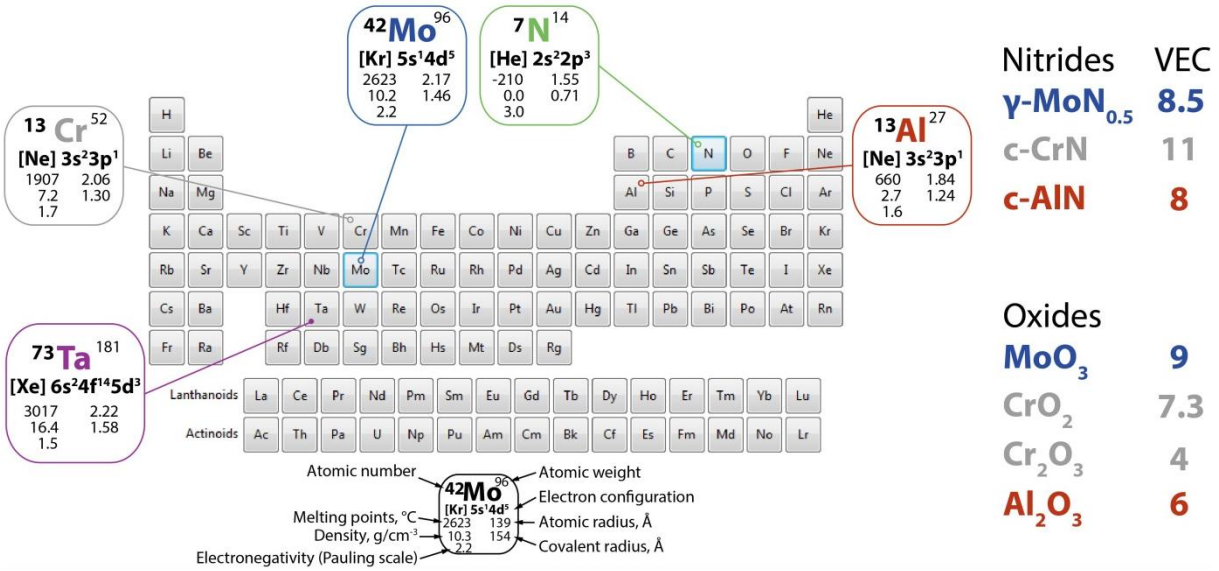

Fig. 10. An extended and Mendeleev's periodic table modified after [86], including some important characteristics for the project-related chemical elements [87].

The exceptional properties of TMNs and particularly molybdenum-based nitrides (e.g. high hardness, chemical inertness) arise from their complex bonding structure (Fig. 7a) [88]. The nitrides (and particularly investigated in the framework of the thesis Mo, Cr, Ta, cf. Fig. 10) become, however, less stable from group IV to VI TMNs. Occupation of the nonbonding states results in stretching of the initially strong metal–metal bonds, hence, weakening them. Moreover, the electrostatic interactions between TM- and N-ions (electronegativity difference) are weakening from group IV to VI TMNs. Due to the weak TM–N bonds, the group VI TMNs tend to decompose releasing the nitrogen at temperatures lower 1000 °C and, hence, are not treated as refractory materials [30].

Addition of Al is of the highest industrial interest due to enhancement of mechanical properties (lowering of VEC of the stoichiometric TMNs towards 8.4 [31]) as well as oxidation and wear resistance [89]. The bonding structure of TMNs and AlN is vastly different, composing of covalent, metallic and (to a lesser extent) ionic bonding types for TMNs and mainly covalent for AlN.

An increased thermal stability as well as improved macroscopic mechanical properties may also be achieved for the vacancy-rich structures (the interstitial TMNs are primarily nonstoichiometric), associated with a great activation energy needed to activate the vacancy migration [40].

1.7.1. Binary (Mo–N, Cr–N, Al–N)

Molybdenum nitride (Mo–N)

Molybdenum nitrides are fascinating materials and depending on their phase composition can be designed for a variety of applications requesting for tailor-made properties. For instance, due to excellent tribological performance Mo–N coatings were found to be a very promising candidate as protective coating against the rapid tool wear for pistons in a diesel engine [90] or against contamination for micro-injection mold inserts [91].

All crystallographic phases (Fig. 11) within the Mo–N material system are not only superconductive materials, but also exhibit other excellent properties. For example, hexagonal δ-MoN [92-94] is the hardest superconducting metal nitride [95] (>50 GPa when deposited via PVD [96]) with the second highest superconducting transition temperature, T_c, of 13.8 K among all metal nitrides [95, 97]. Another excellent example is Mo_2N (T_c = 5-7 K) [95, 97-99] since its high-temperature allotropy, cubic-structured γ-Mo_2N, exhibits excellent mechanical and tribological properties (due to the forming Magnéli oxide phases, Mo_nO_{3n-1}) [64, 100, 101] and, hence, a very promising candidate for wear-resistant coatings. Moreover, the empirical VEC criterion of 8.5 suggests virtually the highest hardness (which is often observed for VEC = 8.4, implying, hence, γ-$MoN_{0.48}$) within the single phase region, for different content of N-vacancies (unless the electronic structure is significantly altered due to the great vacancy density [52]). Here we used γ-$MoN_{0.48}$, since unlike the most cubic-structured TMNs, γ-Mo_2N crystalizes with 50% vacancies at the nitrogen sublattice, which are furthermore randomly distributed [102]. The major drawback, however, is that γ-Mo_2N is very sensitive to the nitrogen content and, thus, strongly governed by the nitrogen partial pressure used during deposition.

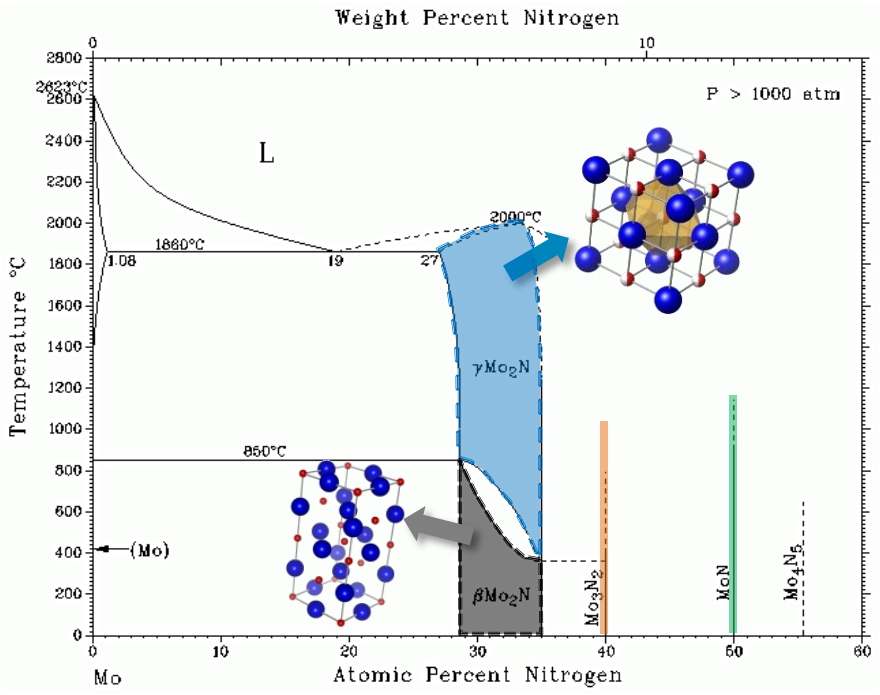

Fig. 11. The equilibrium phase diagram of Mo–N system with isobars [103] and unit cells [86].

The other phases are either poorly studied or reported to be unstable. The ordering phase Mo_3N_2 enriched the phase diagram plotted by Jehn [103] (as many other ordering phases of nonstoichiometric TM nitrides and carbons [33]). The 3:2 stoichiometric Mo_3N_2 first reported by Troitskaya *et al.* [104] and classified as B1-type structure with partial occupation of both sublattices. The hypothetical 1:1 stoichiometric cubic-structured ξ-MoN was proposed (but kept for improbable) first by Linker *et al.* in 1986 [105] to crystallize with the NbO-type structure (which can be thought of as the B1-type structure with 25% vacancies at each sublattice), but predicted only recently, in 2014, by Liu *et al.* [106] (based on findings of Wang *et al.* [107]) to exhibit the lowest energy of formation among many other competing structures. Cubic ξ-MoN is predicted to have the highest superconductive temperature among all refractory carbides and nitrides with T_c = 29.4 K [108] and, though it was found to be thermodynamically unstable [109, 110], some studies report on its synthesis [111, 112].

Summarising, increasing nitrogen content or rising nitrogen (partial) pressure, the PVD Mo–N coatings undergo the following phase transformation:

$$\gamma\text{-}MoN_{0.5} \rightarrow \gamma\text{-}MoN_{0.5} \text{ and/or } \xi\text{-}MoN + \delta\text{-}MoN \rightarrow \delta\text{-}MoN$$

Controlling other deposition parameters, formation of a certain phase can be favoured or supressed. For instance, the hexagonal δ-MoN is favoured by the low kinetic impact, i.e., low substrate temperature and bias voltage, and vice versa, γ-$MoN_{0.5}$ forms predominantly at high substrate temperatures and bias voltage (as found for cathodic arc evaporation) [96].

The main limitation of the Mo–N coatings is due to the volatile oxide MoO_3 forming at elevated temperatures in the oxygen-containing atmosphere [64, 113], restricting the temperature range of application to 300-500 °C [64, 101]. One of the ways to extend the application field to higher temperatures is addition of elements forming protective, dense oxide scales, preventing further oxygen inward and molybdenum outward diffusion. Moreover, Al_2O_3 with its highly ionic chemical bonding character and resulted high stability and chemical inertness is suitable for surface applications.

The Cr–N material system exhibits two intermediate phases in the thermodynamic equilibrium, h-Cr_2N (with the single phase range CrN_x with x = 0.38-0.5 [34]) and B1-structured fcc-CrN (CrN_x with x = 0.82-1.14 [114]), see Fig.12a, which structure and thermodynamics were comprehensively investigated via first principle calculations not long ago [115].

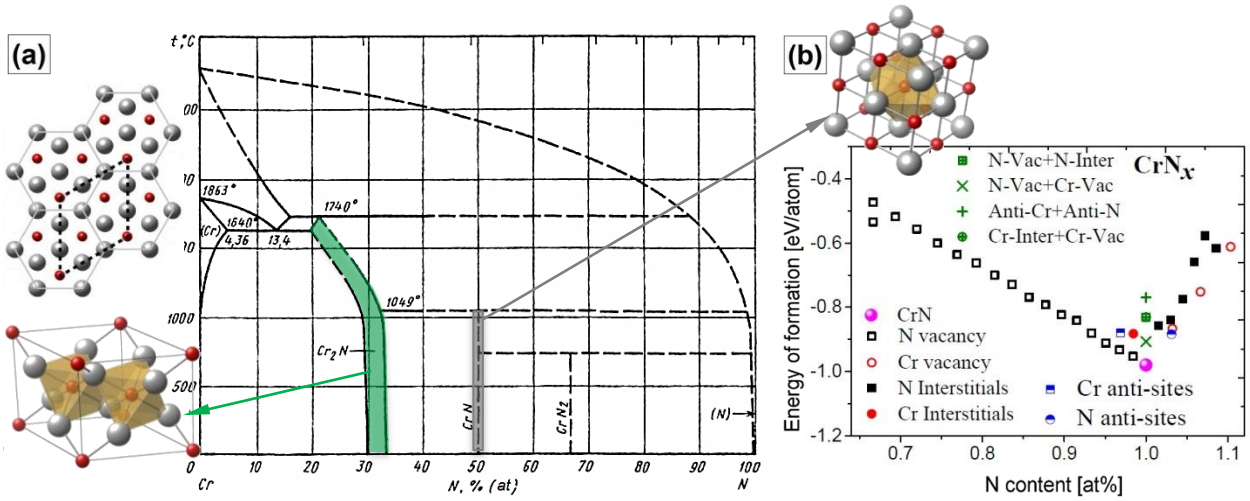

Fig. 12. Equilibrium phase diagram within the Cr–N material system [116] with the unit cells of h-Cr_2N and fcc-CrN [86] (a) and energy of formation of sub- and overstoichiometric fcc-CrN_x [39].

The microstructure, related mechanical properties, thermal stability as well as oxidation kinetic of the reactively sputtered are in detailed investigated by Mayrhofer *et al.* [117-120]. Exposure to elevated temperatures (in the inert atmosphere) reveals the onset temperature for decomposition into Cr_2N and (g)N_2 at ~1000 °C [118]. As a non-refractory group VI TMN, B1-CrN has a low thermal stability due to the weak Cr–N bonds breaking at ~1000 °C, resulting, hence, in release of N_2 [30]. The hexagonal-structured C_2N shows a higher thermal stability, dissociating into Cr an N_2 above 1200 °C [118].

The mechanical properties, and in particular hardness, were found to be strongly related to the microstructural characteristics, e.g. grain size, and residual stress [117]. The highest hardness was observed for stoichiometric CrN, which, however, is very sensitive to the nitrogen partial pressure and ion energy, hence, crystallizing preferred as many other TMNs with partially vacant lattice sites [36]. Formation of the substoichiometric CrN_x compositions (Cr/N < 1) is caused by generation of vacancies on the nitrogen sublattice (Fig. 12b). Interestingly, the comprehensive investigations of the atomic and electronic structure (computational and experimental) of substoichiometric CrN_x reveals the ordering of the vacancies within the (111) planes [42] and vacancy-relted alteration of the bonding structure, resulted in weakening of the ionic and strenghethening of the covalent bonds with increasing vacancy concentration in CrN_x from 1 to 0.5 (CrN → Cr_2N), and increase of metallic character with further increase of vacancy concentration (Cr_2N → Cr). The overstoichiometric compositions (Cr/N > 1) arise with nearly equal probability from vacancies at the Cr-sublattice, nitrogen at the interstitial and anti-site (substitution of Cr on metal sublattice) positions (Fig. 12b) [39].

Aluminium nitride is known to crystallize with the wurtzite-type structure, w-AlN, exhibits, however, also a metastable high-pressure (allotropic modification – cubic-structured fcc-AlN [121-124]. Treating as a bulk material, the cubc allotropy requires extremely high compressive stress of 23 GPa [125] to be stabilized. Still, there are some ways to synthesise fcc-AlN using non-equlibrium PVD techiques, which due to high cooling rates and low homologous temperatures (usually 0.2-0.3) results in kinetic limitations. Two concepts are most common nowadays: designing metastable multlilayer structures or solid solutions.

Formation of metastable multilayer structures is based on the principle of minimum total energy, expressing the interplay between interfacial and volume energies (cf. Fig.13a) [123, 126]. An isostructural material with similar lattice space, e.g. fcc-TiN in combination with low layer thickness of fcc-AlN (t_0 of ~1.5-3 nm [124, 127-129]) is required. The former is essential to achieve the "template" effect, i.e., coherent growth with fcc-AlN, lowering its interfacial energy, which is dominating during the initial growth. For instance, while this concept is successfully applicable for TiN/AlN (lattice mismatch of ~4,9%, assuming <100> growth direction perpendicular to the sample surface [130, 131]), fcc-AlN cannot be stabilized within ZrN/AlN due to the lattice misfit of ~12% [127, 130]. The latter, i.e. critical layer thickness t_0, is to prevent the volume energy (which is considerably larger for fcc-AlN) to become dominative constitute of the total energy.

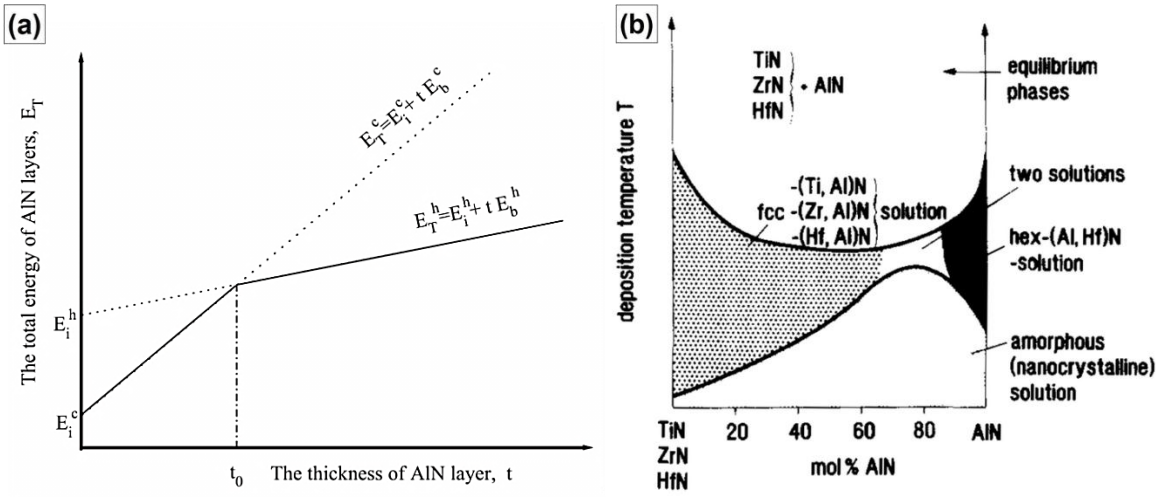

Fig. 13. The total energy of fcc-AlN and w-AlN depending on their layer thickness, with the solid line indicating the low-energy path of the phase development [129] and PVD phase diagram for the fcc-AlN-containing metastable solid solutions [14].

Synthesis of metastable solid solutions using far from thermodynamic equilibrium prevents the instantaneous decomposition into the stable constitutes (Fig. 13b). Here, the threshold solubility concentration of fcc-AlN plays a crucial role, overcoming which formation of w-AlN becomes favoured. Although the driving force for the phase transformation into w-AlN is large, due to the high internal stresses, a great activation energy is required, in order to overcome the energy barrier for the phase transformation into w-AlN (accompanied with 22% volume gain) [125, 132-134].

1.7.2. Ternary (Cr–Al–N, Mo–Cr–N, Mo–Al–N)

Chromium aluminium nitride (Cr–Al–N)

Cubic CrN exhibits higher corrosion and wear resistance and toughness as compared to, e.g., TiN coatings [135], which furthermore can be significantly improved in solid solution fcc-$Cr_{1-x}Al_xN$, showing best performance for the highest Al-contents [89, 135, 136]. Within fcc-$Cr_{1-x}Al_xN$, fcc-AlN has the highest solubility limit (~0.7) among all B1-structured TMNs [135], which strongly depends on the deposition parameters [137] and can be shifted to significantly higher values, when tuning the compressive stresses of the coating [76]. Higher Al-contents, overcoming the threshold Al-concentration, trigger the formation of the hexagonal structure.

The CrN coatings are however thermodynamically less stable due to the weak Cr–N bonds (typically for the group VI TMNs), which during annealing in the inert atmosphere start breaking at 1000 °C and decompose completely at 1400 °C [118, 138]. Alloying with Al improves thermal stability, shifting the onset of decomposition to higher temperatures. The exposure to the elevated temperatures initiate decomposition process, starting with precipitation of h-AlN and, hence, formation of the Cr-rich cubic matrix and consequently of the Cr–N bonds, according to:

$$\text{fcc-}Cr_{1-x}Al_xN \rightarrow \text{fcc-}Cr_{1-x}Al_xN\text{ (Cr-rich)} + \text{h-AlN} \rightarrow \text{h-}Cr_2N + \text{w-AlN} + (g)N_2 \rightarrow \text{c-Cr} + \text{h-AlN} + (g)N_2$$

Molybdenum chromium nitride (Mo–Cr–N)

There is only a limited number of studies on Mo–Cr–N coatings, concentrated mainly on the Cr-rich compositions [139-148], which when using the non-equilibrium PVD technique, e.g., magnetron sputtering, crystallise with the B1 cubic structure with a nearly linear change of the stress-free lattice parameter, resembling the Vegard's observation for the ideal ionic crystals [149]. Addition of Mo results in improved ductility due to increased metallic bonding character of single-phase cubic Mo–Cr–N as suggested by the computational study [57] and – according to the contradictory experimental results – deteriorates [146, 148] or enhances [142, 144] the mechanical properties of Cr–N. The evaluated indentation hardness (14-17 GPa) and modulus (200-250 GPa) of the ternary $Mo_{1-x}Cr_xN$ [146] are even below that of many binary nitrides.

Molybdenum aluminium nitride (Mo–Al–N)

Only little is known about the Mo–Al–N material system [150-152], with the highest reported Al-content within fcc-$Mo_{1-x}Al_xN$ of x = 0.33 [150], while for x = 0.7 (target composition) hexagonal phase was observed [152]. Hence, similar to Al-containing cubic solutions, a threshold concentration is available. Higher Al-contents improve the oxidation resistance (from 500 to 700 °C as compared to γ-$MoN_{0.5}$ [64, 150]) as well as hardness, however only for minor Al-concentrations, x = 0.06, [150].

Additionally, the main conclusion drawn within the poorly investigated quaternary system, Mo–Al–Cr–N, minor Mo-additions to the Al-rich cubic-structured coatings result in best coating performance (with respect to oxidation resistance, hardness and drilling performance) as compared to additions of other TMs is publications [152-154].

2. Experiments description

2.1. Synthesis

A modified Leybold Heraeus Z400 magnetron sputtering system (Fig. 14a) was used to synthesise the coatings in DC glow discharge, established in a gaseous mixture of Ar and N_2 (both gases with purity above 99.999%). Prior to the deposition process, the chamber was evacuated to a high vacuum of $p_{base} \leq 5 \cdot 10^{-4}$ Pa. A constant total pressure, p_T, of 0.35 Pa was kept for all sputtering processes during deposition. The N_2-to-total pressure ratio, p_{N2}/p_T, was varied between 0.13 and 1. All coatings were deposited at 0.4 A DC on the targets (Ø75mm), covered uniformly with alloying elements (Fig. 14b, c), and substrate floating potential of ~ -15 V. The constant substrate temperature of 450 ± 20 °C provides increased ad-atom mobility, preventing the appearance of voided columnar boundaries. After each deposition processes, the substrates were cooled down below 100 °C before ventilating the deposition chamber, in order to minimize the surface chemistry alterations [155].

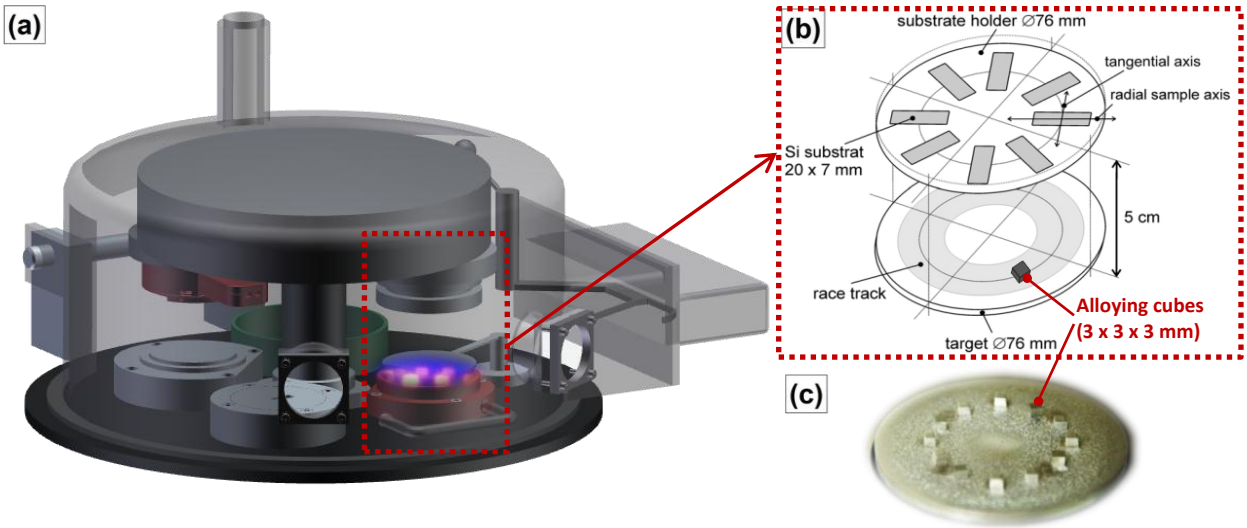

Fig. 14. A view inside the deposition chamber during sputtering (a), target–substrate holder arrangement (b), and photo of Mo-target with uniform distributed Cr-cubes on its race track (c).

2.2. Characterization

X-ray Diffraction

Crystallographic structure was reviled by means of X-ray diffraction (XRD [156, 157], Philips X'Pert) in the symmetric Bragg-Brentano geometry, using monochromatic CuK_α radiation (λ = 1.5418 Å). Evaluation of the stress-free lattice parameter was performed after glancing angle XRD measurements with an angle of incidence γ = 2° (PANalytical Empyrion) and subsequent application of the $sin^2\psi$ method [158].

Electron microscopy

The film growth morphology and rate were investigated from fracture cross-sections of coated Si-substrates using scanning electron microscope (SEM, FEI Quanta 200 FEGSEM with a spatial resolution of ~2 nm). An integrated EDAX Genesis system allows analysing the elemental composition by means of energy dispersive X-ray spectroscopy (EDS)[1]. Further investigations of the growth morphology and structure were conducted by means of transmission electron microscopy (TEM, FEI TECNAI F20 operated at 200 kV, with lattice resolution of ~0.14 nm) and selected area electron diffraction (SAED).

Nanoindentation

Besides the conventional empirical methods of the hardness determination (scratching and indentation), there are also some computational approaches allowing to predict but also support , e.g. the recently suggested approach based on the material electronegativity [159]. The application of the conventional hardness measurements with a few micrometres penetration depth is limited to the thin films, having usually the thickness of the same magnitude. In order to obtain the film-only indentation hardness, *H*, and modulus, *E*, excluding the surface roughness and substrate influences, the penetration depth of the indenter tip (see Fig.15) should not overcome the range ~5-10% of the film thickness. The upper limit is often referred to the Bückle's observation, summarizing empirical findings of the earlier researchers [160]. The possible significant deviations, especially when treating super- (> 40 GPa) and ultra-hard (> 60 GPa) coatings on steel substrates, which starts deforming at penetrations depth less than even 3% of the film thickness, were recently shown using non-linear finite element modeling [161].

Nanoindentation tests were performed within the load range of 3 to 45 mN (30 indents pro sample) using an ultra-micro indentation system (UMIS) equipped with a Berkovich diamond indenter tip. The evaluation of the film-only *H*- and *E*-values from the load-displacement curves (Fig. 15c) was carried out after Oliver and Pharr [162].

[1] Several samples were investigated by Time-of-flight Elastic Recoil Detection (TOF-ERDA) to calibrate the EDS using 36 MeV ^{127}I primary ions and the recoil detection angle of 45° at a tandem accelerator (Uppsala University, Sweden) and used subsequently used as calibration standards for the EDS analyses, especially with regard to the light elements

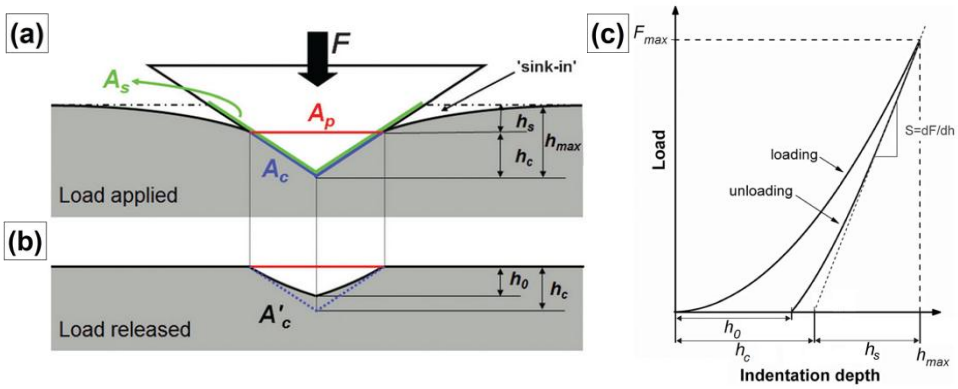

Fig. 15. The simplified illustration of a nanoindentation measurement at the maximum load, F_{max}, (a), after releasing (b), and a recorded load-displacement curve (c) [163]. The projected area, A_p, used for evaluation of the indentation hardness, is associated with the true contact area A_c and the contact depth, h_c. The ideal contact area, A_s, and related maximum penetration depth, h_{max}, would correlate with A_p (h_c) without elastic flexure (and related "sink-in" depth, h_s). The apparent contact area A_c' with related residual depth, h_0, arises after releasing the load and is commonly directly measured using an optical method. The contact stiffness $S = dF/dh$ (at $h = h_{max}$) from the unloading part of the curve (c) is used for evaluation of the indentation modulus.

$$H = F_{max}/A_p \tag{1}$$

$$E \sim S/\sqrt{A_p} \tag{2}$$

The Poisson's ratio, ν, was taken as 0.25. Due to the partial development of the plastic zone within the thin films, the evaluation of the indentation hardness for the film thicknesses below 1 µm is based on the "plateau" approach, i.e., region of the constant H-values on the hardness/penetration depth diagram (Fig.16a) [164]. The film-only indentation modulus, E, is obtained at zero penetration depth after extrapolation of the measurement data (Fig.16b).

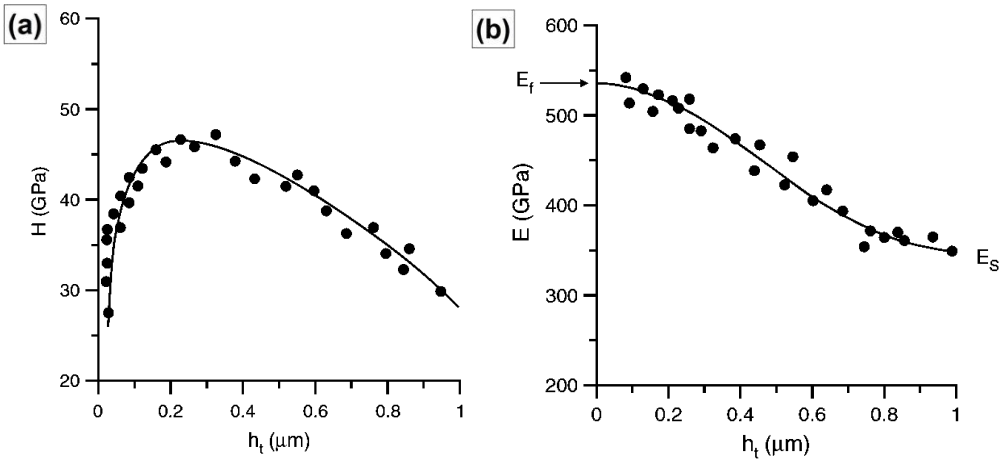

Fig. 16. Evaluation of the film-only indentation hardness and modulus [164].

Nanoindentation with the penetration depths on the nanometer scale is a very sensitive technique and even very little changes of force and displacement readings lead to significant errors in the experimental results. Hence, elimination of the thermal drift, mechanical vibrations, as well as surface roughness (e.g. by using the polished substrates, since the substrate roughness is reproduced on the coating surface) is essential and necessary

prerequisite for an precise nanoindentation measurement. Such changes are, however, often caused by the improperly calibrated tip shape and, hence, the resulted projected area, A_p. The Berkovich tip was calibrated using fused silica as the reference sample with a known value of the Young's modulus of 72.5 GPa. In order to verify the correctness of not only Young's modulus but also the hardness determination, a few reference samples were tested first. The obtained results are shown in the table 1.

Table 1.
Comparison of the measured hardness and Young's modulus (Exp.) with the references (Ref.).

	Sapphire			Si-wafer		MgO		Fused Silica	
	Exp. (11-20)	Exp. (1-102)	Ref. [165]	Exp.	Ref. [166]	Exp.	Refs. [167, 168]	Exp.	Refs. [165, 166]
H, GPa	30.7±0.4	30.6±0.6	~30*	13.2±0.1	10–12	11.0±0.2	~4–10	10.5±0.1	8–10
E, GPa	483±6	458±5	404–499	185±2	172	332±14	248–349	72.5±1.0	72.5

Hence, calibrating using the known Young's modulus, we obtained the indentation hardness of 10.5 GPa which is in excellent agreement with that using, e.g. by S. Vepřek [45], which is much lower than 12.6 GPa, obtained in many other studies. Nevertheless, S. Vepřek points out that the hardness estimation on the instrument, calibrated by known Young's modulus, is incorrect and leads, for instance, to a wrong hardness value for sapphire of 30 GPa (as obtained in our work as well) instead of the correct value of 21 GPa [45]. Therefore, in order to estimate the most important indentation parameters, *H* and *E*, correctly, the two-step calibration, using both constant hardness and constant modulus, respectively, was suggested.

3. Contribution to the field

The main results, obtained in the framework of the current research project and highlighting our contribution to the *surface engineering* scientific field, are divided into the following chapters, 3.1-3.5, according to how they have been/will be presented to the scientific community. Starting investigating the binary Mo–N (Chapter 3.1), we continued with ternaries by alloying first with chromium, Mo–Cr–N (Chapter 3.2) and then with aluminium, Mo–Al–N (Chapter 3.3) and subsequently combined the gained knowledge investigating the quaternary Mo–Al–Cr–N (Chapter 3.4). Finally, focusing in a higher extent on the impact of the vacancies, we investigated Mo–Ta–N material system (Chapter 3.5). For the detailed information, we refer to the journals that the manuscripts have been published in as well as to the appendix at the end of the thesis, containing the full-text manuscripts.

3.1. Computational and experimental studies on Mo–N hard coatings

(See **Publication #1** for details [169])

The current study is dedicated to research into vacancy-driven phase evolution as well as alteration of the mechanical properties within the binary Mo–N. For this purpose, MoN_x coatings were reactively sputtered at varying nitrogen partial and subsequently subjected to compositional, microstructural and micromechanical investigations. The first principles calculations on the phase formation energy as a function of nitrogen vacancy concentration, *x*, performed by *Nikola Koutná*, *David Holec*, and *Holger Euchner*, were carried out for tetragonal β-MoN_x, cubic γ-MoN_x, pseudo-cubic γ'-MoN_x (*with partially ordered N-vacancy-rich NaCl-type*) and γ''-MoN_x (*with partially ordered N-vacancy-rich NbO-type*), and hexagonal δ_1-MoN_x (WC-type) and δ_2-MoN_x (NiAs-type). The energetically inferior δ_1-MoN_x is not treated hereafter.

The metastable cubic γ-MoN_x with the single-phase field extended towards higher nitrogen vacancy concentrations, *x* = 0.33 – 0.53, exhibits the highest hardness of ~33 GPa for γ-$MoN_{0.53}$. The occupation of the initially randomly distributed vacancies on the nitrogen sublattice of γ-MoN_x results in their partial ordering, i.e., formation of the coherent domains of the partially ordered pseudo-cubic γ'-$MoN_{0.67}$ – are the highlights of the current study, described in more details below.

The *ab initio*-obtained formation energies, representing the thermodynamically equilibrium state, indicate two global energy minima at *x* = 0.47 and 1, related to β-$MoN_{0.47}$ and δ_2-MoN, respectively, in agreement with the Mo–N phase diagram. Other compositions, *x*, revealing "only" local minima, are metastable and in thermodynamic equilibrium decompose into stable constitutes pursuant to the lever rule. Due to dramatic cooling rates (10^{13} $K \cdot s^{-1}$), however, PVD coatings crystalize far from thermodynamic equilibrium, allowing the metastable phases to form. Hence, the local energy minima become relevant and have to be considered as well. Subsequently, for x < 0.6, dominates β-MoN_x (without considering metallic molybdenum), while for x > 0.75 – substoichiometric δ_2-MoN_x (rough *x*-estimation, without considering the regions of similar formation energies, suggesting the possible phase coexistence). The N-vacancy concentration region in between, 0.6 < *x* < 0.75, favours the cubic-structured γ-MoN_x and partially ordered pseudo-cubic γ'-MoN_x, which becomes energetically preferable especially in the vicinity of 3:2 stoichiometry, i. e., *x* = 0.67.

The phase evolution observed experimentally with increasing nitrogen partial pressure used deposition is illustrated in Fig. 17 (colour-coded in agreement with the **Publication #1**):

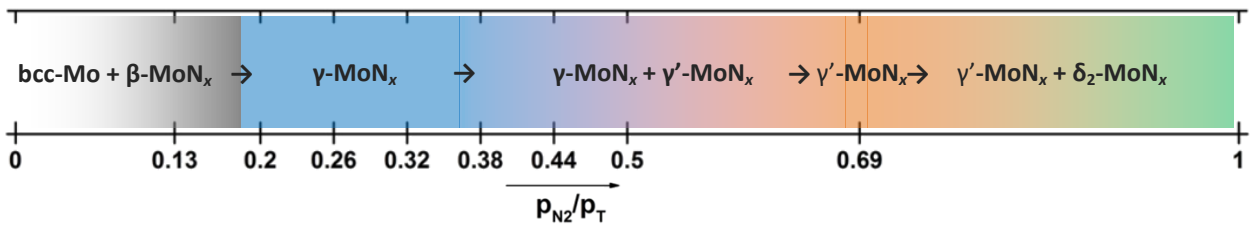

Fig. 17. Phase evolution within Mo–N system based on the nitrogen partial pressure used during deposition.

The deviation from the calculations (dominating of γ-MoN_x over β-MoN_x) can easily be explained by the fact that the calculations were performed at 0 K. Nitrogen sublattice of the cubic γ-MoN_x, unlike the majority of B1-structured transition metal nitrides, consists to 50% of vacancies, x = 0.5, which are furthermore randomly distributed. Due to that fact, elevated temperatures would increase the entropy term, $T{\cdot}S$, lowering, thus, the Gibbs free energy, G, according to $G = H - T{\cdot}S$. Nevertheless, at extremely low p_{N2}/p_T-ratio, β-MoN_x forms next to bcc-Mo. In contrast to thermodynamic equilibrium with the homogeneity range for cubic γ-MoN_x of ~28-35 at.% N (x = 0.39 – 0.54), the single-phase range of synthesised metastable cubic γ-MoN_x is stretched in a greater extent towards higher nitrogen vacancies concentrations, ~20-34 at.% N (x = 0.33 – 0.53), due to constrained adatoms mobility during deposition.

In contrast, only slightly overstoichiometric γ-MoN_x with x^{max} = 0.53 (as revealed by elastic recoil detection analysis) is achievable, since further occupation of the N-vacant sites results in partial ordering of the vacancies, indicating formation of coherent domains of pseudo-cubic ϕ-MoN_x, in the matrix of cubic γ-MoN_x (as evidenced by superstructure reflexes observed experimentally on the XRD and SAED patterns). With rising nitrogen partial pressure, domains of partially ordered γ'-MoN_x continue evolving, becoming consequently matrix and enveloping γ-MoN_x when approaching overall N-content of 40 at.%, whereby Mo–N crystallizes as single-phase pseudo-cubic γ'-$MoN_{0.67}$ with partially ordered nitrogen vacancies. Coatings, deposited only in N-atmosphere, reveal the hexagonal δ_1-MoN_x next to γ'-MoN_x.

Relying on our experimental (elemental composition and stress-free lattice parameter) as computational, we state that partially ordered pseudo-cubic γ'-MoN_x (γ'-Mo_3N_2 or γ'-$MoN_{0.67}$) forms with only one partially vacant sublattice (*N-vacancy-rich NaCl-type*, γ'-MoN_x), but not, as previously believed, with both partially vacant sublattices (*N-vacancy-rich NbO-type,* γ''-MoN_x). With other words, partially ordered pseudo-cubic γ'-MoN_x exhibits NaCl-type crystal structure with ~33 % vacancies on the N-sublattice, but not with 25 and 50 % vacancies on the Mo- and N-sublattices, respectively (the latter can be also thought of as NbO-type with additional nitrogen vacancies).

The highest indentation hardness of ~33 GPa, related to the slightly overstoichiometric single-phase γ-$MoN_{0.53}$, deteriorates with reducing vacancies concentration due to the partial vacancy ordering, i.e., development of pseudo-cubic γ'-$MoN_{0.67}$ (~28 GPa). The softening is in excellent agreement with the valence electron concentration (VEC) empirical criterion, since phase transition γ-$MoN_{0.53}$ → γ'-$MoN_{0.67}$ increases the valence electron concentration per unit cell from 8.5 to ~9.4, hence, moving away from 8.4, at which the highest hardness is observed for numerous material systems.

In summary, the hardness (and empirically predicated wear protection) of γ-MoN_x depend strongly on the concentration of the nitrogen vacancies and shows maximum of ~33 GPa for γ-$MoN_{0.53}$., having the closet VEC-value to 8.4 (8.6). Further occupation of N-vacancies results in their partial ordering, i.e., formation of coherent domains of pseudo-cubic ordering phase γ'-$MoN_{0.67}$, exhibiting hardness of ~28 GPa. Hence, approach of 2:1 stoichiometry and preservation of a random distribution of N-vacancies are essential for optimized hardness of γ-MoN_x.

3.2. Composition driven phase evolution and mechanical properties of Mo–Cr–N hard coatings

(See **Publication #2** for details [170])

The two main purposes of the current research were to investigate the impact of:

1) Chromium additions on the microstructure, and particularly on the nitrogen vacancy concentration, as well as micromechanical properties of cubic γ-MoN_x

2) Additional alteration of the nitrogen vacancy concentration of ternary nitrides $Mo_{1-x}Cr_xN_y$ by varying nitrogen partial pressure used during deposition on their microstructural and micromechanical properties.

Formation of fcc-$Mo_{1-x}Cr_xN_{0.5(1+x)}$ within 0 < x < 1, which reveals the inherent driving force of Mo–Cr–N system to prefer N-vacancies as long as molybdenum is present, unless high nitrogen partial pressure is used during synthesis, resulting in rapid vacancy occupation and subsequent structure evolution according to fcc-$Mo_{1-x}Cr_xN$ (for $x > x^{vac\text{-}free}$, p_{N2}/p_T-dependent). High vacancy concentration combined with low Cr-content enhances mechanical properties – the main conclusions, summarizing our findings in the present research work.

Though the nitrides of molybdenum and chromium, belonging to group VI TMNs, can both crystallize – according to their phase diagrams – in cubic B1-type structure with similar lattice constants (4.163 Å and 4.148 Å, respectively) and should, hence, form solid solution within the entire composition range, the inherent driving force of molybdenum nitride to form with vacancy-rich non-metal sublattice (only half of all the octahedral voids of molybdenum are occupied by nitrogen) excites a great deal of interest for atomic-scaled investigations.

The focus of investigations was narrowed to the Mo-rich compositions of $Mo_{1-x}Cr_xN_y$, deposited at three different p_{N2}/p_T-ratios (low, 0.32, moderate, 0.44, and high, 0.69). Addition of chromium results in formation of single-phase solid solutions – necessary prerequisite for high thermal stability and oxidation resistance – with nanometer-scaled coherently scattering domains (10-30 nm). At low and moderate N-to-total pressure ratios used during deposition, structural development of the solid solutions follows $MoN_{0.5}$–CrN tie line, revealing the inherent driving force of the material system to prefer N-vacancies as long as molybdenum is present. The nearly linear increase of the nitrogen content can best described with the chemical formula $Mo_{1-x}Cr_xN_{0.5(1+x)}$, indicating population of one nitrogen vacancy for every two substitutions of Mo- with Cr-ions on the metal sublattice. In contrast, higher nitrogen partial pressures during deposition process result in rapid occupation of the partially vacant N-sublattice approaching MoN–CrN tie line, i.e., forming vacancy-free $Mo_{1-x}Cr_xN$ at relatively low Cr-concentrations ($x \approx 0.4$ at $p_{N2}/p_T = 0.69$). Higher Cr-concentrations result apparently in nitrogen overstoichiometric compositions (as shown for Cr–N, nitrogen overstoichiometries are equally probable by means of occupation of interstitial and anti-site positions, or formation of Cr-vacancies).

According to the VEC empirical criterion, alloying with Cr along the tie line $MoN_{0.5}$–CrN is accompanied by increasing VEC per unit cell from 8.5 ($MoN_{0.5}$) to 11 (CrN), that predicts an improved ductility of forming solid solution, though their softening as well. The highest

indentation hardness, *H*, of ~33-34 GPa exhibit the coatings synthesised using low nitrogen partial pressure and containing low amount of chromium, $x < 0.19$ (*fcc-*$Mo_{0.81}Cr_{0.19}N_{0.52}$). Apart from that, virtually all synthesised Mo-rich ternaries exhibit indentation hardness in the range 28 – 31 GPa, wherein materials become in general gradually harder with reducing nitrogen partial pressure used during deposition and tend moreover to strength with low Cr-additions. The indentation moduli, *E*, vary for all ternaries in the range 390 – 410 GPa without being significant influenced by Cr-content. Because of the different behaviour of *H* and *E*-values for Cr- and N-deficient coatings, the hardest coating *fcc-*$Mo_{0.81}Cr_{0.19}N_{0.52}$ (~34 GPa) was found to exhibit highest resistance against plastic deformation with $H^3/E^2 \approx 0.2$ GPa.

In summary (Fig. 18), in order to extend the temperature range of application of the γ-MoN_x-based materials, the concept of alloying with chromium was developed, since elevated temperatures (e.g., during dry cutting) result in formation of a dense oxide scale Cr_2O_3 on the coating surface, preventing oxygen inward diffusion and protecting molybdenum from formation of volatile oxides. The B1-structured γ-$MoN_{0.5}$ and c-CrN show complete mutual solubility forming quasi-binary solid solutions $Mo_{1-x}Cr_xN_y$ in a wide range of nitrogen partial pressure used during deposition. However, while moderate and especially low p_{N2}/p_T-values alter their elemental composition in a good agreement with $Mo_{1-x}Cr_xN_{0.5(1+x)}$, high p_{N2}/p_T-ratios lead to a rapid occupation of the N-sublattice with increasing Cr-content, forming subsequently $Mo_{1-x}Cr_xN$ solid solutions. The enhanced micromechanical properties were observed for the vacancy-rich structures with low Cr-concentrations, and particularly for c-$Mo_{0.81}Cr_{0.19}N_{0.52}$ with the highest indentation hardness (~34 GPa) and resistance to plastic deformation (0.2 GPa) among all studied ternary nitrides $Mo_{1-x}Cr_xN_y$.

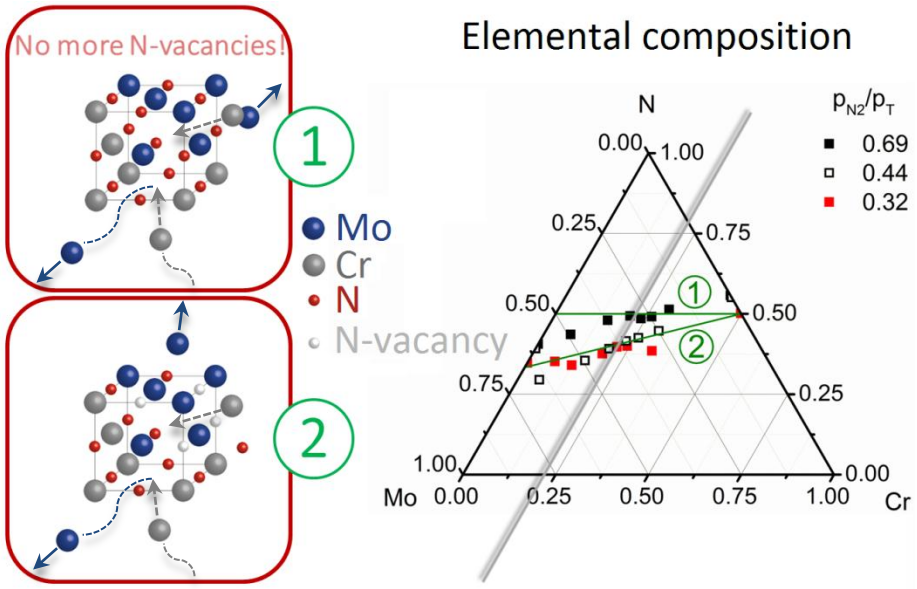

Fig. 18. Elemental composition evolution along the tie lines MoN–CrN (1) and $MoN_{0.5}$–CrN (2). Coatings, prepared using high/moderate/low p_{N2}/p_T-ratios coloured black/white/red. Two red boxes on the left correspond to the Cr-content, *x*, indicated on the concentration triangle with the gray line (~0.22).

3.3. Computational and experimental studies on structure and mechanical properties of Mo–Al–N

(See **Publication #3** for details [171])

Similar to chromium, the concept of alloying with aluminium is aimed at improving oxidation and thermal stabilities of γ-MoN_x, in order to shift the application limit to higher temperatures. Different to chromium, aluminium nitride is known to crystallize with hexagonal crystallographic structure, thus, being in thermodynamic equilibrium immiscible with cubic-structured γ-MoN_x. The high-temperature high-pressure allotropy of h-AlN, namely fcc-AlN, is highly difficult to stabilize, even using non-equilibrium PVD technique (see chapter 1.7.). Guided by the results of our *ab initio* investigations (performed by *Holger Euchner*) and using reactive magnetron sputtering technique, we were focused on synthesis of (hitherto unachievable) Al-rich single-phase cubic-structured metastable solid solutions $Mo_{1-x}Al_xN_y$ within the poorly investigated Mo–Al–N material system.

Nitrogen vacancies play the key role in formation of hard Al-rich fcc-$Mo_{1-x}Al_xN_y$. The benchmark in solving Al in fcc-$Mo_{1-x}Al_xN_y$ was set to $x \approx 0.57$ – the main two conclusions drawn from our findings in the present study, illustrated graphically in Fig. 19 (used as graphical abstract to **Publication #3**).

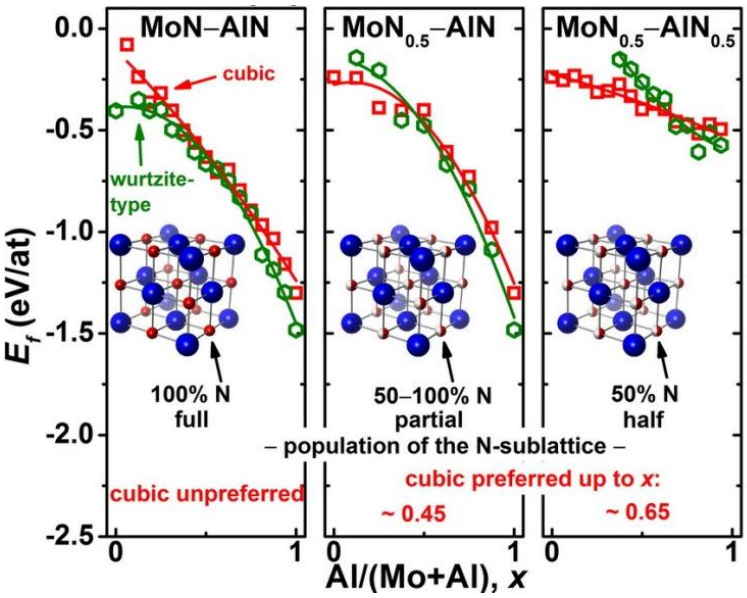

Fig. 19. Dependence of the cubic phase formation on the N-sublattice population [171].

While the vacancy-free compositions along the MoN–AlN tie line favour the hexagonal-structured $Mo_{1-x}Al_xN$ to form for any *x*, generation of vacancies on the nitrogen sublattice allows $Mo_{1-x}Al_xN_y$ to crystallize with cubic structure. The threshold Al-concentration for the cubic-hexagonal phase transition is directly related to the nitrogen vacancy concentration, shifting the E_f-curves intersection point from x ≈ 0.45 (for partially occupied N-sublattice, i.e., $Mo_{1-x}Al_xN_{0.5(1+x)}$) to ~0.65 (for highly defected $Mo_{1-x}Al_xN_{0.5}$, having persistently 50% vacancies on the non-metal-sublattice independent of Al-content).

Applying the gained knowledge, we have proceeded with the experimental part, generating nitrogen-deficient atmosphere during reactive sputtering. By doing this, we were able to synthesise single-phase cubic-structured solid solutions, fcc-$Mo_{1-x}Al_xN_y$, along the $MoN_{0.5}$–AlN tie line, suggesting partial occupation of the N-sublattice as a function of Al-content, $y = 0.5(1+x)$. This indicates (similar to quasi-binary fcc-$Mo_{1-x}Cr_xN_{0.5(1+x)}$) that one octahedral void becomes occupied by nitrogen for each two substitutions of Mo- with Al-ions on the metal sublattice. The maximum Al-solubility on the metal sublattice of fcc-$Mo_{1-x}Al_xN_{0.5(1+x)}$ was measured to be ~57 at.% (*fcc-*$Mo_{0.43}Al_{0.57}N_{0.80}$) – currently the highest Al-concentration reached for fcc-$Mo_{1-x}Al_xN_y$. Higher Al-contents and related lower N-vacancy concentrations, i.e., approach of the vacancy-free composition ($y = 1$), trigger the development of the hexagonal structure next to the cubic one due to contraction of formation energy benefit for the cubic structure.

According to the VEC empirical criterion, alloying with Al along the $MoN_{0.5}$–AlN tie line is accompanied by marginally increasing VEC per unit cell from 8.5 ($MoN_{0.5}$) to 9 (AlN), predicting formation of hard ternary nitrides. Indeed, all ternary fcc-$Mo_{1-x}Al_xN_{0.5(1+x)}$ exhibit indentation hardness values above ~33 GPa, though higher Al-concentrations harden fcc-$Mo_{1-x}Al_xN_{0.5(1+x)}$ significantly resulting in maximum of ~38 GPa for the highest aluminium concentration, *fcc-*$Mo_{0.43}Al_{0.57}N_{0.80}$. The hexagonal phase development for $x > 0.67$ deteriorates the coatings hardness dramatically from ~38 to 22 GPa. The indentation moduli of the ternary nitrides show nearly the same tendency, increasing first from ~410 to 480 GPa with increasing Al-content, but drops to ~245 GPa for the coatings with evolving hexagonal phases.

In summary, backing up the first principle calculations with solid empirical evidence we carried out comprehensive structural investigations of Mo–Al–N material system and discovered the decisive role of the nitrogen vacancies in synthesis of cubic-structured Al-rich metastable solid solutions. Reactive magnetron sputtering in the N-deficient atmosphere allowed us to synthesise fcc-$Mo_{1-x}Al_xN_{0.5(1+x)}$ with partial occupation of the N-sublattice up to very high Al-contents, $x \approx 0.57$ – hitherto the highest Al-solubility in $Mo_{1-x}Al_xN_y$. It's worth mentioning, that this threshold Al-concentration, as shown in our *ab initio* calculations, can be shifted even to higher values on account of higher N-vacancy concentration. Overcoming the threshold Al-concentration, which is related to the E_f-curves intersection point, hexagonal phase start becomes energetically favourable. High Al-concentrations harden (and stiffen) $Mo_{1-x}Al_xN_y$ resulting in maximum ~38 GPa (~480 GPa) at the threshold $x \approx 0.57$, *fcc-*$Mo_{0.43}Al_{0.57}N_{0.80}$, which dramatically drop to ~22 GPa (~245 GPa) for the dual-phased coatings ($x > 0.67$). Therefore, tuning the N-vacancy concentration, fcc-$Mo_{1-x}Al_xN_y$ can be stabilized up to very high Al-contents – prerequisite for improved strength and thermal stability.

.

3.4. Synthesis of the super-hard Mo–Al–Cr–N coatings: *ab initio*-guided empirical approach

(See **Publication #4** for details [172])

Applying the knowledge gained in our recent investigations of the binary MoN_y and the ternaries $Mo_{1-x}Cr_xN_y$ and $Mo_{1-x}Al_xN_y$ [169-171] we aimed at synthesise of hard quaternary Al-rich Mo–Al–Cr–N nitrides with optimized elemental composition. Indentation hardness, *H*, and modulus, *E*, as well as empirical criteria VEC (toughness), *H*/*E* (elastic strain to failure), H^3/E^2 (resistance to the plastic deformation) were used to characterize mechanical properties.

Synthesis of the Al-rich/Cr-poor quaternaries fcc-$Mo_{1-x-y}Al_xCr_yN_z$ in the nitrogen-deficient atmosphere yield the superhardness combined with (expected) good toughness and excellent wear protection – is the most significant result obtained in this research work.

Reactively sputtered single-phase cubic-structured fcc-$Mo_{1-x-y}Al_xCr_yN_z$ with up to very high Al-content ~0.5-0.6 (depending on Cr-content), while further Al-enrichment favours the formation of the hexagonal structure, see Fig. 20. High Al-contents of γ-MoN_x-based quaternaries, which result in enhanced material strength, could be achieved because of the nitrogen-deficient atmosphere used during deposition processes and resulted high concentration of the nitrogen vacancies, shown in our previous study on Mo–Al–N to stabilize the cubic structure [171]. Combining with low Cr-concentrations, Al-rich fcc-$Mo_{1-x-y}Al_xCr_yN_z$ coatings exhibit hardness of ~40 GPa (which drastically drops to ~20 GPa in the dual-phased regions). The super-hard fcc-$Mo_{0.39}Al_{0.52}Cr_{0.09}N_{0.98}$ exhibits the highest hardness, *H*, of ~41 GPa among all coatings studied, which in combination with a relatively low indentation modulus, *E*, results in the highest empirical criteria *H*/*E* and H^3/E^2 (0.1 and 0.35, respectively), suggesting for excellent wear protection. Together with improved toughness typical for high-VEC materials (VEC increases from 8.7 for γ-$MoN_{0.53}$ to 9.3 for fcc-$Mo_{0.39}Al_{0.52}Cr_{0.09}N_{0.98}$), our super-hard fcc-$Mo_{0.39}Al_{0.52}Cr_{0.09}N_{0.98}$ shows a high potential for severe applications.

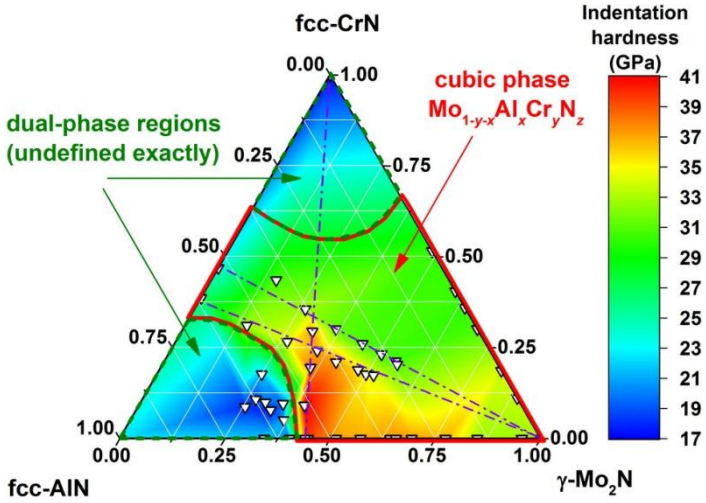

Fig. 20. Ternary contour of indentation hardness of the coatings within Mo–Al–Cr–N material system with indicated single- and dual-phased regions. The violet dash-dotted lines indicate the hardness evolution of fcc-$Mo_{1-x-y}Al_xCr_yN_z$ along three different tie lines.

3.5. Vacant positions in MONTAN: Vacancy-driven evolution of structure and mechanical properties of hard Mo–Ta–N

(See **Publication #5** for details [173])

Motivated by the previous studies on the vacancy-rich substoichiometric nitrides (with nitrogen/metal-ratio <1) and by the recent sophisticated computational findings within the vacancy-rich MoN_x and Ta_xN we have combined computational and experimental materials science to provide thorough insights into the vacancy-related crystallographic changes within the Mo–Ta–N material system.

Nitrogen-deficient sputtering atmosphere causes the formation of fcc-$Mo_mTa_xN_n$ for $0 < x < 0.7$ and a mixture of cubic and hexagonal phases for $x > 0.7$. Within the fcc-$Mo_mTa_xN_n$, in turn, the two-stage structural development is revealed:

a) **for Mo-rich compositions (x < 0.5) – along the quasi-binary tie line $MoN_{0.5}$–$Ta_{1-y}N_{1-y}$ ($Ta_{1-y}N_{1-y}$ = Schottky defects), i.e., fcc-$Mo_{1-x}Ta_xN_{0.5(1-x)}$ with $x = 1 - y$;**

b) **for Ta-rich compositions (x > 0.5) – along the quasi-binary tie line $Mo_{0.78}N$–$Ta_{0.78}N$, i.e., fcc-$Mo_{0.78(1-x)}Ta_{0.78x}N$.**

Ta-enrichment enhances hardness as long as Me-sublattice remains occupied (a), reaching maximum ~36 GPa for the threshold Ta-content, but softens materials with Me-vacancies (b) – a brief summary of the final part of the thesis, also shown in Fig. 21.

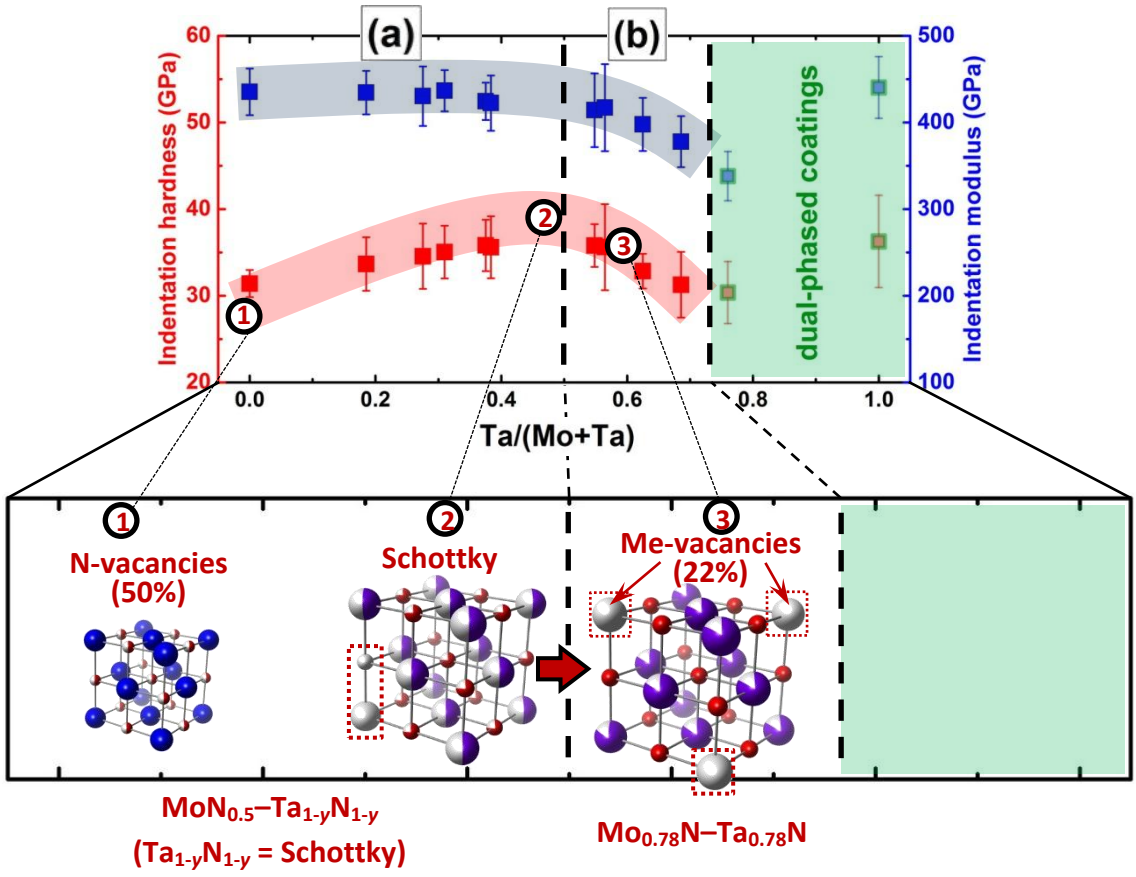

Fig. 21. Graphical illustration of the phase evolution within the Mo–Ta–N material system synthesised in N-deficient atmosphere and related indentation hardness and modulus.

Using reactive sputtering, we fused two binary nitrides, Mo–N and Ta–N, i.e., two material systems with their inherent driving force to crystallize with high concentration of vacancies. However, while cubic Mo–N prefers vacancies at the N-sublattice (γ-MoN_x), the low-energy cubic Ta–N forms with partially vacant *Me*-sublattice (δ-Ta_xN). When sputtering in nitrogen-deficient atmosphere, we could stabilize the cubic-structured quasi-binary fcc-$Mo_mTa_xN_n$ up to x ≈ 0.7, while beyond that threshold Ta-concentration, a mixture of cubic and hexagonal phases develops. Putting the main emphasis on the single-phase cubic structures, we carried out first principle calculations, to compare the energies of formation of different defected structures (at the reduced nitrogen chemical potential, corresponding to our nitrogen-deficient sputtering conditions) and to describe the structural development with increasing Ta-concentrations.

Putting computational and experimental results together, the two-stage structural development within the fcc-$Mo_mTa_xN_n$ was revealed:

(a) Mo-rich compositions (x < ~0.5) force the structure to develop along the quasi-binary $MoN_{0.5}$–$Ta_{1-y}N_{1-y}$ tie line ($Ta_{1-y}N_{1-y}$ indicates Schottky defects), i.e., in agreement with the chemical formula fcc-$Mo_{1-x}Ta_xN_{0.5(1-x)}$ (x = 1 - y).
Since the concentration of low-energy Schottky defects is only ~6%, experimentally they can easily be confused with the defect-free structure, δ-TaN, which is, however, clearly energetically inferior to that with ~6% Schottky defects.

(b) Ta-rich compositions (x > ~0.5) force the structure to develop along the quasi-binary $Mo_{0.78}N$–$Ta_{0.78}N$ tie line, i.e., forming vacancies at the *Me*-sublattice in excellent agreement with the chemical formula fcc-$Mo_{0.78(1-x)}Ta_{0.78x}N$.

The threshold Ta-concentration within the two-stage structural development of fcc-$Mo_mTa_xN_n$ (x ≈ 0.5) is mainly determined by the nitrogen vacancies concentration, as derived from the reduced nitrogen chemical potential and related formation energies, $E_f(\mu_N\text{-}\mu_N(N_2))$. However, it is worth mentioning that any alteration of the metallic chemical potentials will certainly influence the threshold Ta-concentration as well. The Ta-concentration is, in turn, crucial in whether the structure formed consist of vacancies at the N-sublattice (with up to 6% vacancies on the *Me*-sublattice with increasing Ta-content to the threshold concentration due to Schottky defects) or at the *Me*-sublattice.

Ta-enrichment enhances indentation hardness, H, as long as *Me*-sublattice remains occupied (a), reaching maximum ~36 GPa for the threshold Ta-content, but softens materials with *Me*-vacancies (b). Due to the different behaviour of the indentation modulus, E, for fcc-$Mo_{1-x}Ta_xN_{0.5(1-x)}$ (x = 1 - y), which remains unaltered with increasing Ta-content, the coating with the highest hardness is also suggested (by empirical criteria H/E, H^3/E^2) to demonstrate the best wear protection.

Summarizing, the atomic-scale understanding of a complex nature of materials with inherent driving force to form vacancies at both sublattices, such as Mo–Ta–N, – a key for the macroscopic properties tuning. A very effective approach for this challenge is the combination of computational and experimental materials science.

4. Conclusions

In the framework of this thesis, supporting experiments with *ab initio* calculations, the impact of vacancies on evolution of phase composition and mechanical properties of substoichiometric Mo-based nitride materials was investigated.

The metastable cubic γ-MoN_x, with the homogeneity range stretched towards the higher vacancy concentrations, x = 0.33 – 0.53, exhibits the highest hardness of ~33 GPa for γ-$MoN_{0.53}$, i.e., experimentally closest composition to VEC per unit cell of 8.4. Occupation of the initially randomly distributed vacancies at the nitrogen sublattice of γ-MoN_x, (x > 0.53), results in their partial ordering, i.e., formation of the coherent domains of the partially ordered pseudo-cubic, softer γ'-$MoN_{0.67}$ (~28 GPa). The use of the same optimized p_{N2}/p_T-ratio during sputtering (combined with low amount of chromium) was also shown to be decisive for the hardness enhancement within Mo–Cr–N system, where both cubic structures show complete mutual solubility at any p_{N2}/p_T-ratio, even despite the significant difference in occupation of N-sublattice. Nitrogen-deficient atmospheres favour formation of solid solutions fcc-$Mo_{1-x}Cr_xN_{0.5(1+x)}$ exhibiting inherent driving force to prefer N-vacancies as long as molybdenum is present, while sputtering using high p_{N2}/p_T-ratios causes rapid population of vacancies and formation of solid solutions fcc-$Mo_{1-x}Cr_xN$ (for $x > x^{vac\text{-}free}$, p_{N2}/p_T-dependent). Nitrogen vacancies play furthermore the key role in formation of Al-rich fcc-$Mo_{1-x}Al_xN_y$. Aluminium in turn is essential for improved material hardness and oxidation resistance. The N-deficient sputtering atmosphere allowed us setting benchmark in solving Al in fcc-$Mo_{1-x}Al_xN_y$ to $x \approx 0.57$, resulted simultaneously in the highest hardness of ~38 GPa. Finally, the accumulated knowledge was applied to synthesise quaternaries fcc-$Mo_{1-x-y}Al_xCr_yN_z$ in the nitrogen-deficient atmosphere with hardness of ~40 GPa, but high-potential super-hard fcc-$Mo_{0.39}Al_{0.52}Cr_{0.09}N_{0.98}$ (~41 GPa) with predicted good toughness and excellent wear protection as well.

Hence, the search for novel multifunctional materials demonstrating the sought-after performance becomes streamlined when combining experimental and computational approaches. Such conjunction provides thorough insights into the complex nature of the substoichiometric nitrides, and particularly highly promising Mo-based nitride materials synthesised in the framework of this thesis, revealing, i.a., the determining role of the nitrogen vacancies (and vacancies in general) in structure development. The understanding of the processes on the atomic scale is, in turn, a most powerful properties-tuning tool.

Figures

References

[1] K. Bobzin. Oberflächentechnik für den Maschinenbau, John Wiley & Sons, 2013.

[2] The World Bank, http://data.worldbank.org/ (accessed on 22.01.2016).

[3] P.M. Martin. Handbook of deposition technologies for films and coatings: science, applications and technology, William Andrew, 2009.

[4] Bundesministerium für Forschung und Technologie. Damit Rost und Verschleiß nicht Milliarden fressen: Fortschritt durch Forschung, BMFT, Referat Presse und Öffentlichkeitsarbeit, 1983.

[5] F.J. Momper, W. Heinrich, J. Farby, Kennametal Hertel AG Fürth. Scheidstoffe für moderne Werkstoffe. in: Ruthardt R, (Ed.). Pulvermetallurgie in Wissenschaft und Praxis, Band 13: Hartstoffe, Hartstoffschichten, Werkzeuge, Verschleißschutz, vol. 13. Frankfurt, 1997. pp. 213-230.

[6] P.H. Mayrhofer, C. Mitterer, L. Hultman, H. Clemens. Microstructural design of hard coatings, Progress in Materials Science 51 (2006) 1032-1114.

[7] R. Haubner, B. Lux. CVD-Beschichtungen von Werkzeugen. in: Ruthardt R, (Ed.). Pulvermetallurgie in Wissenschaft und Praxis, Band 13: Hartstoffe, Hartstoffschichten, Werkzeuge, Verschleißschutz, vol. 13. Frankfurt, 1997. pp. 89-116.

[8] W. König, R. Fritsch, O. Knotek, G. Krämer. Arc-PVD-Beschichtung von Hartmetallen und Analyse des funktionellen Verhaltens beim Zerspanen im unterbrochenen Schnitt, Materialwissenschaft und Werkstofftechnik 24 (1993) 131-141.

[9] P.H. Mayrhofer, M. Geier, C. Löcker, L. Chen. Influence of deposition conditions on texture development and mechanical properties of TiN coatings, International journal of materials research 100 (2009) 1052-1058.

[10] W. Westwood. Sputter Deposition (AVS Education Committee Book Series vol 2), AVS, New York, ISBN: 0-7354-0105-5 (2003).

[11] N. Laegreid, G.K. Wehner. Sputtering Yields of Metals for Ar+ and Ne+ Ions with Energies from 50 to 600 ev, Journal of Applied Physics 32 (1961) 365.

[12] J.A. Thornton. High rate thick film growth, Annual review of materials science 7 (1977) 239-260.

[13] D.M. Mattox. Handbook of physical vapor deposition (PVD) processing, William Andrew, 2010.

[14] H. Holleck. Advanced concepts of PVD hard coatings, Vacuum 41 (1990) 2220-2222.

[15] J.A. Thornton. High rate sputtering techniques, Thin Solid Films 80 (1981) 1-11.

[16] A.I.H. Committee. ASM handbook: Surface engineering, ASM International, 1994.

[17] P.H. Mayrhofer. Oberflächentechnik / Surface Technology. Lecture notes: First edition, 2013.

[18] I. Petrov, P. Barna, L. Hultman, J. Greene. Microstructural evolution during film growth, Journal of Vacuum Science & Technology A 21 (2003) S117-S128.

[19] P. Barna, M. Adamik. Fundamental structure forming phenomena of polycrystalline films and the structure zone models, Thin Solid Films 317 (1998) 27-33.

[20] D. Sangiovanni, F. Tasnádi, L. Hultman, I. Petrov, J. Greene, V. Chirita. N and Ti adatom dynamics on stoichiometric polar TiN (111) surfaces, Surface Science 649 (2016) 72-79.

[21] F. Baumann, D. Chopp, T.D. de la Rubia, G. Gilmer, J. Greene, H. Huang, S. Kodambaka, P. O'sullivan, I. Petrov. Multiscale modeling of thin-film deposition: applications to Si device processing, Mrs Bulletin 26 (2001) 182-189.

[22] B. Movchan, A. Demchishin. Structure and properties of thick condensates of nickel, titanium, tungsten, aluminum oxides, and zirconium dioxide in vacuum, Fiz. Metal. Metalloved. 28: 653-60 (Oct 1969).
[23] J.A. Thornton. Influence of apparatus geometry and deposition conditions on the structure and topography of thick sputtered coatigns, J Vac Sci Technol 11 (1974) 666-670.
[24] A. Anders. A structure zone diagram including plasma-based deposition and ion etching, Thin Solid Films 518 (2010) 4087-4090.
[25] R.F. Bunshah. Handbook of deposition technologies for films and coatings: science, technology, and applications, William Andrew, 1994.
[26] E. Hall. The deformation and ageing of mild steel: III discussion of results, Proceedings of the Physical Society. Section B 64 (1951) 747.
[27] N. Petch. The cleavage strength of polycrystals, J. Iron Steel Inst. 174 (1953) 25-28.
[28] A. Chokshi, A. Rosen, J. Karch, H. Gleiter. On the validity of the Hall-Petch relationship in nanocrystalline materials, Scripta Metallurgica 23 (1989) 1679-1683.
[29] R. Bunshah. Structure/property relationships in evaporated thick films and bulk coatings, Journal of Vacuum Science & Technology 11 (1974) 633-638.
[30] H.O. Pierson. Handbook of Refractory Carbides & Nitrides: Properties, Characteristics, Processing and Apps, William Andrew, 1996.
[31] H. Holleck. Material selection for hard coatings, J. Vac. Sci. Technol., A 4 (1986) 2661-2669.
[32] S.-H. Jhi, S.G. Louie, M.L. Cohen, J. Ihm. Vacancy hardening and softening in transition metal carbides and nitrides, Physical Review Letters 86 (2001) 3348.
[33] A.I. Gusev, A.A. Rempel, A.J. Magerl. Disorder and order in strongly nonstoichiometric compounds: transition metal carbides, nitrides and oxides, Springer Science & Business Media, 2013.
[34] L. Toth. Transition Metal Carbides and Nitrides (Academic, New York, 1971), and references therein (1992) 87.
[35] D.A. Porter, K.E. Easterling, M. Sherif. Phase Transformations in Metals and Alloys, (Revised Reprint), CRC press, 2009.
[36] L. Hultman. Thermal stability of nitride thin films, Vacuum 57 (2000) 1-30.
[37] C.L. Rollinson. The Chemistry of Chromium, Molybdenum and Tungsten: Pergamon International Library of Science, Technology, Engineering and Social Studies, Elsevier, 2015.
[38] M.T. Baben, L. Raumann, D. Music, J.M. Schneider. Origin of the nitrogen over- and understoichiometry in $Ti_{0.5}Al_{0.5}N$ thin films, J. Phys. Condens. Matter. 24 (2012) 155401.
[39] D. Holec, L. Zhou, Z. Zhang, P.H. Mayrhofer. Impact of point defects on the electronic structure of paramagnetic CrN, arXiv preprint arXiv:1410.0758 (2014).
[40] L. Tsetseris, N. Kalfagiannis, S. Logothetidis, S. Pantelides. Role of N defects on thermally induced atomic-scale structural changes in transition-metal nitrides, Physical review letters 99 (2007) 125503.
[41] X. Jiang, M. Wang, K. Schmidt, E. Dunlop, J. Haupt, W. Gissler. Elastic constants and hardness of ion-beam-sputtered TiN_x films measured by Brillouin scattering and depth-sensing indentation, Journal of applied physics 69 (1991) 3053-3057.
[42] Z. Zhang, H. Li, R. Daniel, C. Mitterer, G. Dehm. Insights into the atomic and electronic structure triggered by ordered nitrogen vacancies in CrN, Physical Review B 87 (2013) 014104.
[43] R.W. Cahn, P. Haasen. Physical metallurgy. Vol. 2, North-Holland, 1996.
[44] W. Kern. Thin film processes II, Academic press, 2012.
[45] S. Veprek. Recent search for new superhard materials: Go nano!, Journal of Vacuum Science & Technology A: Vacuum, Surfaces, and Films 31 (2013) 050822.
[46] H. Riedl, C. Koller, F. Munnik, H. Hutter, F.M. Martin, R. Rachbauer, S. Kolozsvári, M. Bartosik, P. Mayrhofer. Influence of oxygen impurities on growth morphology, structure and mechanical properties of Ti-Al-N thin films, Thin Solid Films (2016).
[47] A. Roth. Vacuum technology, Elsevier, 2012.
[48] H. Holleck, Schier. Multilayer PVD coatings for wear protection, Surface and Coatings Technology 76 (1995) 328-336.
[49] P.H. Mayrhofer, C. Mitterer, H. Clemens. Self-Organized Nanostructures in Hard Ceramic Coatings, Advanced Engineering Materials 7 (2005) 1071-1082.

[50] G. de Portu, S. Guicciardi. 2.14 - Wear of Hard Ceramics A2 - Sarin, Vinod K. Comprehensive Hard Materials. Elsevier, Oxford, 2014. pp. 385-412.
[51] M. Ashby. Materials selection in mechanical design: Fourth edition, 2010.
[52] S.-H. Jhi, J. Ihm, S.G. Louie, M.L. Cohen. Electronic mechanism of hardness enhancement in transition-metal carbonitrides, Nature 399 (1999) 132-134.
[53] H. Bilz. Über Elektronenzustände von Hartstoffen mit Natriumchloridstruktur, Zeitschrift für Physik 153 (1958) 338-358.
[54] S. Pugh. XCII. Relations between the elastic moduli and the plastic properties of polycrystalline pure metals, The London, Edinburgh, and Dublin Philosophical Magazine and Journal of Science 45 (1954) 823-843.
[55] D. Pettifor. Theoretical predictions of structure and related properties of intermetallics, Materials science and technology 8 (1992) 345-349.
[56] D.G. Sangiovanni, L. Hultman, V. Chirita. Supertoughening in B1 transition metal nitride alloys by increased valence electron concentration, Acta Materialia 59 (2011) 2121-2134.
[57] L. Zhou, H. David, P.H. Mayrhofer. Ab initio study of the alloying effect of transition metals on structure, stability and ductility of CrN, J. Phys. D: Appl. Phys. 46 (2013) 365301.
[58] H. Kindlund, D. Sangiovanni, J. Lu, J. Jensen, V. Chirita, J. Birch, I. Petrov, J. Greene, L. Hultman. Vacancy-induced toughening in hard single-crystal $V_{0.5}Mo_{0.5}N_x$/MgO (001) thin films, Acta Materialia 77 (2014) 394-400.
[59] D.G. Sangiovanni. Toughness enhancement in transition metal nitrides, (2011).
[60] A. Dietzel. Die Kationenfeldstärken und ihre Beziehungen zu Entglasungsvorgängen, zur Verbindungsbildung und zu den Schmelzpunkten von Silicaten, Z. Elektrochem 48 (1942) 9-23.
[61] A. Erdemir. A crystal-chemical approach to lubrication by solid oxides, Tribology Letters 8 (2000) 97-102.
[62] A. Öztürk, K. Ezirmik, K. Kazmanlı, M. Ürgen, O. Eryılmaz, A. Erdemir. Comparative tribological behaviors of TiN, CrN and MoN Cu nanocomposite coatings, Tribology International 41 (2008) 49-59.
[63] L. Zhou, D. Holec, P.H. Mayrhofer. Ab initio study of the alloying effect of transition metals on structure, stability and ductility of CrN, J. Phys. D: Appl. Phys. 46 (2013) 365301.
[64] G. Gassner, P.H. Mayrhofer, K. Kutschej, C. Mitterer, M. Kathrein. Magnéli phase formation of PVD Mo–N and W–N coatings, Surface and Coatings Technology 201 (2006) 3335-3341.
[65] A. Magnéli. Structures of the ReO_3-type with recurrent dislocations of atoms:homologous series' of molybdenum and tungsten oxides, Acta Crystallographica 6 (1953) 495-500.
[66] W.D. Callister, D.G. Rethwisch. Materials science and engineering. Ninth edition ed., Wiley New York, 2014.
[67] A. Voevodin, S. Prasad, J. Zabinski. Nanocrystalline carbide/amorphous carbon composites, Journal of Applied Physics 82 (1997) 855-858.
[68] R. Hauert, J. Patscheider. From alloying to nanocomposites—Improved performance of hard coatings, Advanced Engineering Materials 2 (2000) 247-259.
[69] U. Helmersson, S. Todorova, S. Barnett, J.E. Sundgren, L.C. Markert, J. Greene. Growth of single-crystal TiN/VN strained-layer superlattices with extremely high mechanical hardness, Journal of Applied Physics 62 (1987) 481-484.
[70] F.-W. Bach, K. Möhwald, A. Laarmann, T. Wenz. Modern surface technology, John Wiley & Sons, 2006.
[71] F. Rovere, D. Music, S. Ershov, H.-G. Fuss, P.H. Mayrhofer, J.M. Schneider. Experimental and computational study on the phase stability of Al-containing cubic transition metal nitrides, Journal of Physics D: Applied Physics 43 (2010) 035302.
[72] P.H. Mayrhofer, A. Hörling, L. Karlsson, J. Sjölén, T. Larsson, C. Mitterer, L. Hultman. Self-organized nanostructures in the Ti-Al-N system, Applied Physics Letters 83 (2003) 2049-2051.
[73] P. Mayrhofer, D. Music, J. Schneider. Ab initio calculated binodal and spinodal of cubic $Ti_{1-x}Al_xN$, Applied Physics Letters 88 (2006) 071922.
[74] P. Mayrhofer, D. Music, J. Schneider. Influence of the Al distribution on the structure, elastic properties, and phase stability of supersaturated $Ti_{1-x}Al_xN$, J. Appl. Phys 100 (2006) 094906.

[75] R. Rachbauer, S. Massl, E. Stergar, D. Holec, D. Kiener, J. Keckes, J. Patscheider, M. Stiefel, H. Leitner, P. Mayrhofer. Decomposition pathways in age hardening of Ti-Al-N films, Journal of Applied Physics 110 (2011) 023515.
[76] D. Holec, F. Rovere, P.H. Mayrhofer, P.B. Barna. Pressure-dependent stability of cubic and wurtzite phases within the TiN–AlN and CrN–AlN systems, Scripta Materialia 62 (2010) 349-352.
[77] H. Euchner, P. Mayrhofer. Vacancy-dependent stability of cubic and wurtzite $Ti_{1-x}Al_xN$, Surface and Coatings Technology (2015).
[78] P. Hohenberg, W. Kohn. Inhomogeneous electron gas, Physical review 136 (1964) B864.
[79] M. Born, R. Oppenheimer. Zur quantentheorie der molekeln, Annalen der Physik 389 (1927) 457-484.
[80] J. Emmerlich, D. Music, P. Eklund, O. Wilhelmsson, U. Jansson, J.M. Schneider, H. Högberg, L. Hultman. Thermal stability of Ti_3SiC_2 thin films, Acta Materialia 55 (2007) 1479-1488.
[81] T. Gebhardt, D. Music, D. Kossmann, M. Ekholm, I.A. Abrikosov, L. Vitos, J.M. Schneider. Elastic properties of fcc Fe–Mn–X (X= Al, Si) alloys studied by theory and experiment, Acta Materialia 59 (2011) 3145-3155.
[82] P. Mayrhofer, D. Music, T. Reeswinkel, H.-G. Fuß, J. Schneider. Structure, elastic properties and phase stability of $Cr_{1-x}Al_xN$, Acta Materialia 56 (2008) 2469-2475.
[83] P.H. Mayrhofer, F.D. Fischer, H.J. Böhm, C. Mitterer, J.M. Schneider. Energetic balance and kinetics for the decomposition of supersaturated $Ti_{1-x}Al_xN$, Acta materialia 55 (2007) 1441-1446.
[84] F. Rovere, D. Music, J. Schneider, P. Mayrhofer. Experimental and computational study on the effect of yttrium on the phase stability of sputtered Cr–Al–Y–N hard coatings, Acta Materialia 58 (2010) 2708-2715.
[85] J. Svoboda, F. Fischer, P. Mayrhofer. A model for evolution of shape changing precipitates in multicomponent systems, Acta Materialia 56 (2008) 4896-4904.
[86] K. Momma, F. Izumi. VESTA 3 for three-dimensional visualization of crystal, volumetric and morphology data, Journal of Applied Crystallography 44 (2011) 1272-1276.
[87] Royal Society of Chemistry, http://www.rsc.org/ (accessed on 22.01.2016).
[88] P. Mayrhofer, F. Rachbauer, D. Holec, F. Rovere, J. Schneider. Protective Transition Metal Nitride Coatings. Comprehensive Materials Processing, vol. 4. Elsevier Amsterdam, 2014. pp. 355-388.
[89] A. Reiter, V. Derflinger, B. Hanselmann, T. Bachmann, B. Sartory. Investigation of the properties of $Al_{1-x}Cr_xN$ coatings prepared by cathodic arc evaporation, Surface and Coatings Technology 200 (2005) 2114-2122.
[90] H. Hazar. Characterization of MoN coatings for pistons in a diesel engine, Materials & Design 31 (2010) 624-627.
[91] V. Miikkulainen, M. Suvanto, T.A. Pakkanen, S. Siitonen, P. Karvinen, M. Kuittinen, H. Kisonen. Thin films of MoN, WN, and perfluorinated silane deposited from dimethylamido precursors as contamination resistant coatings on micro-injection mold inserts, Surface and Coatings Technology 202 (2008) 5103-5109.
[92] A.Y. Ganin, L. Kienle, G.V. Vajenine. Synthesis and characterisation of hexagonal molybdenum nitrides, Journal of Solid State Chemistry 179 (2006) 2339-2348.
[93] E. Zhao, J. Wang, Z. Wu. Displacive phase transition, structural stability, and mechanical properties of the ultra-incompressible and hard MoN by first principles, physica status solidi (b) 247 (2010) 1207-1213.
[94] X. Zhao, K.-J. Range. High pressure synthesis of molybdenum nitride MoN, Journal of alloys and compounds 296 (2000) 72-74.
[95] S. Wang, D. Antonio, X. Yu, J. Zhang, A.L. Cornelius, D. He, Y. Zhao. The Hardest Superconducting Metal Nitride, Scientific reports 5 (2015).
[96] M. Kazmanli, M. Ürgen, A. Cakir. Effect of nitrogen pressure, bias voltage and substrate temperature on the phase structure of Mo–N coatings produced by cathodic arc PVD, Surface and Coatings Technology 167 (2003) 77-82.
[97] H. Ihara, Y. Kimura, K. Senzaki, H. Kezuka, M. Hirabayashi. Electronic structures of B1 MoN, fcc-Mo_2N, and hexagonal MoN, Physical Review B 31 (1985) 3177.

[98] K. Inumaru, K. Baba, S. Yamanaka. Synthesis and Characterization of Superconducting β-Mo_2N Crystalline Phase on a Si Substrate: An Application of Pulsed Laser Deposition to Nitride Chemistry, Chemistry of materials 17 (2005) 5935-5940.
[99] V. Anitha, S. Major, D. Chandrashekharam, M. Bhatnagar. Deposition of molybdenum nitride thin films by rf reactive magnetron sputtering, Surface and Coatings Technology 79 (1996) 50-54.
[100] M. Ürgen, O. Eryilmaz, A. Cakir, E. Kayali, B. Nilüfer, Y. Işik. Characterization of molybdenum nitride coatings produced by arc-PVD technique, Surface and Coatings Technology 94 (1997) 501-506.
[101] T. Suszko, W. Gulbiński, J. Jagielski. The role of surface oxidation in friction processes on molybdenum nitride thin films, Surface and Coatings Technology 194 (2005) 319-324.
[102] P. Ettmayer. Das System Molybdän-Stickstoff, Monatshefte für Chemie/Chemical Monthly 101 (1970) 127-140.
[103] H. Jehn, P. Ettmayer. The molybdenum-nitrogen phase diagram, Journal of the Less Common Metals 58 (1978) 85-98.
[104] N.V. Troitskaya, Z.G. Pinsker. Sov. Phys. Crystallogr. (Engl. Transl.) 4 (1960) 33-36.
[105] G. Linker, H. Schmidt, C. Politis, R. Smithey, P. Ziemann. Magnetic susceptibility and defect structure of B1 phase MoN sputtered films, Journal of Physics F: Metal Physics 16 (1986) 2167.
[106] Z. Liu, X. Zhou, D. Gall, S. Khare. First-principles investigation of the structural, mechanical and electronic properties of the NbO-structured 3d, 4d and 5d transition metal nitrides, Computational Materials Science 84 (2014) 365-373.
[107] Y. Wang, T. Yao, H. Li, J. Lian, J. Li, Z. Li, J. Zhang, H. Gou. Structural stability, phase transition, and mechanical and electronic properties of transition metal nitrides MN (M= Tc, Re, Os, and Ir): First-principles calculations, Computational Materials Science 56 (2012) 116-121.
[108] W. Pickett, B. Klein, D. Papaconstantopoulos. Theoretical prediction of MoN as a high T c superconductor, Physica B+ C 107 (1981) 667-668.
[109] J. Chen, L. Boyer, H. Krakauer, M. Mehl. Elastic constants of NbC and MoN: Instability of B 1-MoN, Physical Review B 37 (1988) 3295.
[110] G.L. Hart, B.M. Klein. Phonon and elastic instabilities in MoC and MoN, Physical Review B 61 (2000) 3151.
[111] A. Perry, A. Baouchi, J. Petersen, S. Pozder. Crystal structure of molybdenum nitride films made by reactive cathodic arc evaporation, Surface and Coatings Technology 54 (1992) 261-265.
[112] M. Maoujoud, L. Binst, P. Delcambe, M. Offergeld-Jardinier, F. Bouillon. Deposition parameter effects on the composition and the crystalline state of reactively sputtered molybdenum nitride, Surface and Coatings Technology 52 (1992) 179-185.
[113] N. Solak, F. Ustel, M. Urgen, S. Aydin, A. Cakir. Oxidation behavior of molybdenum nitride coatings, Surface and Coatings Technology 174 (2003) 713-719.
[114] H. Era, Y. Ide, A. Nino, K. Kishitake. TEM study on chromium nitride coatings deposited by reactive sputter method, Surface and Coatings Technology 194 (2005) 265-270.
[115] L. Zhou, F. Körmann, D. Holec, M. Bartosik, B. Grabowski, J. Neugebauer, P.H. Mayrhofer. Structural stability and thermodynamics of CrN magnetic phases from ab initio calculations and experiment, Phys. Rev. B. 90 (2014) 184102
[116] V. Ivanchenko, T. Melnichenko. Phase Equilibria and Alloy Thermodynamics in the System Chromium--Nitrogen, Metallofizika(Ukraine) 13 (1991) 23-30.
[117] P.H. Mayrhofer, G. Tischler, C. Mitterer. Microstructure and mechanical/thermal properties of Cr–N coatings deposited by reactive unbalanced magnetron sputtering, Surface and Coatings Technology 142 (2001) 78-84.
[118] P.H. Mayrhofer, F. Rovere, M. Moser, C. Strondl, R. Tietema. Thermally induced transitions of CrN thin films, Scripta Materialia 57 (2007) 249-252.
[119] W. Ernst, J. Neidhardt, H. Willmann, B. Sartory, P. Mayrhofer, C. Mitterer. Thermal decomposition routes of CrN hard coatings synthesized by reactive arc evaporation and magnetron sputtering, Thin Solid Films 517 (2008) 568-574.
[120] P.H. Mayrhofer, H. Willmann, C. Mitterer. Oxidation kinetics of sputtered Cr–N hard coatings, Surface and Coatings Technology 146 (2001) 222-228.

[121] I. Petrov, E. Mojab, R.C. Powell, J.E. Greene, L. Hultman, J.E. Sundgren. Synthesis of metastable epitaxial zinc-blende-structure AlN by solid-state reaction, Applied Physics Letters 60 (1992) 2491.
[122] I. Ivanov, L. Hultman, K. Järrendahl, P. Mårtensson, J.E. Sundgren, B. Hjörvarsson, J.E. Greene. Growth of epitaxial AlN(0001) on Si(111) by reactive magnetron sputter deposition, Journal of Applied Physics 78 (1995) 5721.
[123] A. Madan, I.W. Kim, S.C. Cheng, P. Yashar, V.P. Dravid, S.A. Barnett. Stabilization of Cubic AlN in Epitaxial AlN/TiN Superlattices, Physical Review Letters 78 (1996) 1743-1746.
[124] M. Setoyama, A. Nakayama, M. Tanaka, N. Kitagawa, T. Nomura. Formation of cubic-AlN in TiN/AlN superlattice, Surface and Coatings Technology 86-87 (1996) 225-230.
[125] M. Ueno, A. Onodera, O. Shimomura, K. Takemura. X-ray observation of the structural phase transition of aluminum nitride under high pressure, Physical Review B 45 (1992) 10123-10126.
[126] G. Li, J. Lao, J. Tian, Z. Han, M. Gu. Coherent growth and mechanical properties of AlN/VN multilayers, Journal of Applied Physics 95 (2004) 92.
[127] M.-S. Wong, G.-Y. Hsiao, S.-Y. Yang. Preparation and characterization of AlN/ZrN and AlN/TiN nanolaminate coatings, Surface and Coatings Technology 133-134 (2000) 160-165.
[128] D.-G. Kim, T.-Y. Seongb, Y.-J. Baik. Effects of annealing on the microstructures and mechanical properties of TiN/AlN nano-multilayer films prepared by ion-beam assisted deposition, Surface and Coatings Technology 153 (2002) 79-83.
[129] F.H. Mei, N. Shao, J.W. Dai, G.Y. Li. Coherent growth and superhardness effect of AlN/TiN nanomultilayers, Materials Letters 58 (2004) 3477-3480.
[130] W. Wong-Ng, H.F. McMurdie, B. Paretzkin, Y. Zhang, K.L. Davis, C.R. Hubbard, A.L. Dragoo, J.M. Stewart. Standard X-ray diffraction powder patterns of sixteen ceramic phases, Powder Diffraction 2 (1987) 191-202.
[131] H. Vollstädt, E. Ito, M. Akaishi, S.-i. Akimoto, O. Fukunaga. High pressure synthesis of rocksalt type of AlN, Proceedings of the Japan Academy. Ser. B: Physical and Biological Sciences 66 (1990) 7-9.
[132] R. Pandey, A. Sutjianto, M. Seel, J.E. Jaffe. Electronic structure of high pressure phase of AlN, Journal of materials research 8 (1993) 1922-1927.
[133] N.E. Christensen, I. Gorczyca. Calculated structural phase transitions of aluminum nitride under pressure, Physical Review B 47 (1993) 4307-4314.
[134] Q. Xia, H. Xia, A.L. Ruoff. Pressure-induced rocksalt phase of aluminum nitride: A metastable structure at ambient condition, Journal of Applied Physics 73 (1993) 8198.
[135] X.-Z. Ding, X.T. Zeng. Structural, mechanical and tribological properties of CrAlN coatings deposited by reactive unbalanced magnetron sputtering, Surface and Coatings Technology 200 (2005) 1372-1376.
[136] O. Knotek, F. Löffler, S. H.-J. Properties of arc-evaporated CrN and (Cr, Al)N coatings, Surface and Coatings Technology 45 (1991) 53-58.
[137] P.H. Mayrhofer, D. Music, T. Reeswinkel, H.G. Fuß, J.M. Schneider. Structure, elastic properties and phase stability of $Cr_{1-x}Al_xN$, Acta Materialia 56 (2008) 2469-2475.
[138] P.H. Mayrhofer, H. Willmann, L. Hultman, C. Mitterer. Influence of different atmospheres on the thermal decomposition of Al-Cr-N coatings, Journal of Physics D: Applied Physics 41 (2008) 155316.
[139] K. Frisk. A thermodynamic evaluation of the Cr-N, Fe-N, Mo-N and Cr-Mo-N systems, Calphad 15 (1991) 79-106.
[140] L. Zhou, F. Klimashin, D. Holec, P.H. Mayrhofer. Structural and mechanical properties of nitrogen-deficient cubic Cr-Mo-N and Cr-WN systems, arXiv preprint arXiv:1507.02738 (2015).
[141] Y. Benlatreche, C. Nouveau, I. Rahil, R. Marchal, L. Chekour. Comparative Studies on Mo–Cr–N and Al–Cr–N Coatings Obtained by PVD Dual Magnetron Sputtering, Plasma Processes and Polymers 6 (2009) 135-140.
[142] E.Y. Choi, M.C. Kang, D.H. Kwon, D.W. Shin, K.H. Kim. Comparative studies on microstructure and mechanical properties of CrN, Cr–C–N and Cr–Mo–N coatings, Journal of materials processing technology 187 (2007) 566-570.
[143] B. Gu, J. Tu, X. Zheng, Y. Yang, S. Peng. Comparison in mechanical and tribological properties of Cr–W–N and Cr–Mo–N multilayer films deposited by DC reactive magnetron sputtering, Surface and Coatings Technology 202 (2008) 2189-2193.

[144] K. Ho Kim, E. Young Choi, S. Gyun Hong, B. Gyu Park, J. Hong Yoon, J. Hae Yong. Syntheses and mechanical properties of Cr–Mo–N coatings by a hybrid coating system, Surface and Coatings Technology 201 (2006) 4068-4072.
[145] Y.L. Di, Z.H. Cai, P. Zhang, W. Shen. Research on CrN-based Ternary Films Deposited by magnetron sputtering, Advanced Materials Research 557 (2012) 1650-1653.
[146] P. Hones, R. Sanjinés, F. Lévy, O. Shojaei. Electronic structure and mechanical properties of resistant coatings: The chromium molybdenum nitride system, Journal of Vacuum Science & Technology A 17 (1999) 1024-1030.
[147] F. Lévy, P. Hones, P. Schmid, R. Sanjinés, M. Diserens, C. Wiemer. Electronic states and mechanical properties in transition metal nitrides, Surface and Coatings Technology 120 (1999) 284-290.
[148] P. Hones, R. Sanjinés, F. Lévy. Sputter deposited chromium nitride based ternary compounds for hard coatings, Thin Solid Films 332 (1998) 240-246.
[149] L. Vegard. Bildung von Mischkristallen durch Berührung fester Phasen, Zeitschrift für Physik A Hadrons and Nuclei 5 (1921) 393-395.
[150] J. Yang, Z. Yuan, Q. Liu, X. Wang, Q. Fang. Characterization of Mo–Al–N nanocrystalline films synthesized by reactive magnetron sputtering, Materials Research Bulletin 44 (2009) 86-90.
[151] J. Šůna, J. Musil, P. Dohnal. Control of macrostress σ in reactively sputtered Mo–Al–N films by total gas pressure, Vacuum 80 (2006) 588-592.
[152] S. Holly. Synthesis and characterization of AlCrMoN coatings. Physical Metallurgy and Materials Testing: University of Leoben, 2006. p.85.
[153] J.L. Endrino, V. Derflinger. The influence of alloying elements on the phase stability and mechanical properties of AlCrN coatings, Surface and Coatings Technology 200 (2005) 988-992.
[154] C.S. Yoon, K.H. Kim, S.H. Kwon, I.W. Park. Syntheses and Properties of Cr–Al–Mo–N Coatings Fabricated by Using a Hybrid Coating System, Journal of Korean Physical Society 54 (2009) 1237.
[155] G. Greczynski, S. Mráz, L. Hultman, J. Schneider. Venting temperature determines surface chemistry of magnetron sputtered TiN films, Applied Physics Letters 108 (2016) 041603.
[156] Я.С. Уманский, Ю.А. Скаков, А.Н. Иванов, Л.Н. Расторгуев. Кристаллография, рентгенография и электронная микроскопия: Учебник для вузов, Металлургия, 1982.
[157] V. Holý, U. Pietsch, T. Baumbach. High-resolution X-ray scattering from thin films and multilayers, Springer Tracts in Modern Physics 149 (1999).
[158] D. Rafaja, C. Wüstefeld, C. Baehtz, V. Klemm, M. Dopita, M. Motylenko, C. Michotte, M. Kathrein. Effect of internal interfaces on hardness and thermal stability of nanocrystalline $Ti_{0.5}Al_{0.5}N$ coatings, Metallurgical and Materials Transactions A 42 (2011) 559-569.
[159] K. Li, P. Yang, D. Xue. Anisotropic hardness prediction of crystalline hard materials from the electronegativity, Acta Materialia 60 (2012) 35-42.
[160] H. Bückle. Mikrohärteprüfung und ihre Anwendung, Berliner Union, 1965.
[161] M.G. Veprek-Heijman, S. Veprek. The deformation of the substrate during indentation into superhard coatings: Bückle's rule revised, Surface and Coatings Technology 284 (2015) 206-214.
[162] W.C. Oliver, G.M. Pharr. An improved technique for determining hardness and elastic modulus using load and displacement sensing indentation experiments, Journal of materials research 7 (1992) 1564-1583.
[163] D. Rafaja, C. Wüstefeld, M. Motylenko, C. Schimpf, T. Barsukova, M.R. Schwarz, E. Kroke. Interface phenomena in (super) hard nitride nanocomposites: from coatings to bulk materials, Chemical Society Reviews 41 (2012) 5081-5101.
[164] A.C. Fischer-Cripps. Critical review of analysis and interpretation of nanoindentation test data, Surface and Coatings Technology 200 (2006) 4153-4165.
[165] W.C. Oliver, G.M. Pharr. Improved technique for determining hardness and elastic modulus using load and displacement sensing indentation experiments, J. Mater. Res. 7 (1992) 1564-1580.
[166] A.C. Fischer-Cripps. Nanoindentation, Springer, 2011.
[167] D.-H. Chung. Elastic moduli of single crystal and polycrystalline MgO, Philosophical Magazine 8 (1963) 833-841.

[168] C. Brookes, J. O'neill, B. Redfern. Anisotropy in the hardness of single crystals. Proceedings of the Royal Society of London A: Mathematical, Physical and Engineering Sciences, vol. 322: The Royal Society, 1971. p.73-88.
[169] F.F. Klimashin, N. Koutná, H. Euchner, D. Holec, P.H. Mayrhofer. Computational and experimental studies on Mo–N hard coatings (manuscript in final preparation).
[170] F.F. Klimashin, H. Riedl, D. Primetzhofer, J. Paulitsch, P.H. Mayrhofer. Composition driven phase evolution and mechanical properties of Mo–Cr–N hard coatings, Journal of Applied Physics 118 (2015) 025305.
[171] F.F. Klimashin, H. Euchner, P.H. Mayrhofer. Computational and experimental studies on structure and mechanical properties of Mo–Al–N, Acta Materialia 107 (2016) 273-278.
[172] F.F. Klimashin, P.H. Mayrhofer. Synthesis of the super-hard Mo–Al–Cr–N coatings: ab initio-guided empirical approach (manuscript in final preparation).
[173] F.F. Klimashin, N. Koutná, L. Lobmaier, D. Holec, P.H. Mayrhofer. Vacant positions in MONTAN: Vacancy-driven evolution of structure and mechanical properties of hard Mo–Ta–N (manuscript in final preparation).

5. Manuscripts

5.1. Computational and experimental studies on Mo–N hard coatings

Abstract

The current study presents computational and experimental investigations on the influence of nitrogen vacancies on structure and phase evolution and resulting mechanical properties of reactively sputtered MoN_x coatings. We show experimentally – guided by density functional theory – that besides the thermodynamically stable β-$MoN_{0.44}$ and δ_2-MoN, also the metastable γ-MoN_x can be formed, when a non-equilibrium synthesis technique is used. Varying the nitrogen chemical potential, the single-phased γ-MoN_x was observed in range of nitrogen concentrations 23 – 34 at.% (x = 0.30 – 0.53), extending, hence, the homogeneity range towards the strong substoichiometric compositions (Mo:N < 2:1). The single-phased cubic-structured coating with the highest nitrogen content – γ-$MoN_{0.53}$ (VEC ~8.6) – provides the highest hardness of ~33 GPa among all MoN_x coatings studied, highlighting the need for the γ-MoN_x with the Me:N-stoichiometry close to 2:1, when aiming for excellent mechanical properties.

Both, *ab initio* calculations and experiments, show that with further filling the nitrogen vacancies of γ-MoN_x, an ordered structure forms, leading to the development of the pseudo-cubic γ'-Mo_3N_2 phase. In excellent agreement with *ab initio* calculations, the experimentally obtained lattice parameter of this γ'-MoN_x phase is larger than that of γ-MoN_x, especially at low nitrogen contents, due to their ordered nitrogen vacancies, which themselves contradicts for the generation of vacancies at the metal sublattice.

Keywords

Mo–N, hard coatings, vacancies, phase-ordering, Mo_3N_2

I. Introduction

Molybdenum nitrides are fascinating materials, which – depending on their phase composition – can be designed for a variety of applications requiring tailor-made properties. Besides the fact that all known phases within the molybdenum nitride system are superconducting, they also exhibit other excellent properties. For example, the hexagonal-structured δ-MoN [1, 2] is known as the hardest superconducting metal nitride [3, 4] with the second highest critical temperature for superconductivity of T_c = 13.8 K among all metal nitrides [3, 5]. Another excellent example is Mo_2N (with T_c = 5-7 K [3, 5, 6]), because its high-temperature modification, cubic-structured γ-Mo_2N (*Pm-3m*), exhibits excellent mechanical and tribological properties [7, 8] and – as shown in our recent studies [9-11] – has enormous potentials for being used as wear-resistant coating. Interestingly, like most cubic-structured

transition metal nitrides, γ-Mo_2N crystalizes with the NaCl-type structure, yet with 50% randomly distributed vacancies on the N-sublattice [12]. However, the stoichiometric γ-Mo_2N (2:1 stoichiometry Me:N) is very sensitive to the nitrogen content, thus, its physical properties are strongly governed by the nitrogen partial pressure used during deposition. The allotropic modification of γ-Mo_2N, the low-temperature tetragonal-structured β-Mo_2N (*I4₁/amd*, T_c = 5.2 K [6]), with ordered nitrogen vacancies has been studied rarely [6, 13, 14].

The Mo–N phase diagram plotted by Jehn [13] is furthermore enriched by the ordering phase Mo_3N_2 (similar to many other phase diagrams of nonstoichiometric transition metal nitrides and carbons after discovering their ordering phases [15]). The ordering phase Mo_3N_2 (which we hereafter refer to as pseudo-cubic γ'-MoN_x, because it is based on the cubic-structured γ-MoN_x phase, but with ordered N-vacancies) is rarely studied and was first reported by Troitskaya *et al.* [16] and classified as a NaCl-type structure with partial occupation of both sublattices (*Pm-3m*).There are no reports currently on its mechanical properties in literature.

Finally, cubic ξ-MoN with 1:1 stoichiometry was found to be thermodynamically unstable [17, 18], though some studies report on its existance [5, 19]. The theoretically predicted low-energy structure for ξ-MoN is a vacancy-rich NbO-prototype (*Pm-3m*) [20], which can be thought of as NaCl-type structure with 25% vacancies on each sublattice [21]. Intriguingly, the ξ-MoN phase was predicted to have the highest superconducting temperature among all refractory carbides and nitrides T_c = 29.4 K [22].

Guided by computational predictions, we performed experimental investigations on the impact of nitrogen vacancies on the structure and phase evolution, and resulting mechanical properties of Mo–N coatings, by adjusting the nitrogen partial pressure during their deposition. Although we discuss all the above mentioned phases, the main focus of this work, however, lies on γ-Mo_2N, which is an ideal candidate for multifunctional nitrides crystallizing in the cubic structure – a necessary prerequisite for high stability and strength.

II. Computational and experimental details

A. Computational details

The calculations were performed using Density Functional Theory (DFT) as implemented in the Vienna Ab initio Simulation package (VASP) [23, 24] together with pseudopotentials employing the projector augmented plane wave method (PAW) [25] and the exchange correlation functional within generalized gradient approximation (GGA) as parameterized by Perdew, Burke, and Ernzerhof (PBE) [26]. Five different types of Mo–N crystal structures were considered in the present study: cubic γ-Mo_2N (*Fm-3m*, space group 225, NaCl prototype), ξ-MoN (*Pm-3m*, space group 221, NbO-prototype), tetragonal β-Mo_2N (*I4₁/amd*, space group 141), hexagonal δ_2-MoN (*P6₃/mmc*, space group 194, NiAs-prototype), and δ_1-MoN (*P-6m2*, space group 187, WC-prototype). The plane-wave cut-off energy was set to 700 eV, while the reciprocal space was sampled with gamma-centered Monkhorst-Pack meshes [27] equivalent to at least 25000 k-points · atoms. The total energy of all systems was converged to about 10^{-3}

eV/at. The previously published lattice constants for the non-defected stoichiometric structures were used to initiate all bulk studies, and were optimized by fitting the energy vs. volume curve with the Birch-Murnaghan equation of state [28]. Structure optimizations in defected systems were carried out by relaxing the cell shape and atomic positions at every fixed volume.

Cubic γ-MoN_x defected structures were modelled using 2x2x2 supercells (64 lattice sites). The disordered vacancies were distributed according to the special quasi-random structure (SQS) method [29]. Additionally, we also considered (partially) ordered defect configurations which we refer to as pseudo-cubic γ'-MoN_x phase. The partially ordered γ'-MoN_x structures were constructed from a conventional cubic B1 cell (8 atoms) containing one or two N-vacancies, and subsequently expanded to 2x2x2 supercells. To obtain partially ordered structures with different nitrogen content, we started from the above mentioned defected supercells, arbitrarily filling vacancy sites. Since γ'-MoN_x defected supercells are based on the B1 type structure, the same sampling of the Brillouin zone as for γ-MoN_x was used. To investigate low-defected hexagonal δ_2-MoN_x compositions, one to four vacancies were randomly introduced into a perfect 1x1x2 supercell with 32 lattice sites. Analogically, we considered 1, 2, 3 and 8 N-vacancies in a 48-atom ξ-MoN_x supercell, with the latter ones generated according to the SQS method. Defects in tetragonal β-Mo_2N (β-MoN_x) were assumed to form either as N-vacancies (1 vacancy in a supercell with 16, 24, or 48 lattice sites, respectively) or as interstitials randomly filling the unoccupied N-sites (1 to 5 interstitials). One N-vacancy in supercells with 16, 24 and 54 lattice sites was considered for the hexagonal δ_1-MoN. Finally, 6 and 8 vacancies on the N-sublattice, distributed according to the SQS method, were used to model the highly defected WC-type MoN_x structures.

The averaged lattice parameters, a, corresponding to (defected) cubic structures were calculated as:

$$a = \sqrt[3]{V_0}, \tag{1}$$

where V_0 is the equilibrium volume of conventional B1-NaCl type cell. Since the defected systems are modelled in 2x2x2 supercells, it follows that $V_0 = V/8$, where V is the volume of fully relaxed (defected) supercell. The relative chemical stability was measured by the energy of formation, E_f, [30]:

$$E_f = [E_{tot}(Mo_nN_m) - n\mu_{Mo} - m\mu_N]/(n+m), \tag{2}$$

where $E_{tot}(Mo_nN_m)$ is the total energy of the (defected) supercell containing n Mo- and m N-atoms. The chemical potentials of Mo and N (μ_{Mo} and μ_N) in MoN were conventionally set to the total energies of bcc-Mo, $\mu_{Mo}(bcc-Mo)$, and molecular N_2, $\mu_N(N_2)$, respectively. To discuss the impact of the deposition conditions, we have additionally calculated E_f as a function of the nitrogen chemical potential μ_N. This value is limited by:

$$\mu_N \leq \mu_N(N_2). \tag{3}$$

Similarly,

$$\mu_{Mo} \leq \mu_{Mo}(bcc - Mo). \quad (4)$$

Using

$$E_{tot}(\mathrm{MoN}) = \mu_{Mo} + \mu_N, \quad (5)$$

one obtains the lower limit for μ_N:

$$E_{tot}(\mathrm{MoN}) - \mu_{Mo}(bcc - Mo) \leq \mu_N \quad (6)$$

It is important to note, that the lower limit for μ_N, given by Eq. (6), depends on the specific phase we assume.

In practise, the chemical potential is related to the nitrogen partial pressure and temperature [31]. As suggested in a recent study of Caffrey *et al*. [32], we plot $\mu_N - \mu_N(N_2)$ ranging from -2 to 0 eV. Thus, all reasonable values of the nitrogen chemical potential (cf. Eq. (3), Eq. (6)) are included. The lower limit is conventionally termed as the N-poor conditions, while the upper limit corresponds to the so-called N-rich condition [31].

B. Experimental details

The Mo–N thin films were synthesised using a modified Leybold Heraeus Z400 magnetron sputtering system, in mixed Ar and N_2 (both gases with purity above 99.999 %) glow discharge. All depositions were prepared with an 0.4 A DC on the Mo-target (99.95 % purity, Ø75 mm) and floating potential at the substrates (~ -15 V). The constant substrate temperature of 450 ± 20 °C corresponds to the homologous temperature T/T_m of ~ 0.3 (transition zone T according to Thornton's zone model [33]), thus providing an increased ad-atom mobility and preventing the appearance of voided columnar boundaries. Prior to the deposition process, the chamber was evacuated to a high vacuum of $p_{base} \leq 5 \cdot 10^{-4}$ Pa. A constant total pressure, p_T, of 0.35 Pa was kept for all sputtering processes during deposition. The N_2-to-total pressure ratio, p_{N2}/p_T, was varied between 0.13 and 1.

Phase analysis was carried out by means of X-ray diffraction (XRD) in the Bragg-Brentano geometry, using monochromatic CuK_α radiation (λ = 1.5418 Å). In addition, selected area electron diffractometry (SAED), using a transmission electron microscope (TEM, U = 200 kV, spatial resolution ~0.14 nm), was applied. For evaluation of the stress-free lattice parameter, glancing angle XRD measurements with an angle of incidence γ = 2° were conducted, and subsequently the $sin^2\psi$ method [34] was applied. The film growth morphology and growth rate were investigated from fracture cross-sections using scanning electron microscope (SEM) and TEM. The elemental composition was estimated by means of energy dispersive X-ray spectroscopy (EDX), using Mo–N thin film standards that have been characterized by elastic recoil detection analyses [9, 35]. Nanoindentation tests were conducted using an ultra-micro indentation system (UMIS) – equipped with a Berkovich diamond tip – and applying loads in the range of 3 to 30 mN. The evaluation of the film-only indentation hardness, *H*, and modulus, *E*, from the load-displacement curves was carried out after Oliver and Pharr [36] as described in detail in Refs. [9] and [37].

III. Results

A. Computational results

Figure 1 illustrates the formation energy of MoN_x as a function of the nitrogen content, *x*, derived from our *ab initio* calculations (with the chemical potential, μ_N, corresponding to the total energy of N_2). In accordance with the equilibrium phase diagram suggested by Jehn [13], β-MoN_x appears to be the most stable phase in the vicinity of the 2:1 stoichiometry, while the hexagonal-structured δ_2-MoN evidences the lowest energy for the 1:1 stoichiometry. Although the cubic phases, γ-MoN_x and γ'-MoN_x, possess structures with the lowest energy for certain compositions in between, they lie above the quasi-binary β-$MoN_{0.44}$–δ-MoN tie line (indicated in Fig. 1 by a red line) and, thus, appear to be metastable. (In other words, in thermodynamic equilibrium, any MoN_x structure with a chemical composition between β-$MoN_{0.44}$ and δ-MoN will undergo the phase separation into energetically stable constitutes β-$MoN_{0.44}$ and δ-MoN). Nevertheless, physical vapour deposition (PVD) as a non-equilibrium technique allows for synthesis and investigation of such metastable structures, especially when taking into account the random (partially random) distribution of the N-vacancies in γ-MoN_x (which we refer to as γ'-MoN_x for an easier reading) and the associated configurational entropy, *S*, which lowers the Gibbs free energy, G, of material with the enthalpy *H* at elevated temperatures, *T*, as follows:

$$G = H - TS, \tag{7}$$

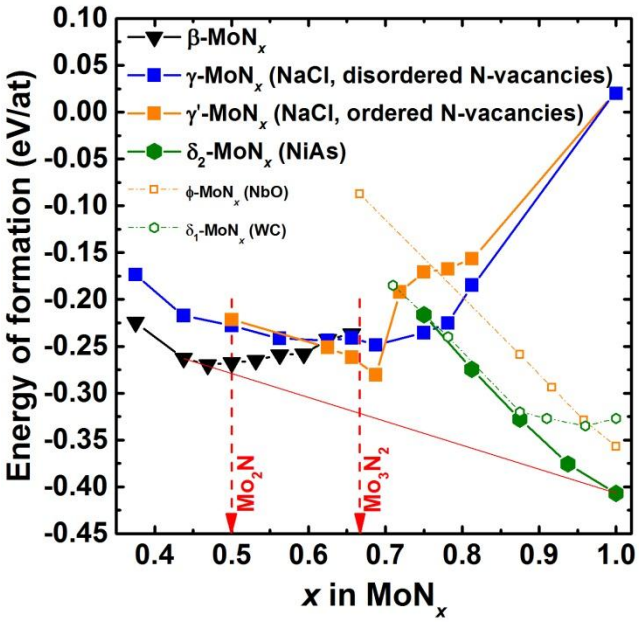

Fig. 1. *Ab initio* formation energies of four low-energy phases (β-MoN_x, γ-MoN_x, ϕ-MoN_x, δ_2-MoN_x – solid symbols) and the energetically inferior NbO-structured γ'-MoN_x and WC-structured δ_1-MoN_x (open smaller symbols) as a function of the nitrogen content *x* at normalized nitrogen chemical potential $\mu_N(N_2)$ = 0 [32, 38]. The red dashed lines indicate nitrogen content *x* of 2:1 and 3:2 stoichiometric compositions, the red solid line reveals the low-energy phases in the thermodynamic equilibrium.

The tetragonal-structured β-MoN_x appears to be the low-energy phase for $x < 0.6$, while for $x > 0.75$ the hexagonal-structured δ_2-MoN_x becomes energetically predominant (the δ_1/WC- and δ_2/NiAs-types show equal energies of formation up to $x \approx 0.85$, while lower nitrogen vacancy concentrations favour the δ_2/NiAs-type). Within the x range of $0.6 < x < 0.75$, both cubic phases, γ-MoN_x and γ'-MoN_x, exhibit the lowest formation energies. In fact, the closer the N-content approaches the 3:2 stoichiometry (i.e., $MoN_{0.67}$), the more energetically preferable becomes the pseudo-cubic γ'-MoN_x with (partially) ordered nitrogen vacancies with respect to γ-MoN_x, where the vacancies at the N-sublattice are randomly distributed . Interestingly, our calculations show that the structure of Mo_3N_2 – following the description proposed by Troitskaya *et al.* [16] (which can also be obtained from the NbO-structured ξ-MoN by increasing the N-vacancy concentration to ξ-$MoN_{0.67}$) – evidences E_f ≈ -0.09 eV/at (as compared to γ'-$MoN_{0.66}$ with E_f = -0.26 eV/at and γ'-$MoN_{0.69}$ with E_f = -0.28 eV/at). Therefore, γ'-MoN_x can be regarded as energetically preferred. The energetically closest structure to γ'-MoN_x, in the vicinity of x ≈ 0.67, is γ-MoN_x, having randomly distributed vacancies at the N-sublattice. The energy of formation of the 1:1 stoichiometric cubic structure becomes significantly more negative when vacancies are introduced on both sublattices. For instance, the comparison of γ-MoN (fully populated sublattices) having $E_f^{\gamma} \approx$ 0.02 eV/at with ξ-MoN (25% vacancies on each sublattice) having E_f^{ξ} ≈ -0.36 eV/at, would suggest the defect-rich structures to be preferred. However, this low-energy crystal structure of ξ-MoN is still by an amount of $\Delta E_f \approx$ 0.05 eV/at (at x = 1) less favourable than the thermodynamically stable defect-free δ_2-MoN. In addition, nearly the same values of ΔE_f can be observed for nitrogen-deficient compositions, ξ-MoN_x and δ_2-MoN_x.

The energy of formation is also strongly influenced by the chemical potential, μ_N, which can represent the specific deposition conditions, such as, for instance, the nitrogen partial pressure. By varying μ_N the stoichiometry can be altered and thereby various structures can be stabilized. The cubic phases, γ-MoN_x and γ'-MoN_x, remain, however, energetically inferior in the entire μ_N range investigated, from -2 to < 0 eV/at. Therefore, they are metastable even for the N-poor conditions (Fig. 2a). The hexagonal-structured δ-MoN_x is energetically preferred for the N-rich conditions, $-0.74 < \mu_N$ (eV/at) < 0, while N-poor conditions (lower values of μ_N) favor the formation of the substoichiometric β-MoN_x (with $x < 0.44$, see Fig. 2b). As non-equilibrium PVD techniques allows the synthesis of the metastable phases, we separately consider in Fig. 2c, cubic γ-MoN_x and pseudo-cubic γ'-MoN_x, which locally exhibit the lowest energy of formation in the x range of $0.6 < x < 0.75$ (Fig. 1). Cubic γ-MoN_x, with randomly distributed N-vacancies is the low-energy structure at N-poor conditions, μ_N < -0.61 eV/at, while for N-rich conditions the (partially) ordered pseudo-cubic γ'-MoN_x (x = 0.69) is energetically preferred. However, it is worth mentioning that the difference in formation energies of γ-MoN_x and γ'-MoN_x, for $\mu_N >$ -1.5 eV/at is lower than 50 meV/at, indicating almost equal formation probability and possible coexistence of both phases.

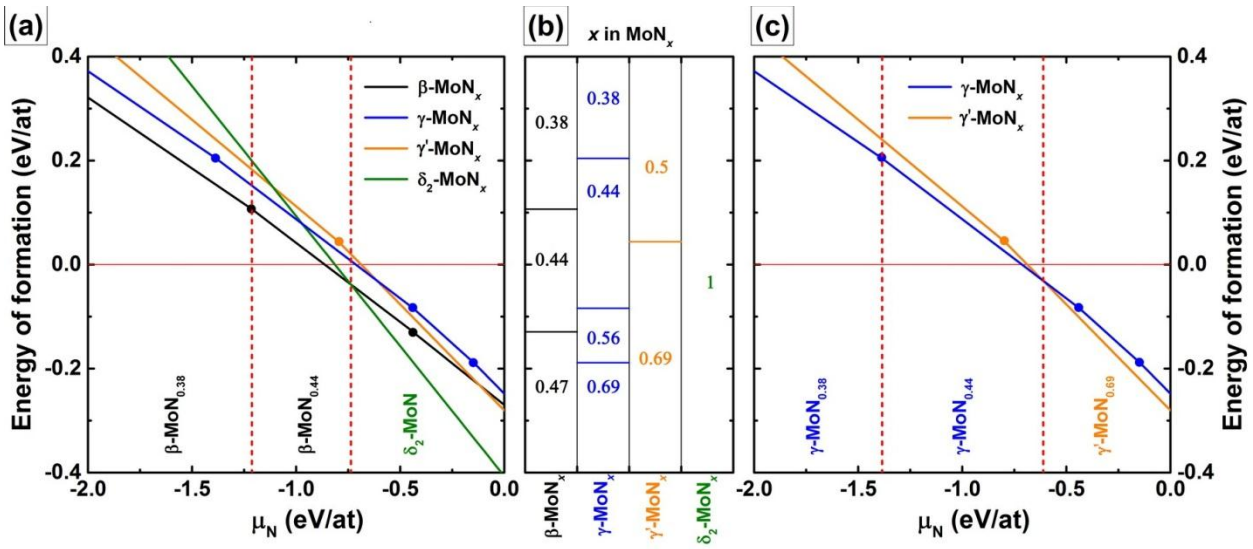

Fig. 2. *Ab initio* obtained phase formation energy with respect to the nitrogen chemical potential $\mu_N(N_2)$, ranging from -2 to 0 eV, thus, including all reasonable values. The solid lines depict the lowest formation energy of each phase (β-MoN_x, γ-MoN_x, γ'-MoN_x, δ_2-MoN_x) at a given chemical potential (a). At each kink (scatters on the lines), the stoichiometry of the low-energy phase changes (b). The metastable cubic phases are considered separately (c). The red solid line indicates the energy zero, the red dashed lines restrict the regions of low-energy phases color-noted in the bottom part of the graphs.

B. Experimental results

When increasing the nitrogen partial pressure used during deposition, p_{N2}/p_T, up to 0.26 the nitrogen content within our Mo–N coatings increases up to ~32 at.% (i.e. 2:1 stoichiometry, see the red dashed line in Fig. 3). However, a further increase of p_{N2}/p_T-ratio up to 0.69 only slightly increases the N-content up to ~40 at.% (corresponds to the 3:2 stoichiometry, see the red dashed line in Fig. 2) of our Mo–N thin films. Even when synthesised in a pure nitrogen atmosphere (p_{N2}/p_T = 1) the N-content is only increased to ~43 at.%.

XRD investigations, Fig. 4a, reveal that single-phased cubic γ-MoN_x forms in a p_{N2}/p_T-window between 0.20 and 0.32, corresponding to the range of N-solubility in γ-MoN_x of x = 0.30 – 0.53 (corresponding to 23 – 34 at.% N). For lower nitrogen partial pressures (p_{N2}/p_T = 0.13), β-Mo_2N forms together with bcc-Mo, while with increasing p_{N2}/p_T to 0.50, the pseudo-cubic γ'-MoN_x crystallizes next to γ-$MoN_{0.5}$. The low-intensity superstructure reflections from (100) and (220) planes of γ'-MoN_x are shifted to higher diffraction angles indicating tensile stresses. Even higher nitrogen partial pressures, p_{N2}/p_T = 0.69, lead to the formation of pseudo-cubic γ'-Mo_3N_2 with significantly more intense (100) and (300) superstructure reflections, which are shifted to lower diffraction angles. This indicates an increase of the long-range order parameter or even a completely ordered structure, consisting of single-phased γ'-Mo_3N_2 under compressive stresses. As mentioned above, this coating exhibits 40 at.% nitrogen, which corresponds exactly to the 3:2 stoichiometry of Mo_3N_2. When preparing our Mo–N coatings just in nitrogen atmosphere (p_{N2}/p_T = 1) also hexagonal h-MoN crystallizes next to polycrystalline γ'-Mo_3N_2.

This phase evolution with increasing p_{N2}/p_T-ratio used during deposition and especially the evolution of the superstructure reflections can clearly be observed using the color-coded XRD intensity map depicted in Fig. 4b. This figure is composed of the XRD patterns of nine different MoN_x coatings using a linear interpolation scheme between the experimental data.

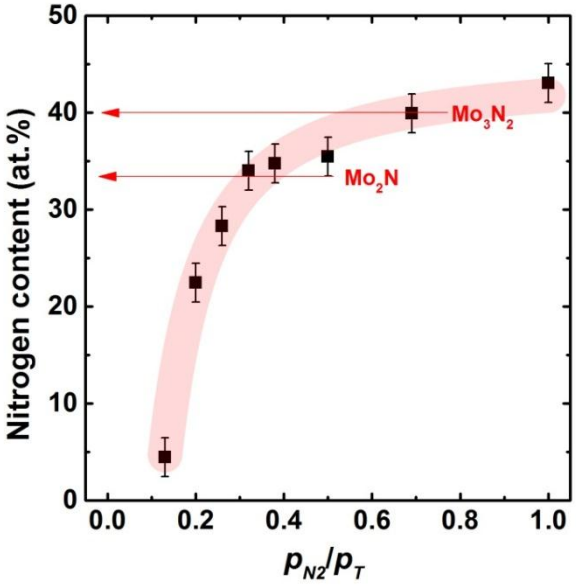

Fig. 3. EDX measurements of the nitrogen content as a function of the nitrogen partial pressure used during deposition. The red dashed lines indicate nitrogen content *x* of 2:1 and 3:2 stoichiometric compositions.

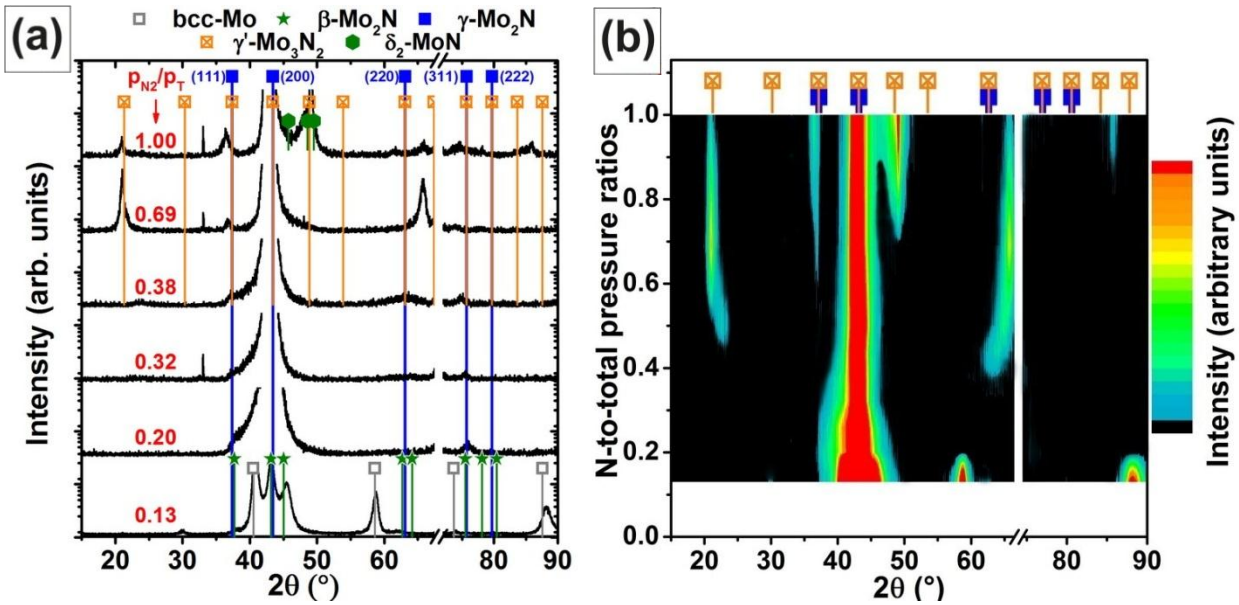

Fig. 4. Logarithmic scaled XRD patterns of significant MoN_x coatings (a) and color-coded XRD intensities of all MoN_x coatings (b) with indicated peak positions for bcc-Mo (ICDD 00-042-1120), β-Mo_2N (ICDD 00-025-1366), γ-Mo_2N (ICDD 00-025-1366), γ'-Mo_3N_2 (the XRD pattern of γ-Mo_2N including the forbidden reflexes), and δ_2-MoN_x (ICDD 01-072-9061).

The cross-sectional TEM investigations and corresponding SAED analyses — such as shown for $MoN_{0.66}$, Figs. 5a and d, and for $MoN_{0.53}$, Figs. 5c and d — reveal a columnar growth

microstructure and single-phased cubic-structure, respectively. Furthermore, the SAED patterns presented in Fig. 5b clearly indicate the formation of an ordered cubic structure for the $MoN_{0.67}$ coating prepared at p_{N2}/p_T = 0.69. In agreement with XRD, this corresponds to the formation of pseudo-cubic γ'-$MoN_{0.66}$ or γ'-Mo_3N_2.

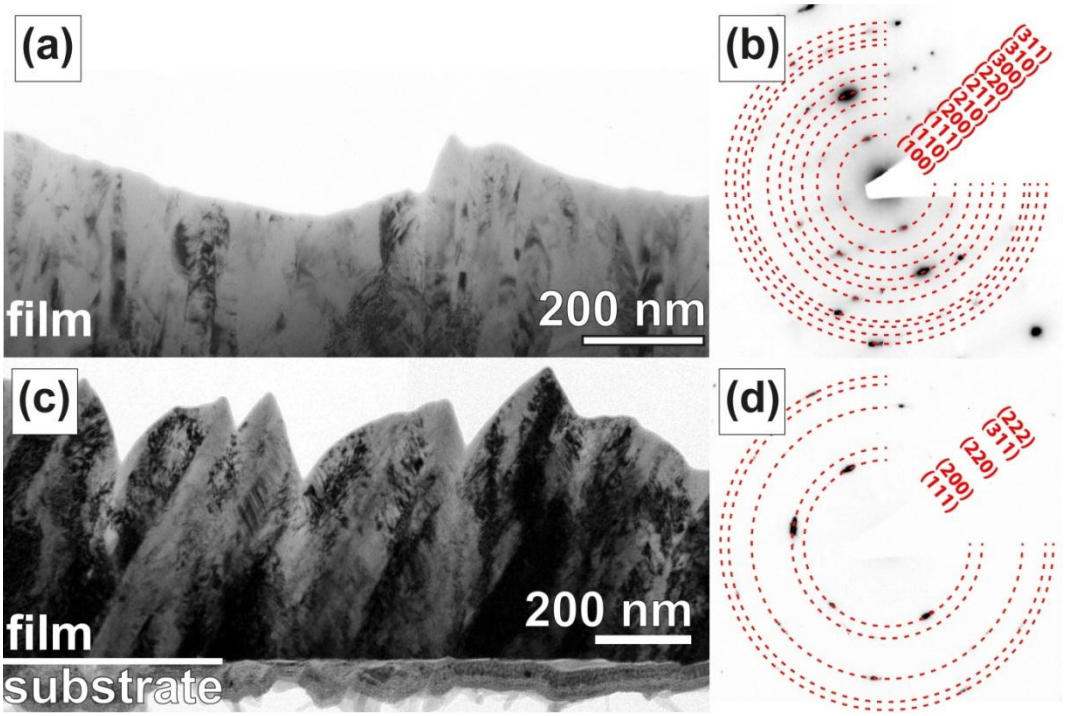

Fig. 5. TEM images and SAED patterns of the pseudocubic γ'-$MoN_{0.66}$ with partially ordered nitrogen vacancies (a, b) and cubic γ-$MoN_{0.53}$ with the randomly distributed nitrogen vacancies (c, d).

With increasing p_{N2}/p_T from 0.26 to 1 the lattice parameter continuously increases from 4.169 ± 0.022 Å (for single-phased γ-$MoN_{0.48}$, i.e. nitrogen content of 32 ± 2 at.%) to 4.256 ± 0.019 Å (determined for γ'-MoN_x, which, however, coexists with δ_2-MoN), see Fig. 6a. The calculated lattice parameters for γ'-MoN_x and γ-MoN_x were extracted from our *ab initio* data. For both cubic phases, the lattice parameter increases almost linearly with increasing nitrogen content, *x*, Fig. 6b. When the nitrogen content of the coatings, *x*, increases from 0.5 to 0.8, the lattice parameter of the pseudo-cubic γ'-MoN_x phase continuously increases from 4.211 to 4.348 Å, but that of γ-MoN_x only increases from 4.202 to 4.302 Å. Their very close values make a clear identification and separation just by their lattice parameters difficult. Our calculated lattice parameter for γ-$MoN_{0.5}$ is in excellent agreement with earlier reports [11]. When we consider the well-known and accepted overestimation of GGA for the lattice parameters [39], the stress-free lattice parameters of our single-phased cubic-structured coatings (γ-MoN_x: prepared at p_{N2}/p_T = 0.20 and 0.32; γ'-MoN_x prepared at p_{N2}/p_T = 0.69) yield an excellent agreement with *ab initio* calculations, see Fig. 6b. The coating prepared at p_{N2}/p_T = 0.69 contains 40 at.% N (hence a 3:2 Me:N-stoichiometry, i.e., Mo_3N_2), Fig. 3, and clearly exhibits pronounced superstructure reflexes during XRD and SAED investigations, see Figs. 4a and 5b, respectively. Thus, this coating can clearly be assigned as pseudo-cubic γ'-Mo_3N_2 having an ordered structure. Based on the excellent agreement between our *ab initio* calculated and

experimentally obtained lattice parameters (a_0 = 4.234 Å), we can conclude that our pseudo-cubic γ'-Mo_3N_2 phase forms across the γ-$MoN_{0.5}$ phase by filling the N-vacancies (as used for the *ab initio* calculations) rather than via generation of vacancies on the Mo-sublattice. The latter is reported by Troitskaya *et al.* (ICDD 03-065-4278) for Mo_3N_2, but they observed a lattice parameter of only a = 4.165 Å, as also indicated in the ICDD 03-065-4278 data base. Consequently, PVD allows for the preparation of the ordered pseudo-cubic γ'-Mo_3N_2 phase, which is actually based on the cubic-structured γ-$MoN_{0.5}$, but has partially ordered N-vacancies.

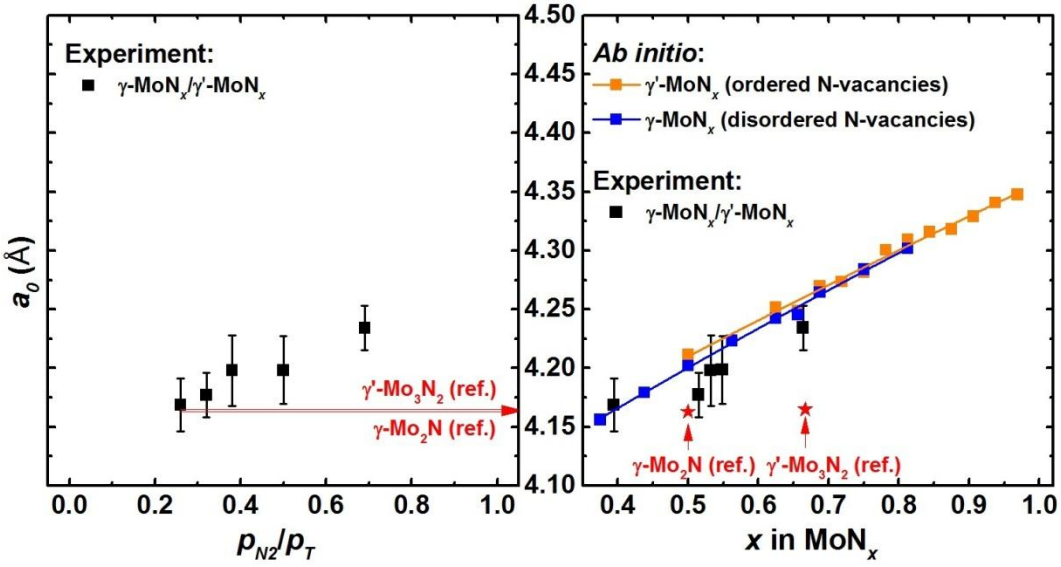

Fig. 6. Stress-free lattice parameters, a_0, of the single-phased cubic-structured coatings γ-MoN_x and γ-MoN_x as a function of the N-to-total pressure ratio (a) and as a function of x in MoN_x (b). The red lines (a) or stars (b) indicate the literature values for the lattice parameters of γ-Mo_2N (ICDD 00-025-1366) and γ'-Mo_3N_2 (ICDD 03-065-4278). The subfigure (b) contains the results of our *ab initio* calculations together with the experimental values.

In addition to these results, also the deposition rate (see Fig. 7) for our cubic-structured Mo–N coatings decreases nearly linearly from ~1.3 nm/s (single-phased γ-$MoN_{0.30}$ at p_{N2}/p_T = 0.20) to ~0.7 nm/s (single-phased γ'-$MoN_{0.67}$ at p_{N2}/p_T = 0.69) with increasing nitrogen partial pressure, suggesting no major changes in the crystal structure. All of our coatings exhibit a very dense fibrous growth morphology, see the examples presented in Figs. 8a to f, prepared at p_{N2}/p_T = 0.13 to 1, corresponding to the six coatings presented by XRD patterns in Fig. 4a.

The nanoindentation hardness, H, of our coatings increases from 26.7 ± 0.6 to 33.0 ± 1.7 GPa, with increasing p_{N2}/p_T from 0.13 to 0.32, but then decreases again to ~28-29 GPa with a further increase of p_{N2}/p_T, see Fig. 9a. The highest indentation hardness of all coatings studied (33.0 ± 1.7 GPa) is obtained for the single-phased cubic-structured γ-$MoN_{0.53}$. The single-phased pseudo-cubic γ'-$MoN_{0.67}$ coating, exhibits only 27 GPa. The indentation modulus, E, increases noticeable from ~390 to 410 GPa with increasing p_{N2}/p_T from 0.13 to 0.20, where the coatings do not contain metallic bcc-Mo anymore. Upon further increasing p_{N2}/p_T to 1, E increases slower, almost linearly to ~440 GPa. Also this nearly linear behaviour of the indentation modulus when increasing p_{N2}/p_T from 0.20 to 0.69, where we do observe by XRD and SAED a

change from γ-MoN_x to γ'-MoN_x, suggests no major change in crystal structure. Hence, supports our conclusion that the crystal structure of our $MoN_{0.67}$ coating (prepared with p_{N2}/p_T = 0.69) – exhibiting the superstructure reflexes during XRD and SAED investigations – is based on γ-MoN_x, but with partly filled and ordered N-vacancies. Finally, when plotting *H* and *E*-values of γ-MoN_x to γ'-MoN_x over the valence electron concentration (per unit cell), the maximum of hardness is found in the vicinity of ~8.4, while the *E*-moduli remain almost unaltered (cf. Fig. 9b).

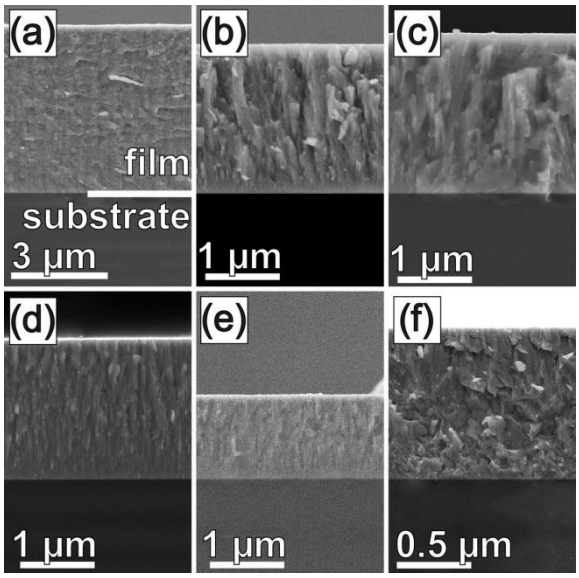

Fig. 7. SEM fracture cross-sections of significant MoN_x coatings with increasing p_{N2}/p_T from 0.13 (a) to 1 (f).

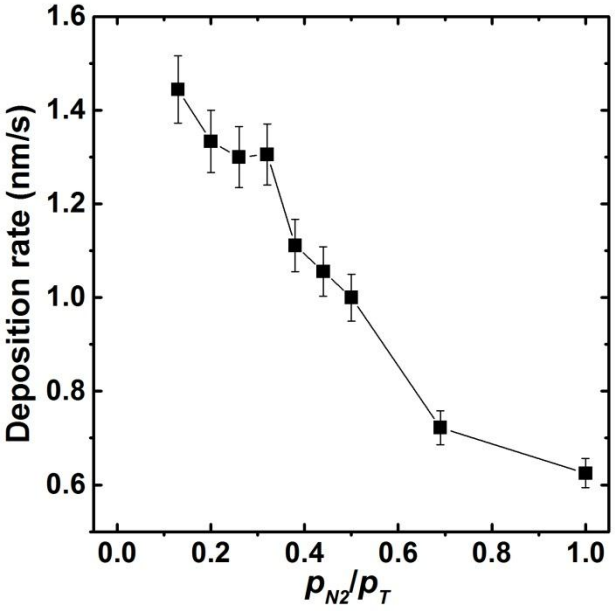

Fig. 8. Deposition rate of our MoN_x coatings as a function of the nitrogen partial pressure.

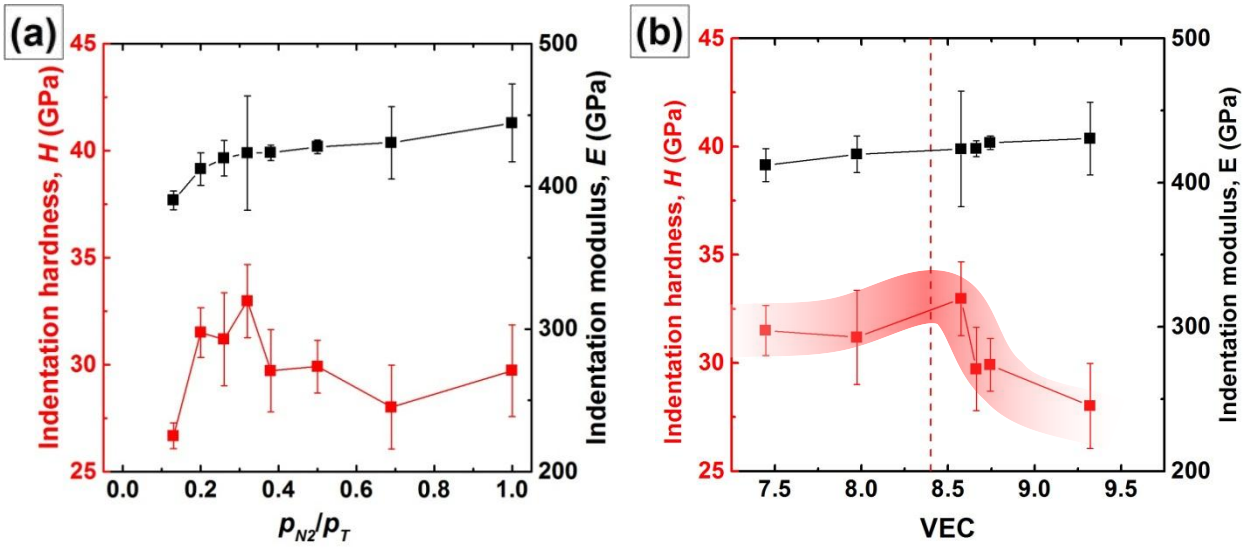

Fig. 9. Indentation hardness, *H*, (left axis, red open circles) and indentation modulus, *E*, (right axis, black solid squares) of our MoN_x coatings as a function of the nitrogen partial pressure used during deposition (a) and valence electron concentration (b).

IV. Discussion

The nitrogen content (or better, the concentration of N-vacancies, Fig. 1) and the chemical potential of nitrogen, μ_N, (Fig. 2) play the decisive role in the phase formation of MoN_x, whereby and even sub- and overstoichiometric compositions are enabled. For example, the tetragonal-structured β-MoN_x phase – which preferentially crystallize as substoichiometric nitride with x = 0.44 rather than with Me:N stoichiometry of 2:1 in thermodynamic equilibrium – prefers even higher substoichiomteries for decreased nitrogen chemical potentials, Fig. 2.

Our chemical investigations (Fig. 3) combined with structural investigations (XRD, Fig. 4, and SAED, Fig. 5b) reveal the formation of single-phased cubic-structured coatings based on the γ-Mo_2N phase only within a p_{N2}/p_T window 0.20 – 0.32 used during deposition. These coatings have nitrogen contents between 23 and 34 at.% (x = 0.30 – 0.53) and no superstructure reflexes can be detected. To highlight, that this cubic-structured γ-Mo_2N phase is actually based on the NaCl-type structure with half-filled N-sublattice, we again want to mention our chosen notification of γ-MoN_x.

The formation energy clearly highlights γ-MoN_x as metastable phase, Fig. 1. With respect to the more stable β-MoN_x phase at low N-contents, the N-vacancies are randomly distributed. Hence, the configurational entropy itself is not zero (contrary to ordered phases) suggesting the preferred formation of γ-MoN_x (over β-MoN_x) especially at elevated temperatures. Based on our *ab initio* calculations, we further envision that elevated temperatures combined with high cooling rates (as accessible by PVD processes) allow the formation of γ-MoN_x over a rather wide composition range. The other phases, β-MoN_x and γ'-MoN_x, are based on ordered N-vacancy structures and hence their formation, especially at higher temperatures, is not promoted over the γ-MoN_x. Even for the 0K calculations, the difference in energy of formation between γ-

MoN_x and β-MoN_x or γ'-MoN_x is below 50 meV/at, cf. Fig. 1. For N-contents, x, between 0.55 and 0.65, the difference is even below 10 meV/at. Especially, when using N-deficient conditions during deposition (simulated by *ab initio* calculations using low chemical potentials for nitrogen, μ_N < -1.5 eV/at) the formation of γ-MoN_x is preferred over the ordered γ'-MoN_x phase even at 0K. A shift of the chemical potential towards N-rich conditions increasingly favours the ordered γ'-MoN_x phase, cf. Fig. 2c. This behaviour is almost expected from the energy of formation, yielding lowest values for γ'-MoN_x at compositions around x = 0.67 (hence, Mo:N of 3:2 stoichiometry).

Our experiments are in excellent agreement with these calculations, because the MoN_x thin films prepared with $p_{N2}/p_T \geq 0.38$ exhibit superstructure reflexes during XRD (Fig. 4) and SAED (Fig. 5b) investigations, highlighting the formation of ordered structures. The coating prepared with $p_{N2}/p_T = 0.69$ provides the highest degree of ordering (please compare the superstructure reflexes in Fig. 4, which are most pronounced for this coating). The presence of this rarely investigated phase within the Mo–N system is proven by indexing the diffraction patterns based on the structure suggested by Troitskaya *et al.* [16] (as indicated in ICDD 03-065-4278). However, contrary to the description Troitskaya *et al.* [16], our γ'-MoN_x phase only contains vacancies at the N-sublattice. Actually, a corresponding model for our γ'-MoN_x phase (according to Maojoud *et al.* [40]) was already proposed earlier by Pinsker *et al.* [41]. The formation of superstructure reflexes can generally be attributed to the doubling of the distance between equivalent atomic planes. Since even small lattice distortions result in lowering of the crystal symmetry [42], the phase ordering will result in transition from the cubic to, for instance, orthorhombic structure. This significantly broadens the search field for a low-energy structure of the pseudo-cubic γ'-Mo_3N_2 phase.

Within all Mo–N coatings synthesized, the single-phased cubic-structured γ-$MoN_{0.53}$ exhibits the highest hardness of ~33 GPa. The altering elemental composition is accompanied by changes in the electronic band structure, which can be characterized by e.g. the number of the electrons in the valence band per unit cell [43, 44]. Despite the limitation for strongly substoichiometric compounds, altering the electronic structure [45], hardness enhancement with approaching VEC of 8.4 was observed for many B1-structured transition metal nitrides, e.g., the group V TMs, NbN_x and TaN_x [46]. An excellent correlation of VEC and shear modulus behaviours [45, 47] suggests the hardness improvement through population of the non-metal *p* and metal *d* orbitals – the shear-resistive bonding states [45, 47].

With the additional formation of the pseudo-cubic and ordered γ'-$MoN_{0.67}$ phase – upon further increasing p_{N2}/p_T during deposition – the hardness decreases. We envision that this ordered phase evolves within γ-MoN_x and forms coherent domains due to the small lattice mismatch of ~1.4% (assuming the <100> growth of γ-$MoN_{0.53}$ with 4.177 Å γ'-$MoN_{0.66}$ with 4.234 Å). Though formation of coherent domains is known to enhance the hardness due to induced coherency strains [48], we observe a pronounced hardness reduction. Again, the hardness deterioration can be explained in terms of VEC/shear modulus, i.e., due to population of the shear-sensitive metal–metal orbitals. The hardness slightly increases again when further

increasing p_{N2}/p_T to 1 during deposition, as additionally the hexagonal δ-MoN phase is formed, cf. Fig. 4, which is reported to be super-hard [3, 4].

Interestingly, the reported limitations for the empiric criterion VEC for the strongly substoichiometric compounds does not spread to the γ-MoN_x even though it consists to 50% of vacancies. This might imply that vacancies at the N-sublattice of γ-MoN_x have to be treated as structural vacancies (i.e., related directly to the chemical composition) [15], performing the same functions as the present nitrogen atoms, thus, forming together a substitutional solid solution at the N-sublattice.

V. Summary and conclusions

Based on our computational and experimental results, we can conclude, that the nitrogen content (actually the vacancies at the N-sublattice) plays a crucial role in the phase formation within the Mo–N system. Among the thermodynamically stable β-$MoN_{0.44}$ and δ_2-MoN phases, the metastable cubic γ-MoN_x, having the local minima of the formation energy for *x* between 0.6 – 0.75, can be obtained by PVD due to their conditions far from equilibrium. When approaching the Me:N stoichiometry of 3:2 ($x \approx 0.67$), the initially randomly distributed nitrogen vacancies favour their ordering, leading to the formation of the pseudo-cubic γ'-MoN_x phase. Contrary to earlier reports on Mo_3N_2, our γ'-$MoN_{0.67}$ phase (also with a 3:2 stoichiometry) contains vacancies only at the N-sublattice, hence being based on γ-MoN_x but with ordered N-vacancies.

Coatings prepared with p_{N2}/p_T ratios between 0.2 and 0.32 during deposition have nitrogen contents between 23 – 34 at.% (x = 0.30 – 0.53), respectively, and crystallize single-phased cubic γ-MoN_x structured (with random distribution of the N-vacancies). These also exhibit the highest hardnesses among all coatings studied, with a maximum of ~33 GPa for γ-$MoN_{0.53}$, being closest to the 2:1 stoichiometry and VEC of ~8.6. Higher p_{N2}/p_T-ratios during deposition favour the formation of the (partially) ordered γ'-$MoN_{0.67}$ phase, and with p_{N2}/p_T = 0.69, the coating contains the highest fraction of γ'-$MoN_{0.67}$. There, the stoichiometry is closest to 3:2, where also our *ab initio* calculations exhibit highest preference for this partially ordered structure, being based on γ-MoN_x. The close relation between γ'-$MoN_{0.67}$ and γ-MoN_x is represented by their very similar lattice parameters (for comparable N-contents) and smooth transition in indentation moduli, which only slightly increases from 420 for γ-$MoN_{0.53}$ to 430 for γ'-$MoN_{0.67}$. Again in excellent agreement with *ab initio* calculations, the coating with the highest N-content prepared of 43 at% (x = 0.75) is dual phase structured (with hardnesses of ~30 GPa) and contains also the δ_2-MoN phase.

ACKNOWLEDGEMENTS

The financial support by the START Program (Y371) of the Austrian Science Fund (FWF) is gratefully acknowledged. The authors are thankful to the XRC, USTEM, and VSC of the TU Wien.

REFERENCES

[1] A.Y. Ganin, L. Kienle, G.V. Vajenine. Synthesis and characterisation of hexagonal molybdenum nitrides, Journal of Solid State Chemistry 179 (2006) 2339-2348.

[2] E. Zhao, J. Wang, Z. Wu. Displacive phase transition, structural stability, and mechanical properties of the ultra-incompressible and hard MoN by first principles, physica status solidi (b) 247 (2010) 1207-1213.

[3] S. Wang, D. Antonio, X. Yu, J. Zhang, A.L. Cornelius, D. He, Y. Zhao. The Hardest Superconducting Metal Nitride, Scientific reports 5 (2015).

[4] M. Kazmanli, M. Ürgen, A. Cakir. Effect of nitrogen pressure, bias voltage and substrate temperature on the phase structure of Mo–N coatings produced by cathodic arc PVD, Surface and Coatings Technology 167 (2003) 77-82.

[5] H. Ihara, Y. Kimura, K. Senzaki, H. Kezuka, M. Hirabayashi. Electronic structures of B1 MoN, fcc Mo_2N, and hexagonal MoN, Physical Review B 31 (1985) 3177.

[6] K. Inumaru, K. Baba, S. Yamanaka. Synthesis and Characterization of Superconducting β-Mo_2N Crystalline Phase on a Si Substrate: An Application of Pulsed Laser Deposition to Nitride Chemistry, Chemistry of materials 17 (2005) 5935-5940.

[7] G. Gassner, P.H. Mayrhofer, K. Kutschej, C. Mitterer, M. Kathrein. Magnéli phase formation of PVD Mo–N and W–N coatings, Surface and Coatings Technology 201 (2006) 3335-3341.

[8] M. Ürgen, O. Eryilmaz, A. Cakir, E. Kayali, B. Nilüfer, Y. Işik. Characterization of molybdenum nitride coatings produced by arc-PVD technique, Surface and Coatings Technology 94 (1997) 501-506.

[9] F.F. Klimashin, H. Riedl, D. Primetzhofer, J. Paulitsch, P.H. Mayrhofer. Composition driven phase evolution and mechanical properties of Mo–Cr–N hard coatings, Journal of Applied Physics 118 (2015) 025305.

[10] F.F. Klimashin, H. Euchner, P.H. Mayrhofer. Computational and experimental studies on structure and mechanical properties of Mo-Al-N, Acta Materialia (2016).

[11] L. Zhou, F. Klimashin, D. Holec, P.H. Mayrhofer. Structural and mechanical properties of nitrogen-deficient cubic Cr-Mo-N and Cr-W-N systems, arXiv preprint arXiv:1507.02738 (2015).

[12] P. Ettmayer. Das System Molybdän-Stickstoff, Monatshefte für Chemie/Chemical Monthly 101 (1970) 127-140.

[13] H. Jehn, P. Ettmayer. The molybdenum-nitrogen phase diagram, Journal of the Less Common Metals 58 (1978) 85-98.

[14] M. Mudholkar, L. Thompson. Control of composition and structure for molybdenum nitride films synthesized using ion beam assisted deposition, Journal of applied physics 77 (1995) 5138-5143.

[15] A.I. Gusev, A.A. Rempel, A.J. Magerl. Disorder and order in strongly nonstoichiometric compounds: transition metal carbides, nitrides and oxides, Springer Science & Business Media, 2013.

[16] N.V. Troitskaya, Z.G. Pinsker. Sov. Phys. Crystallogr. (Engl. Transl.) 4 (1960) 33-36.

[17] J. Chen, L. Boyer, H. Krakauer, M. Mehl. Elastic constants of NbC and MoN: Instability of B 1-MoN, Physical Review B 37 (1988) 3295.

[18] G.L. Hart, B.M. Klein. Phonon and elastic instabilities in MoC and MoN, Physical Review B 61 (2000) 3151.

[19] E. Donovan, G. Hubler, M. Mudholkar, L.T. Thompson. Ion-beam-assisted deposition of molybdenum nitride films, Surface and Coatings Technology 66 (1994) 499-504.

[20] Z. Liu, X. Zhou, D. Gall, S. Khare. First-principles investigation of the structural, mechanical and electronic properties of the NbO-structured 3d, 4d and 5d transition metal nitrides, Computational Materials Science 84 (2014) 365-373.

[21] G. Linker, H. Schmidt, C. Politis, R. Smithey, P. Ziemann. Magnetic susceptibility and defect structure of B1 phase MoN sputtered films, Journal of Physics F: Metal Physics 16 (1986) 2167.

[22] W. Pickett, B. Klein, D. Papaconstantopoulos. Theoretical prediction of MoN as a high T_c superconductor, Physica B+ C 107 (1981) 667-668.

[23] G. Kresse, J. Furthmüller. Efficient iterative schemes for ab initio total-energy calculations using a plane-wave basis set, Physical Review B 54 (1996) 11169.

[24] G. Kresse, J. Hafner. Ab initio molecular dynamics for liquid metals, Physical Review B 47 (1993) 558.
[25] G. Kresse, D. Joubert. From ultrasoft pseudopotentials to the projector augmented-wave method, Physical Review B 59 (1999) 1758.
[26] J.P. Perdew, K. Burke, M. Ernzerhof. Generalized gradient approximation made simple, Physical review letters 77 (1996) 3865.
[27] H.J. Monkhorst, J.D. Pack. Special points for Brillouin-zone integrations, Physical Review B 13 (1976) 5188.
[28] F. Birch. Finite elastic strain of cubic crystals, Physical Review 71 (1947) 809.
[29] S.-H. Wei, L. Ferreira, J.E. Bernard, A. Zunger. Electronic properties of random alloys: Special quasirandom structures, Physical Review B 42 (1990) 9622.
[30] H. Euchner, P. Mayrhofer. Vacancy-dependent stability of cubic and wurtzite $Ti_{1-x}Al_xN$, Surface and Coatings Technology (2015).
[31] C. Stampfl, A. Freeman. Metallic to insulating nature of TaN x: role of Ta and N vacancies, Physical Review B 67 (2003) 064108.
[32] N.M. Caffrey, R. Armiento, R. Yakimova, I.A. Abrikosov. Charge neutrality in epitaxial graphene on 6 H-SiC (0001) via nitrogen intercalation, Physical Review B 92 (2015) 081409.
[33] J.A. Thornton. Influence of substrate temperature and deposition rate on structure of thick sputtered Cu coatings, Journal of Vacuum Science and Technology 12 (1975) 830-835.
[34] D. Rafaja, C. Wüstefeld, C. Baehtz, V. Klemm, M. Dopita, M. Motylenko, C. Michotte, M. Kathrein. Effect of internal interfaces on hardness and thermal stability of nanocrystalline $Ti_{0.5}Al_{0.5}N$ coatings, Metallurgical and Materials Transactions A 42 (2011) 559-569.
[35] Y. Zhang, H.J. Whitlow, T. Winzell, I.F. Bubb, T. Sajavaara, K. Arstila, J. Keinonen. Detection efficiency of time-of-flight energy elastic recoil detection analysis systems, Nuclear Instruments and Methods in Physics Research Section B: Beam Interactions with Materials and Atoms 149 (1999) 477-489.
[36] W.C. Oliver, G.M. Pharr. An improved technique for determining hardness and elastic modulus using load and displacement sensing indentation experiments, Journal of materials research 7 (1992) 1564-1583.
[37] A.C. Fischer-Cripps. Critical review of analysis and interpretation of nanoindentation test data, Surface and Coatings Technology 200 (2006) 4153-4165.
[38] K. Kadas, G. Kern, J. Hafner. Ab initio studies of the (111) and (1^{-} 1^{-} 1^{-}) surfaces of cubic BN: Structure and energetics, Physical Review B 58 (1998) 15636.
[39] A. Khein, D.J. Singh, C.J. Umrigar. All-electron study of gradient corrections to the local-density functional in metallic systems, Physical Review B 51 (1995) 4105.
[40] M. Maoujoud, M. Jardinier-Offergeld, F. Bouillon. Synthesis and characterization of thin-film molybdenum nitrides, Applied surface science 64 (1993) 81-89.
[41] Z.G. Pinsker, S.V. Kaverin. Sov. Phys. Crystallogr. (Engl. Transl.) 3 (1957) 380.
[42] L. Toth. Transition metal carbides and nitrides, Elsevier, 2014.
[43] L. Toth. Transition Metal Carbides and Nitrides (Academic, New York, 1971), and references therein (1992) 87.
[44] H. Bilz. Über Elektronenzustände von Hartstoffen mit Natriumchloridstruktur, Zeitschrift für Physik 153 (1958) 338-358.
[45] S.-H. Jhi, J. Ihm, S.G. Louie, M.L. Cohen. Electronic mechanism of hardness enhancement in transition-metal carbonitrides, Nature 399 (1999) 132-134.
[46] H. Holleck. Material selection for hard coatings, J. Vac. Sci. Technol., A 4 (1986) 2661-2669.
[47] S.-H. Jhi, S.G. Louie, M.L. Cohen, J. Ihm. Vacancy hardening and softening in transition metal carbides and nitrides, Physical Review Letters 86 (2001) 3348.
[48] P.H. Mayrhofer, A. Hörling, L. Karlsson, J. Sjölén, T. Larsson, C. Mitterer, L. Hultman. Self-organized nanostructures in the Ti-Al-N system, Applied Physics Letters 83 (2003) 2049-2051.

5.2. Composition driven phase evolution and mechanical properties of Mo–Cr–N hard coatings

Abstract

Although many research activities concentrate on transition metal nitrides, due to their excellent properties, only little is known for Mo–N based materials. We investigate in detail the influence of Cr on the structural evolution and mechanical properties of Mo–N coatings prepared at different nitrogen partial pressures. The chemical composition as well as the structural development of coatings prepared with N_2-to-total pressure ratios (p_{N2}/p_T) of 0.32 and 0.44, can best be described by the quasi-binary Mo_2N–CrN tie line. Mo_2N and CrN are face centered cubic (fcc), only that for Mo_2N half of the N-sublattice is vacant. Consequently, with increasing Cr content also the N-sublattice becomes less vacant and the chemical composition of fcc single-phase ternaries can be described as $Mo_{1-x}Cr_xN_{0.5(1+x)}$. These coatings exhibit an excellent agreement between experimentally and *ab initio* obtained lattice parameters of fcc $Mo_{1-x}Cr_xN_{0.5(1+x)}$. When increasing the N_2-to-total pressure ratio to p_{N2}/p_T = 0.69, the N-sublattice is already fully occupied for Cr-additions of $x \geq 0.4$, as suggested by elastic recoil detection analysis and lattice parameter variations. The latter follows the *ab initio* obtained lattice parameters along the quasi-binary MoN–CrN tie line for $x \geq 0.5$. The single-phase fcc coating with Cr/(Mo+Cr) of x ~0.2, prepared with p_{N2}/p_T = 0.32, exhibits the highest hardness of ~34 GPa among all coatings studied.

I. Introduction

Many research activities are conducted on TiN, ZrN, and CrN based coatings [1-8], but only little is known for Mo–N based materials. Mo–N coatings and especially face centered cubic phase γ-Mo_2N – due to its high hardness and excellent tribological performance – are promising candidates for many applications, like protective coatings against rapid tool wear [9-13]. Structure and phase development of Mo–N coatings are extremely sensitive to the N_2-partial pressure used during depositions. With increasing nitrogen partial pressure, the formation of the hexagonal close packed hcp δ-MoN ($P6_3/mmc$) [14, 15] is promoted next to face centered cubic (fcc) γ-Mo_2N (Fm-3m) [16]. For extremely high nitrogen pressures, even the metastable ξ-MoN (Fm-3m) is accessible [17].

However, the formation of interatomic bonds in Mo–N, by filling of antibonding electron states, results in low chemical and thermal stability [18]. Therefore, we use the concept of alloying Mo–N with Cr, to increase the chemical and thermal stability. Especially the oxidation resistance will significantly be improved due to the formation of a dense Cr-rich oxide, such as shown for Cr–N coatings [19]. Zhou et al. [20] highlighted that single-phase cubic structured Mo–Cr–N phases exhibit a high driving force towards an isostructural decomposition – providing a high potential for spinodal decomposition similar to single-phase cubic structured Ti–Al–N [21]. With increasing Mo content, the metallic bonding character within single-phase cubic Mo–Cr–N increases, leading to an improved ductility [22]. Besides the computational

studies [20, 23], there are further experimental investigations within the Mo–Cr–N system [5, 24-29], but these often yield contradictory results. For example, the addition of Mo reduces [5, 29] or increases [25, 27] the mechanical properties of Cr–N. Furthermore, all experimental studies [25-27, 30] focussed on the Cr-rich side with Cr/(Mo+Cr) atomic ratios above 0.5.

Therefore, we concentrate our investigations on the Mo-rich side of Mo–Cr–N coatings with Cr/(Mo+Cr) atomic ratios below 0.5. Varying the N_2-to-total pressure ratio, p_{N2}/p_T, during deposition, allows the development of ternary coatings along the quasi-binary Mo_2N–CrN or MoN–CrN tie line with predominant face centered cubic structure.

II. Experimental details

Various Mo–Cr–N coatings are synthesized, using a modified Leybold Heraeus Z400 magnetron sputtering system, in mixed Ar and N_2 (both gases with purity above 99.999%) glow discharges. Small cubes of Cr (99.99% purity, 3x3x3mm^3) were uniformly arranged (4, 8, 12, 16, 20, and 36 pieces) on the race track of a molybdenum target (99.99% purity, Ø75mm) to vary the Cr/(Mo+Cr) ratio within the films prepared. The substrates are centered parallel above the target at a distance of 55 mm. All depositions were prepared with 0.4 A DC target current and floating potential of the substrates (~ -15 V), a total pressure, p_T, of 0.35 Pa, and a substrate temperature of 450±20°C. The latter one corresponds to an homologous temperature T/T_m of about 0.3 of these nitrides [14] and based on Thornton's zone model [31] suggests for a zone T structure. The chamber was always evacuated to a base pressure of $p_{base} \leq 5 \cdot 10^{-4}$ Pa. Pre-studies showed that single-phase face centered cubic Mo_2N coatings can be prepared with N_2-to-total pressure ratios, p_{N2}/p_T, between 0.32 and 0.44. Higher ratios result in an increasing phase fraction of hcp δ-MoN. Contrary, single phase face centered cubic c-CrN coatings can be synthesized for ratios $p_{N2}/p_T \geq 0.44$, lower ratios promote the crystallization of hexagonal close packed h-Cr_2N. Figure 1 shows a scheme of these phase evolutions. Based on these pre-studies, the Mo–Cr–N coatings are prepared with three different N_2-to-total pressure ratios, p_{N2}/p_T = 0.32, 0.44, or 0.69, to allow for the development of single-phase ternary coatings.

Phase analyses were performed with an X-ray diffractometer Philips X'Pert using monochromized Cu K_α radiation. Lattice parameters and dimensions of coherently scattering domains, *d*, were obtained by Williamson Hall plots and pseudo-Voigt approximations, respectively. Fracture cross-sections of coated Si-substrates are investigated by scanning electron microscopy (FEI Quanta 200 FEGSEM with a spatial resolution of about 2 nm) for evaluating the film growth morphology. An integrated EDAX Genesis system allows analysing the elemental composition by means of energy dispersive X-ray spectroscopy (EDS). Several samples were investigated by Time-of-flight Elastic Recoil Detection (TOF-ERDA) to calibrate the EDS using 36 MeV ^{127}I primary ions at the tandem accelerator at Uppsala University, Sweden. The recoil detection angle in the ERDA experiments was 45°. More details on TOF-ERDA can be found elsewhere [32]. Further investigations of the growth morphology and film structure is conducted by transmission electron microscopy (TEM) using a FEI TECNAI F20 operated at 200 kV, with lattice resolution of about 0.14 nm.

Indentation hardness, *H*, and modulus, *E*, of the coatings on austenitic substrates (due to the better adhesion) are characterized with a UMIS unit equipped with a Berkovich diamond tip and applying loads within the range of 3 to 30 mN. The film-only indentation hardness, *H*, and modulus, *E*, are obtained by evaluating the load-displacement curve after Oliver and Pharr [33]. Subsequently, in order to guarantee for minimized substrate interference, only indentations from a fully developed plastic zone are used, i.e. a region of nearly constant values of indentation hardness and modulus over the penetration depth ("plateau" method). For the case of partially-developed plastic zone, i.e. insufficient coating thickness, the film-only indentation modulus, *E*, resulted from extrapolation of the measured values back to zero indentation depth [34]. All data are analysed with a Poisson's ratio, *v*, of 0.25 for our Mo–Cr–N thin films. The indenter geometry correction factor was obtained through indentation tests with varying maximum loads of fused silica with known *E* and *v* values of 72.5 GPa and 0.17, respectively [35]. Verification of *H* and *E* is carried out with series of well-characterized single phase and polycrystalline reference samples: fused silica, silicon, and sapphire. The coatings are also characterized for their as-deposited biaxial stresses using the cantilever beam method and applying the Stoney equation [36].

III. Results

The nitrogen content of our Mo–N coatings increases from 35 to 41 at.% (i.e. $MoN_{0.53}$ to $MoN_{0.68}$) and of the Cr–N coatings from 50 to 55 at.% (i.e. $CrN_{1.01}$ to $CrN_{1.22}$) with increasing p_{N2}/p_T from 0.32 to 0.69, causing the phase composition to develop according to Figs. 1b and c.

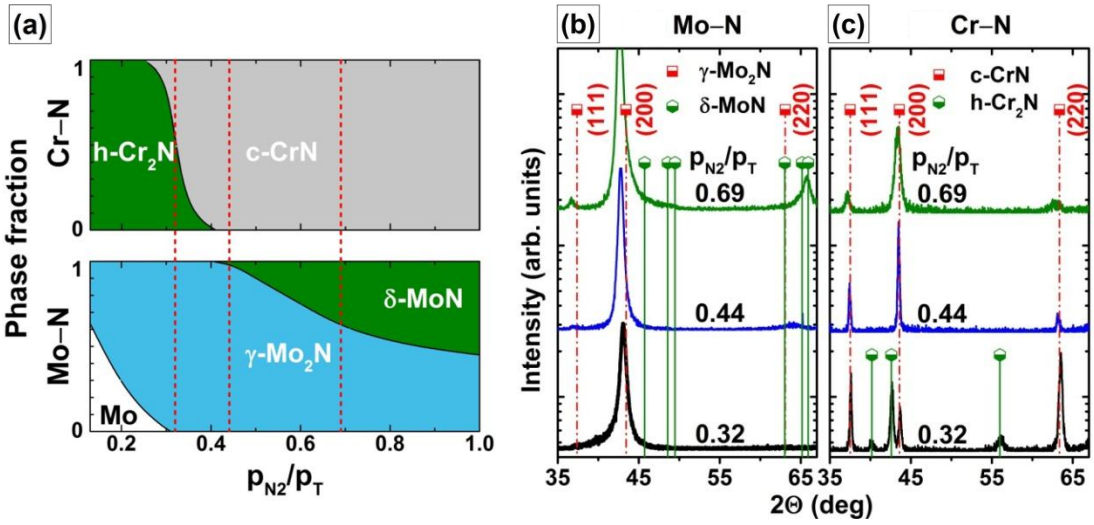

Fig. 1. (a) Schematic illustration of the phase evolution with increasing N_2-to-total pressure ratios, p_{N2}/p_T, used during deposition of binary Mo–N and Cr–N coatings (the red dashed vertical lines indicate three p_{N2}/p_T ratios, 0.32, 0.44, and 0.69, used for the current study). And XRD patterns of binary (b) Mo–N and (c) Cr–N with labelled N_2-to-total pressure ratios, p_{N2}/p_T = 0.32, 0.44, and 0.69, used during deposition. The indicated phases are γ-Mo_2N (ICDD 00-025-1366), δ-MoN (ICDD 01-072-9061), c-CrN (ICDD 01-077-0047), and h-Cr_2N (ICDD 00-035-0803).

The increasing deposition rate from 1.2 to 1.4 nm/s for Mo–N coatings with increasing p_{N2}/p_T from 0.44 to 0.69 is mainly based on the formation of hexagonal MoN phases next to face centered cubic γ-Mo_2N, see Fig. 1b. For Cr–N coatings, we can detect hexagonal close packed h-Cr_2N phases next to c-CrN with p_{N2}/p_T = 0.32, but only c-CrN with p_{N2}/p_T = 0.44, leading to decreasing deposition rates from 1.3 to 0.8 nm/s. Please note that the nitrogen-rich phase is face centered cubic for Cr–N, but hexagonal for Mo–N. The packing density is significantly higher for the face centered cubic phases than that for the hexagonal phases. Consequently, the deposition rate increases with increasing fraction of the hexagonal phases (for Cr–N as well as for Mo–N). The further reduction in deposition rate for CrN_y coatings to 0.8 nm/s upon increasing p_{N2}/p_T to 0.69 is mainly based on poisoning effects [37, 38], as the coating is still single-phase cubic structured, see Fig. 1c. The chromium content within our Mo–Cr–N films increases from 0 to ~32 at.% with increasing number of Cr-cubes (from 0 to 36) at the Mo-target.

Our elemental analysis suggests that with increasing Cr content also the incorporated nitrogen increases, for example from 35 to 38 at.% when using p_{N2}/p_T = 0.32, see Fig. 2a. Corresponding results are also obtained for p_{N2}/p_T = 0.44 and 0.69, where the Cr-content also increases from 0 to ~30 at.%, but the nitrogen increases approximately from 39 to 45 at.% and from 40 to 51 at.%, respectively. These data indicate that the nitrogen content within our Mo–Cr–N films is closely related to the metal sublattice population, as highlighted in Fig. 2b.

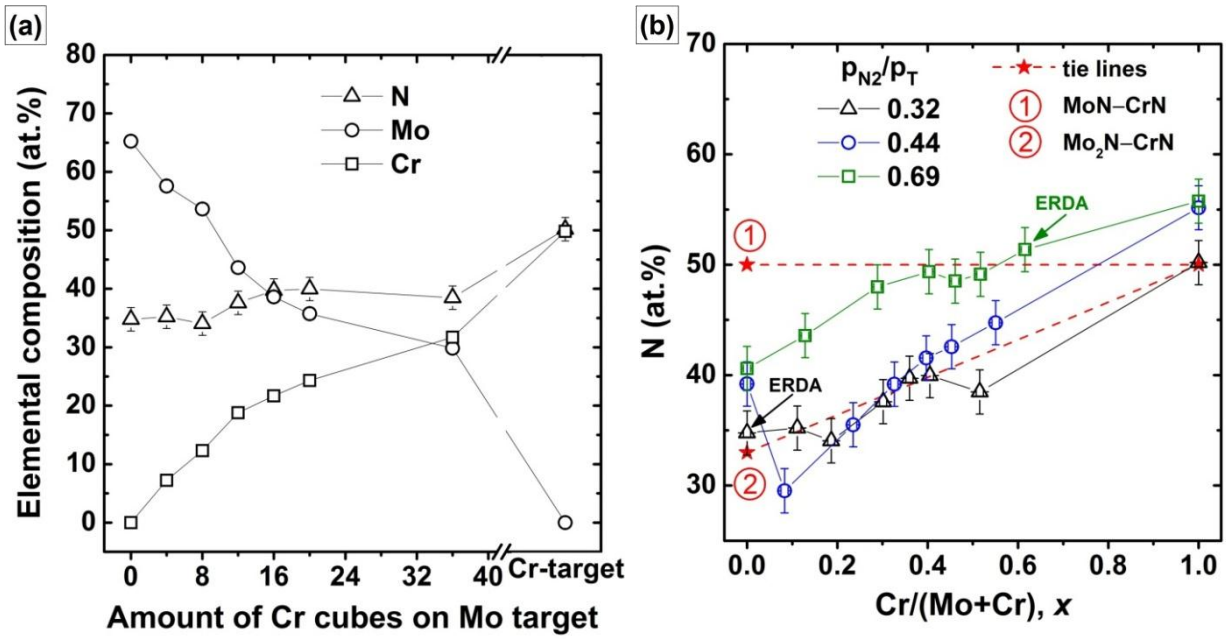

Fig. 2. Elemental composition, obtained by EDS and verified for $MoN_{0.54}$ and $Mo_{0.62}Cr_{0.38}N_{1.04}$ by ERDA, of Mo–Cr–N coatings deposited with p_{N2}/p_T = 0.32 and different amount of Cr cubes placed on the Mo-target race track. (a) The error bars for Cr- and Mo-concentrations are smaller than the symbol size. And (b), nitrogen concentration (in at.%) within our ternary $Mo_{1-x}Cr_xN_y$ coatings, prepared with p_{N2}/p_T = of 0.32, 0.44, and 0.69, as a function of their Cr/(Mo+Cr)-ratio, *x*. The two coatings, which are investigated by Elastic Recoil Detection Analysis, are labelled with ERDA. The error bars for Cr/(Mo+Cr)-ratios are smaller than the symbol size.

Here, two red dash-dotted lines, labelled with 1 and 2, indicate the quasi-binary tie lines Mo_2N–CrN and MoN–CrN, respectively. The comparison clearly suggests that the chemical compositions of our coatings prepared with lower p_{N2}/p_T-ratios of 0.32 and 0.44, follow the quasi-binary Mo_2N–CrN tie line. Hence, their composition can be described by $Mo_{1-x}Cr_xN_{0.5(1+x)}$, highlighting that with the addition of Cr, *x*, also the N content increases with a factor of 0.5(1+*x*). When increasing p_{N2}/p_T-ratios to 0.69, the chemical composition meets the MoN–CrN quasi-binary tie line for Cr/(Mo+Cr) ratios ≥ 0.4, see Fig. 3b, as the nitrogen content within the Cr-free MoN_y coatings is already between Mo_2N and MoN. To highlight the population of the N-sublattice in our films, we will use the metal-sublattice-normalized notification of $Mo_{1-x}Cr_xN_y$.

Cross-sectional SEM investigations – such as shown for $Mo_{0.60}Cr_{0.40}N_{0.67}$ prepared with p_{N2}/p_T = 0.32, Fig. 3a, and $Mo_{0.48}Cr_{0.52}N_{0.96}$ prepared with p_{N2}/p_T = 0.69, Fig. 3b – reveal a columnar growth microstructure and smooth surfaces for all ternary Mo–Cr–N coatings studied. This is furthermore represented by the cross-sectional TEM investigations of the $Mo_{0.70}Cr_{0.30}N_{0.61}$ coating (p_{N2}/p_T = 0.32), Fig. 3c. The corresponding SAED pattern (see the inset in Fig. 3c) clearly indicates only a face centered cubic structure.

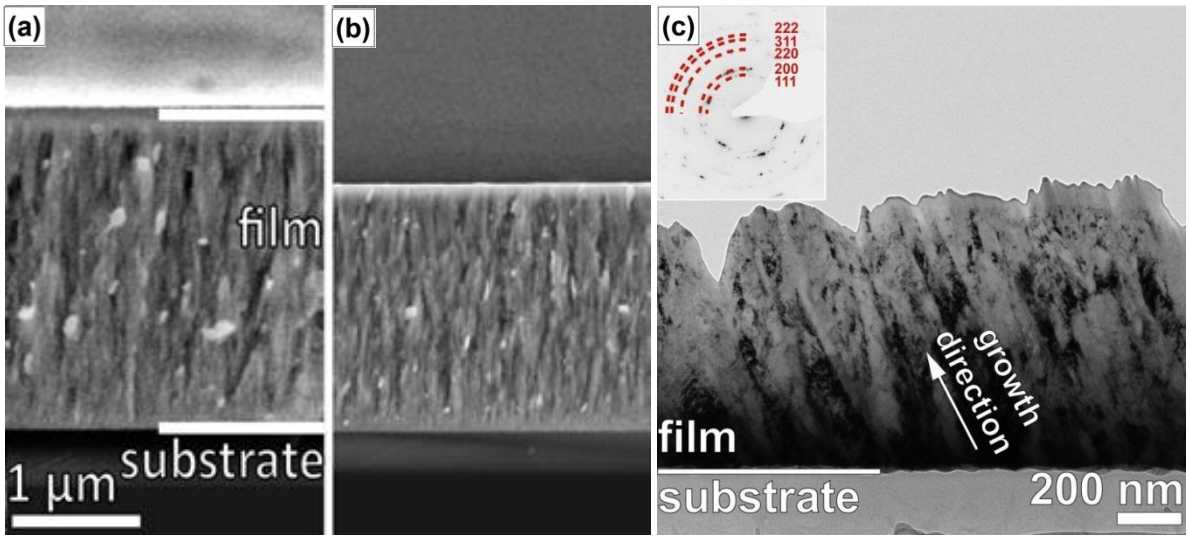

Fig. 3. Fracture cross-section SEM images of $Mo_{0.60}Cr_{0.40}N_{0.67}$ prepared with p_{N2}/p_T = 0.32 (a) and $Mo_{0.48}Cr_{0.52}N_{0.96}$ prepared with p_{N2}/p_T = 0.69 (b) as well as cross-section TEM image of $Mo_{0.70}Cr_{0.30}N_{0.61}$ prepared with p_{N2}/p_T = 0.32 (c). The small inset is the SAED of a representative area within the coating.

This is also clearly represented by the XRD investigations, Fig. 4. All ternary Mo–Cr–N coatings prepared with p_{N2}/p_T = 0.32 and 0.44 are single-phase face centered cubic structured with a pronounced (200) growth orientation, Figs. 4a and 4b, respectively. However, for the highest nitrogen partial pressure used, p_{N2}/p_T = 0.69, connected with the lowest Cr content of the ternary Mo–Cr–N coatings, small XRD peaks of the hexagonal δ-MoN-based phase can be detected, see Fig. 4c. However, these coatings are also single-phase face centered cubic structured, if their Cr content is above 15 at.% (or the Cr/(Mo+Cr)-ratio, *x*, is above 0.29). The dimensions of coherently scattering domains, obtained by Warren Averbach analysis of the XRD patterns, of all ternary Mo–Cr–N coatings investigated are between 10 and 30 nm.

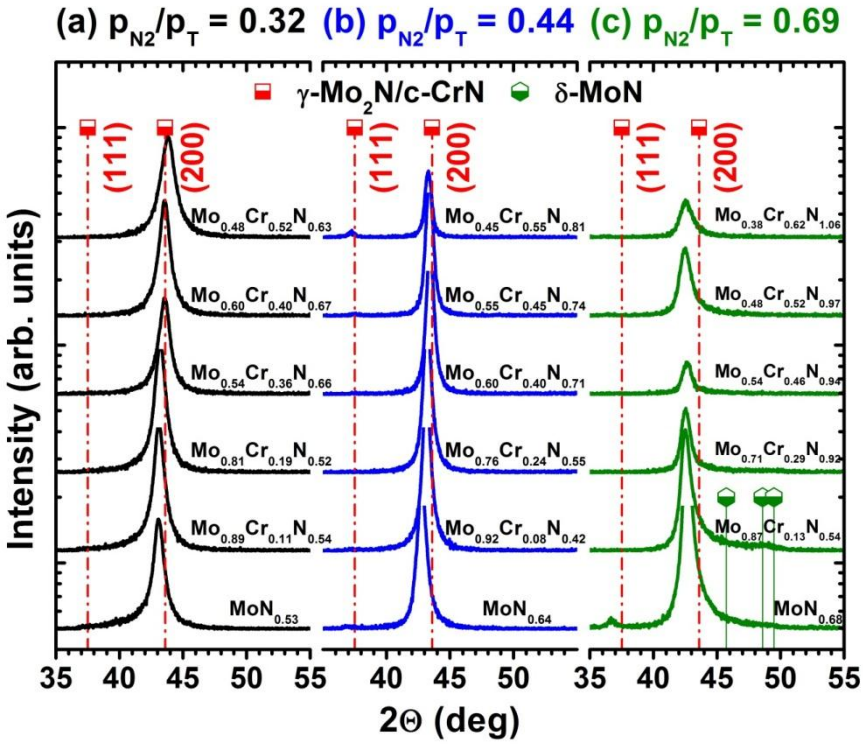

Fig. 4. X-ray diffraction patterns of our Mo–Cr–N thin films prepared with p_{N2}/p_T = 0.32 (a), 0.44 (b), and 0.69 (c). The labels, added to the patterns, indicate the chemical composition according to our metal-sublattice-normalized notification, $Mo_{1-x}Cr_xN_y$.

The pronounced (200)-peaks are used to derive the corresponding lattice parameters of the cubic $Mo_{1-x}Cr_xN_y$ solid solution with respect to their Cr content and p_{N2}/p_T ratios used during deposition, see Fig. 5a. The lattice parameters of the coatings prepared with p_{N2}/p_T = 0.32 and 0.44 are in excellent agreement with *ab initio* calculated values for face centered cubic $Mo_{1-x}Cr_xN_{0.5(1+x)}$ solid solutions. Consequently, in addition to the chemical composition (Fig. 2b), also the lattice parameters suggest that these coatings are composed of fcc solid solutions along the Mo_2N–CrN quasi-binary tie line. The lattice parameters of the coatings prepared with the highest p_{N2}/p_T-ratio of 0.69 meets the *ab initio* obtained lattice parameters of fcc solid solution $Mo_{1-x}Cr_xN$ [20] along the quasi-binary MoN–CrN tie line for Cr contents *x* above 0.4, see Fig. 5a. The lattice parameter variations are actually in excellent agreement with the chemical variation, especially with respect to the nitrogen content. For example, with increasing nitrogen content of the binary MoN_y coating from 35 to 41 at.%, the lattice parameter increases from 4.199 to 4.242 Å, suggesting that the fcc γ-Mo_2N structure (half occupied N sublattice, hence actually, fcc $MoN_{0.5}$) approaches the metastable fcc ξ-MoN structure (with fully occupied N sublattice).

This significant increase in lattice parameter of the fcc structure within our Mo–N coatings is not represented in their compressive biaxial stresses, which are at around -1.2 GPa for p_{N2}/p_T = 0.32, 0.44, and 0.69, see Fig. 5b. We envision that the formation of a small fraction of δ-MoN phases next to fcc-Mo_2N for p_{N2}/p_T = 0.44 and 0.69 – as suggested by the XRD studies, see Fig. 1b – counteracts for the expected increasing compressive stresses when filling the N-sublattice.

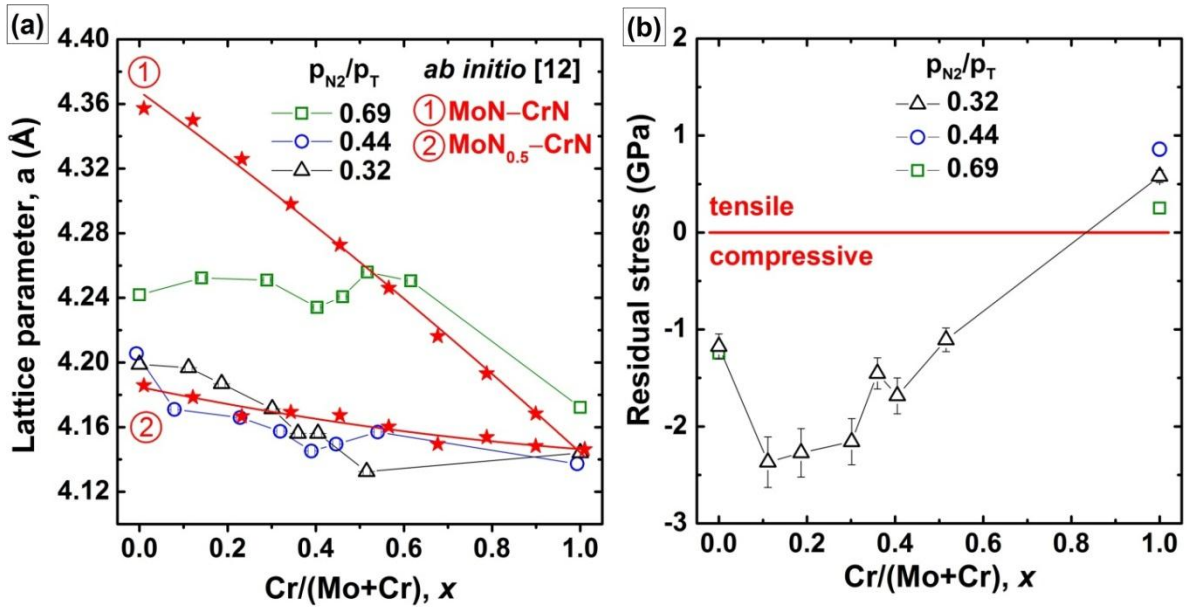

Fig. 5. (a) Lattice parameters of our Mo–Cr–N coatings, based on their face centered cubic (200)-reflex, as a function of their Cr-content, *x*, and p_{N2}/p_T-ratios used during deposition. The symbols along the two red dashed tie lines, MoN–CrN and $MoN_{0.5}$–CrN, represent *ab initio* obtained lattice parameters for fcc-$Mo_{1-x}Cr_xN$ and for fcc-$Mo_{1-x}Cr_xN_{0.5(1+x)}$, respectively [20]. The error bars for Cr/(Mo+Cr)-ratios are smaller than the symbol size. And (b) biaxial residual stresses of our Mo–Cr–N coatings deposited with p_{N2}/p_T = 0.32. The stresses for binary Mo–N and Cr–N prepared with p_{N2}/p_T = 0.44 and 0.69 are added for comparison. The error bars for Cr/(Mo+Cr)-ratios are smaller than the symbol size.

The formation of δ-MoN phases, when increasing p_{N2}/p_T from 0.32 to 0.44 or 0.69, is also represented by the decreasing hardness from 33 to 28 GPa, see Fig. 6. The indentation modulus only slightly decreases from 425 to 412 GPa.

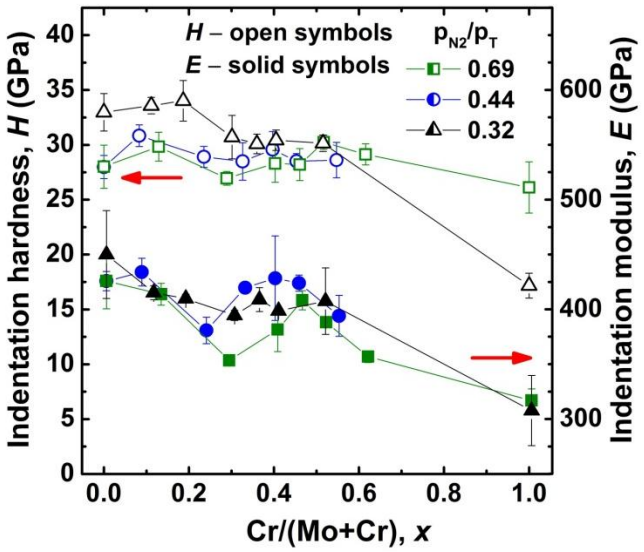

Fig. 6. Indentation hardness (open symbols) and modulus (solid symbols) of our Mo–Cr–N thin films as a function of their Cr content, *x*, and p_{N2}/p_T-ratios used during deposition. The error bars for Cr/(Mo+Cr)-ratios are smaller than the symbol size.

The binary CrN exhibits an even more pronounced change in hardness from H = 17 to 26 GPa upon increasing the N_2-to-total pressure ratio from 0.32 to 0.69, because here the structure significantly changes from mixed h-Cr_2N + c-CrN to single phase c-CrN, see Fig. 1c. Thereby, also the tensile stresses are reduced from +0.3 to +0.1 GPa (Fig. 5b). Corresponding results (increasing hardness and decreasing tensile stresses of magnetron sputtered CrN coatings with increasing N_2 content of the working gas) are already reported earlier [39].

The majority of the ternary $Mo_{1-x}Cr_xN_y$ coatings exhibit hardnesses between 28 and 31 (±2) GPa (almost within the error of measurement) with no significant dependence on the Cr content within the investigated region of $0.1 \leq x \leq 0.6$, see Fig. 6. However, the data clearly suggest that the coatings prepared with the lowest p_{N2}/p_T exhibit hardnesses at the upper limit, whereas those prepared with the highest p_{N2}/p_T exhibit hardnesses at the lower limit of the 28 – 31 GPa range. Consequently, the two ternary Mo–Cr–N coatings with hardnesses above this range (H = 33±1 GPa for $Mo_{0.89}Cr_{0.11}N_{0.54}$ and H = 34±2 GPa for $Mo_{0.81}Cr_{0.19}N_{0.52}$) are prepared with p_{N2}/p_T = 0.32, and the only ternary Mo–Cr–N coating with a hardness below this range (H = 27±1 GPa for $Mo_{0.71}Cr_{0.29}N_{0.92}$) is prepared with p_{N2}/p_T = 0.69. This coating exhibits also the lowest indentation modulus of 353±5 GPa among all ternary Mo–Cr–N coatings studied. Similar to the hardness, most Mo–Cr–N coatings have similar indentation moduli (between 390±10 and 410±10 GPa) with no significant dependence on the Cr content.

The slightly decreasing hardnesses with increasing Cr content of our ternary $Mo_{1-x}Cr_xN_y$ coatings – especially when prepared with p_{N2}/p_T = 0.32 – is well represented by their decreasing compressive stresses.

IV. Discussion

As mentioned in the introduction, PVD allows to prepare metastable ξ-MoN (*Fm-3m*) [17], if the ionization degree and/or the nitrogen partial pressure is very high. This metastable phase is based on the stable high-temperature phase fcc γ-Mo_2N (*Fm-3m*) [14, 40], but with (theoretically) fully occupied octahedral sites of the fcc structure formed by Mo. Within fcc γ-Mo_2N, these octahedral sites are only half-filled with randomly distributed nitrogen. Hence, our metal-sublattice-normalized notification (see the introduction), $MoN_{0.5}$, would be more correct. However, due to the possible formation of ξ-MoN or γ-Mo_2N, both quasi-binary tie lines (Mo_2N–CrN and MoN–CrN) are important for the discussion of chemistry, structure, and phase evolution within ternary Mo–Cr–N coatings prepared at higher N_2-to-total pressures. We do not consider the quasi-binary tie line Mo_2N–Cr_2N, which would be relevant for rather low N_2-partial pressures, where also metallic Mo-phases develop, see Fig. 1a.

Even for the highest N_2-to-total pressure ratio used (p_{N2}/p_T = 0.69) no ξ-MoN phase, with a (theoretically) fully occupied N-sublattice was formed. Their nitrogen content is about 41 at.% (i.e., $MoN_{0.68}$, see Fig. 2b), but here already a small phase fraction of hcp δ-MoN can be detected by XRD, compare Figs. 2b and 1a, b. The maximum nitrogen solubility within fcc MoN_y is $y \approx 0.55$ under thermodynamic equilibrium conditions [14]. However, when investigating the

lattice parameter of the face centered cubic structure, a pronounced increase with increasing p_{N2}/p_T is obtained, see Fig. 5a. The comparison with the calculated values for γ-Mo_2N and ξ-MoN clearly suggests that the amount of nitrogen-vacancies, which is 50% of the fcc N-sublattice within γ-Mo_2N, decreases to nearly 38% with increasing p_{N2}/p_T. Hence, nearly single-phase γ-$MoN_{0.62}$ (using the simplified linear interpolation between $MoN_{0.5}$ and MoN) can be synthesized by reactive magnetron sputtering. A corresponding result was already suggested by V. Anitha *et al.* [16]. However, we need to mention that the accuracy for nitrogen detection within the EDS system used is by around ±2 at.%, which we confirmed by ERDA measurements of $MoN_{0.54}$ and $Mo_{0.62}Cr_{0.38}N_{1.04}$. This would lead to the following three notations, $MoN_{0.53\pm0.05}$, $MoN_{0.65\pm0.05}$, and $MoN_{0.68\pm0.06}$, for the coatings prepared with p_{N2}/p_T = 0.32, 0.44, and 0.69, respectively. Consequently, also the CrN coatings would have chemical compositions of $CrN_{1.01\pm0.04}$, $CrN_{1.23\pm0.06}$, and $CrN_{1.26\pm0.06}$. Actually the lower values, especially for CrN_y would agree better with the XRD investigations, suggesting a small fraction of h-Cr_2N next to the dominating c-CrN for the coating prepared with p_{N2}/p_T = 0.32.

Nitrogen over-stoichiometric compositions can be explained by metal vacancies, nitrogen ions on anti-sites (N on metal places), and the formation of nitrogen interstitials [41, 42]. However, for CrN_y, the latter is energetically un-preferred (by more than 0.1 eV/at) over the previous two mechanisms for nitrogen contents above 52 at.%, i.e., $y \geq 1.1$ [42].

Based on the chemical (Fig. 2) and structural (Fig. 4) investigations of our ternary $Mo_{1-x}Cr_xN_y$ coatings we can conclude that the Cr content and the N_2-partial pressure used during deposition determine the population of the N-sublattice of the face centered cubic structure. If we use a high nitrogen partial pressure (p_{N2}/p_T = 0.69), the nitrogen content in our ternary coatings rapidly increases to $y \geq 1$ (i.e., N-content ≥ 50 at.%) with increasing Cr-content to $x \geq 0.4$ (i.e., Cr-content ≥ 20 at.%), suggesting for a (theoretically) fully occupied N-sublattice. Consequently, the lattice parameter of the fcc phase approaches and follows the calculated values for fcc c-$Mo_{1-x}Cr_xN$. Our results (chemistry and structure) clearly suggest that the single-phase solid solution fcc c-$Mo_{1-x}Cr_xN$ can be prepared by reactive magnetron sputtering for $x \geq 0.4$ (i.e., up to 60 at.% of Mo at the metal sublattice); although, Mo is thermodynamically insoluble (at least for contents above 1 at.%) in c-CrN [43].

For low nitrogen-partial pressures (p_{N2}/p_T = 0.32 and 0.44), the nitrogen content closely follows the quasi-binary tie line Mo_2N–CrN, see Fig. 2b. Consequently, the chemistry of our ternary $Mo_{1-x}Cr_xN_y$ coatings can nearly be described with $Mo_{1-x}Cr_xN_{0.5(1+x)}$, meaning that half as many nitrogen ions are additionally added to the half-filled N-sublattice as Cr ions substitute for Mo, $y = 0.5(1+x)$. (In other words, for the substitution of two Mo-ions with two Cr-ions, one vacancy of the N-sublattice within a γ-$MoN_{0.5}$ based structure is removed). This is also represented by the lattice parameter variation of the fcc phase with the Cr-content x, which follows the *ab initio* calculated values for fcc c-$Mo_{1-x}Cr_xN_{0.5(1+x)}$, see Fig. 5a.

Contrary to some previous studies [5, 30], which actually concentrate only on the Cr-rich side of Mo–Cr–N (with Cr/(Mo+Cr) ratios above 0.4, hence $x > 0.4$), we obtain higher hardnesses and indentation moduli for all of our ternary $Mo_{1-x}Cr_xN_y$ coatings than for CrN, see

Fig. 6. The highest hardness is obtained for the single-phase fcc c-$Mo_{0.81}Cr_{0.19}N_{0.52}$ coating, prepared with p_{N2}/p_T = 0.32, which actually exhibits comparable indentation moduli to the other ternaries. Therefore, this coating also yields the highest resistance against plastic deformation (H^3/E^2 [44]) of 0.2 GPa.

V. Conclusions

Magnetron sputtered Mo–Cr–N coatings are studied in detail as a function of their chemical composition and N_2-to-total pressure ratios, p_{N2}/p_T, used during deposition. The Mo–N and all ternary coatings studied exhibit a pronounced face centered cubic 200-growth orientation with small coherently scattering domains between 10 and 30 nm. All ternary coatings prepared with p_{N2}/p_T = 0.32 and 0.44 are single-phase fcc structured with a chemistry along the quasi-binary Mo_2N–CrN tie line. This can be described by $Mo_{1-x}Cr_xN_{0.5(1+x)}$, indicating that with the addition of Cr, x, also the vacant sites at the N-sublattice decreases, by 0.5x. This is additionally confirmed by their lattice parameters, which are in excellent agreement with *ab initio* obtained values for fcc c-$Mo_{1-x}Cr_xN_{0.5(1+x)}$.

Preparing the Mo–N coatings with a high N_2-to-total pressure ratio, p_{N2}/p_T = 0.69, leads to the formation of fcc c-$MoN_{0.68}$ – where a part of the N-vacancies at the N-sublattice of γ-$MoN_{0.5}$ is occupied – and a small fraction of hcp δ-MoN. However, for Cr-contents of $x \geq 0.29$, all coatings are again single-phase fcc structured and their chemistry as well as lattice parameters approach and follow the quasi-binary MoN–CrN tie line, hence c-$Mo_{1-x}Cr_xN$.

The highest hardness values of 33 – 34 GPa are obtained for the coatings prepared with the lowest N_2-to-total pressure ratio, p_{N2}/p_T = 0.32, combined with low Cr-contents of $x \leq 0.19$. All other ternary $Mo_{1-x}Cr_xN_y$ and MoN_y coatings exhibit hardnesses within the range 28 – 31 GPa, with a tendency for lower values when prepared with p_{N2}/p_T = 0.69. These data indicate that filling the N-vacancies, of the N-sublattice, within the fcc γ-$MoN_{0.5}$ based structure leads to a hardness reduction. The indentation moduli decrease from ~440 GPa for fcc c-$MoN_{0.53}$ to ~350 GPa for fcc c-$Mo_{0.38}Cr_{0.62}N_{1.06}$ with increasing Cr content, x. The binary CrN_y coatings have indentation moduli of ~310 GPa. Consequently, the coating c-$Mo_{0.81}Cr_{0.19}N_{0.52}$, which exhibits the highest hardness of 34 ± 2 GPa among all coatings studied, also exhibits the highest resistance against plastic deformation with $H^3/E^2 \approx 0.2$ GPa.

Based on our results we can conclude that fcc c-$Mo_{1-x}Cr_xN_y$ films – especially with a low Cr-content and a high density of N-vacancies – provide excellent mechanical properties to be beneficial for many industrial applications.

Acknowledgements

The financial support by the START Program (Y371) of the Austrian Science Fund (FWF) is gratefully acknowledged. The authors are thankful to the XRC, USTEM, and VSC of the TU Wien.

References

[1] A. Elyutin, I. Blinkov, A. Volkhonsky, D. Belov. Properties of nanocrystalline arc PVD TiN-Cu coatings, Inorganic Materials 49 (2013) 1106-1112.

[2] C. Wüstefeld, D. Rafaja, V. Klemm, C. Michotte, M. Kathrein. Effect of the aluminium content and the bias voltage on the microstructure formation in $Ti_{1-x}Al_xN$ protective coatings grown by cathodic arc evaporation, Surface and Coatings Technology 205 (2010) 1345-1349.

[3] P. Mayrhofer, D. Sonnleitner, M. Bartosik, D. Holec. Structural and mechanical evolution of reactively and non-reactively sputtered Zr–Al–N thin films during annealing, Surface and Coatings Technology 244 (2014) 52-56.

[4] M.B. Kanoun, S. Goumri-Said. Effect of alloying on elastic properties of ZrN based transition metal nitride alloys, Surface and Coatings Technology 255 (2014) 140-145.

[5] P. Hones, R. Sanjines, F. Lévy. Sputter deposited chromium nitride based ternary compounds for hard coatings, Thin Solid Films 332 (1998) 240-246.

[6] P.H. Mayrhofer, D. Music, T. Reeswinkel, H.G. Fuß, J.M. Schneider. Structure, elastic properties and phase stability of $Cr_{1-x}Al_xN$, Acta Materialia 56 (2008) 2469-2475.

[7] J. Musil. Hard and superhard nanocomposite coatings, Surface and Coatings Technology 125 (2000) 322-330.

[8] I. Blinkov, A. Volkhonskii. The effect of deposition parameters of multilayered nanostructure Ti-Al-N/Zr-Nb-N/Cr-N coatings obtained by the arc-PVD method on their structure and composition, Russian Journal of Non-Ferrous Metals 53 (2012) 163-168.

[9] J. Valli, U. Mäkelä, H. Hentzell. Tribological properties of MoN_x coatings in contact with copper, Journal of Vacuum Science & Technology A 4 (1986) 2850-2854.

[10] W.D. Sproul, M.E. Graham, M.-S. Wong, P.J. Rudnik. Reactive unbalanced magnetron sputtering of the nitrides of Ti, Zr, Hf, Cr, Mo, Ti-Al, Ti-Zr and Ti-Al-V, Surface and Coatings Technology 61 (1993) 139-143.

[11] M. Ürgen, O. Eryilmaz, A. Cakir, E. Kayali, B. Nilüfer, Y. Işik. Characterization of molybdenum nitride coatings produced by arc-PVD technique, Surface and Coatings Technology 94 (1997) 501-506.

[12] G. Gassner, P.H. Mayrhofer, K. Kutschej, C. Mitterer, M. Kathrein. Magnéli phase formation of PVD Mo–N and W–N coatings, Surface and Coatings Technology 201 (2006) 3335-3341.

[13] H. Hazar. Characterization of MoN coatings for pistons in a diesel engine, Materials & Design 31 (2010) 624-627.

[14] H. Jehn, P. Ettmayer. The molybdenum-nitrogen phase diagram, Journal of the Less Common Metals 58 (1978) 85-98.

[15] X. Zhao, K.-J. Range. High pressure synthesis of molybdenum nitride MoN, Journal of alloys and compounds 296 (2000) 72-74.

[16] V. Anitha, S. Major, D. Chandrashekharam, M. Bhatnagar. Deposition of molybdenum nitride thin films by rf reactive magnetron sputtering, Surface and Coatings Technology 79 (1996) 50-54.

[17] A. Perry, A. Baouchi, J. Petersen, S. Pozder. Crystal structure of molybdenum nitride films made by reactive cathodic arc evaporation, Surface and Coatings Technology 54 (1992) 261-265.

[18] L. Toth. Transition metal carbides and nitrides, Elsevier, 2014.

[19] P.H. Mayrhofer, H. Willmann, C. Mitterer. Oxidation kinetics of sputtered Cr–N hard coatings, Surface and Coatings Technology 146 (2001) 222-228.

[20] L. Zhou, D. Holec, P.H. Mayrhofer. Article in press (2015).

[21] P.H. Mayrhofer, A. Hörling, L. Karlsson, J. Sjölén, T. Larsson, C. Mitterer, L. Hultman. Self-organized nanostructures in the Ti–Al–N system, Applied Physics Letters 83 (2003) 2049-2051.

[22] L. Zhou, D. Holec, P.H. Mayrhofer. Ab initio study of the alloying effect of transition metals on structure, stability and ductility of CrN, Journal of Physics D: Applied Physics 46 (2013) 365301.

[23] K. Frisk. A thermodynamic evaluation of the Cr-N, Fe-N, Mo-N and Cr-Mo-N systems, Calphad 15 (1991) 79-106.

[24] Y. Benlatreche, C. Nouveau, I. Rahil, R. Marchal, L. Chekour. Comparative Studies on Mo–Cr–N and Al–Cr–N Coatings Obtained by PVD Dual Magnetron Sputtering, Plasma Processes and Polymers 6 (2009) 135-140.

[25] E.Y. Choi, M.C. Kang, D.H. Kwon, D.W. Shin, K.H. Kim. Comparative studies on microstructure and mechanical properties of CrN, Cr–C–N and Cr–Mo–N coatings, Journal of materials processing technology 187 (2007) 566-570.
[26] B. Gu, J. Tu, X. Zheng, Y. Yang, S. Peng. Comparison in mechanical and tribological properties of Cr–W–N and Cr–Mo–N multilayer films deposited by DC reactive magnetron sputtering, Surface and Coatings Technology 202 (2008) 2189-2193.
[27] K. Ho Kim, E. Young Choi, S. Gyun Hong, B. Gyu Park, J. Hong Yoon, J. Hae Yong. Syntheses and mechanical properties of Cr–Mo–N coatings by a hybrid coating system, Surface and Coatings Technology 201 (2006) 4068-4072.
[28] Y.L. Di, Z.H. Cai, P. Zhang, W. Shen. Research on CrN-based Ternary Films Deposited by magnetron sputtering, Advanced Materials Research 557 (2012) 1650-1653.
[29] P. Hones, R. Sanjinés, F. Lévy, O. Shojaei. Electronic structure and mechanical properties of resistant coatings: The chromium molybdenum nitride system, Journal of Vacuum Science & Technology A 17 (1999) 1024-1030.
[30] F. Lévy, P. Hones, P. Schmid, R. Sanjinés, M. Diserens, C. Wiemer. Electronic states and mechanical properties in transition metal nitrides, Surface and Coatings Technology 120 (1999) 284-290.
[31] J.A. Thornton. Influence of substrate temperature and deposition rate on structure of thick sputtered Cu coatings, Journal of Vacuum Science and Technology 12 (1975) 830-835.
[32] Y. Zhang, H.J. Whitlow, T. Winzell, I.F. Bubb, T. Sajavaara, K. Arstila, J. Keinonen. Detection efficiency of time-of-flight energy elastic recoil detection analysis systems, Nuclear Instruments and Methods in Physics Research Section B: Beam Interactions with Materials and Atoms 149 (1999) 477-489.
[33] W.C. Oliver, G.M. Pharr. An improved technique for determining hardness and elastic modulus using load and displacement sensing indentation experiments, Journal of materials research 7 (1992) 1564-1583.
[34] A.C. Fischer-Cripps. Critical review of analysis and interpretation of nanoindentation test data, Surface and Coatings Technology 200 (2006) 4153-4165.
[35] A.C. Fischer-Cripps. Nanoindentation, Springer, 2011.
[36] W.D. Nix. Mechanical properties of thin films, Metallurgical transactions A 20 (1989) 2217-2245.
[37] S. Schiller, U. Heisig, G. Beister, K. Steinfelder, J. Strümpfel, C. Korndörfer, W. Sieber. Deposition of hard wear-resistant coatings by reactive D.C. Plasmatron sputtering, Thin Solid Films 118 (1984) 255-270.
[38] A. Hmiel. Partial pressure control of reactively sputtered titanium nitride, Journal of Vacuum Science & Technology A 3 (1985) 592-595.
[39] P.H. Mayrhofer, G. Tischler, C. Mitterer. Microstructure and mechanical/thermal properties of Cr–N coatings deposited by reactive unbalanced magnetron sputtering, Surface and Coatings Technology 142 (2001) 78-84.
[40] P. Ettmayer. Das System Molybdän-Stickstoff, Monatshefte für Chemie/Chemical Monthly 101 (1970) 127-140.
[41] L. Raumann, D. Music, J.M. Schneider. Origin of the nitrogen over-and understoichiometry in $Ti_{0.5}Al_{0.5}N$ thin films, Journal of Physics: Condensed Matter 24 (2012) 155401.
[42] D. Holec, L. Zhou, Z. Zhang, P.H. Mayrhofer. Impact of point defects on the electronic structure of paramagnetic CrN, arXiv preprint arXiv:1410.0758 (2014).
[43] C. Quintela, B. Rodríguez-González, F. Rivadulla. Thermoelectric properties of heavy-element doped CrN, Applied Physics Letters 104 (2014) 022103.
[44] A. Leyland, A. Matthews. On the significance of the H/E ratio in wear control: a nanocomposite coating approach to optimised tribological behaviour, Wear 246 (2000) 1-11.

5.3. Computational and experimental studies on structure and mechanical properties of Mo–Al–N

Abstract

Ab initio calculations show that with increasing N-vacancy content of $Mo_{1-x}Al_xN_y$ solid solutions, the cubic structure is increasingly preferred over the wurtzite-type hexagonal structure. While $Mo_{1-x}Al_xN$ solid solutions, without N-vacancies, energetically favor the wurtzite-type structure over the whole composition range, $Mo_{1-x}Al_xN_{0.5(1+x)}$ and $Mo_{1-x}Al_xN_{0.5}$ solid solutions energetically prefer the cubic structure up to ~45 and 65 at.% Al at the metal sublattice.

Detailed *ab initio* calculations in combination with detailed elemental and phase composition analyses and nanoindentation experiments of reactively sputtered $Mo_{1-x}Al_xN_y$ coatings prove the formation of face-centered cubic structures for Al-contents $x \leq 0.57$. These $Mo_{1-x}Al_xN_y$ coatings exhibit an Al-dependent population of the nitrogen sublattice, following the $MoN_{0.5}$–AlN quasi-binary tie line. For Al-contents $x \geq 0.79$ the coatings crystallize in the wurtzite-type hexagonal phase, while in the intermediate composition range both phases, cubic and wurtzite-type hexagonal, coexist. As long as the cubic structure is maintained, the hardness increases from ~33.0 to 38.4 GPa with increasing Al-content, but drops to ~22 GPa for $x \geq 0.67$, when the films contain hexagonal wurtzite-type phases.

Keywords

Mo–Al–N; hard coatings; *ab initio*; nitrogen vacancies; mechanical properties

I. Introduction

Face-centered cubic-structured γ-Mo_2N (B1, NaCl-type with half-populated N-sublattice, hence, actually $MoN_{0.5}$ [1]) exhibits excellent mechanical and tribological properties [2] and is therefore an ideal candidate for wear-resistant coatings. The major limitation of Mo–N coatings is their low resistance against oxidation, resulting in the formation of molybdenum oxides having a high vapour pressure [3]. To overcome these limitations, we have developed Mo–Al–N coatings, since Al typically increases the oxidation resistance of transition metal (TM) nitrides by forming dense oxides. Moreover, an increasing Al-content is known to improve the tribological and mechanical properties of TM nitrides by solid solution strengthening and age hardening [4-9]. Although the binary phases γ-Mo_2N and hexagonal-structured (ZnS wurtzite-type) w-AlN are not miscible in thermodynamic equilibrium, $Mo_{1-x}Al_xN$ solid solutions can be prepared by physical vapour deposition. Since the face-centered cubic-structured (c-) modification of AlN is a highly unstable high-pressure allotrope of the thermodynamically stable w-AlN structure [10], we expect the Al-content to play a crucial role in the formation of cubic-structured c-$Mo_{1-x}Al_xN_y$ and wurtzite-type w-$Mo_{1-x}Al_xN_y$ phases, similar to the cases of $Ti_{1-x}Al_xN$ [11-13] and $Cr_{1-x}Al_xN$ [13-15].

There is only a limited number of studies on coatings within the Mo–Al–N system and the reported maximum Al-content, x = Al/(Mo+Al), achieved within single-phased c-$Mo_{1-x}Al_xN_y$ coatings is x ~0.3 [16-18]. Two recent publications even present deteriorating mechanical properties with increasing Al-content [17, 18]. This rather unusual behavior and the limited information about sputtered Mo–Al–N coatings available, motivated us for a detailed study of this material system.

By combining *ab initio* and experimental studies of $Mo_{1-x}Al_xN_y$ we show that the metal sublattice population as well as the nitrogen sublattice population is crucial for the formation of face-centered cubic-structured solid solutions. Our experimental investigations clearly evidence that sputter-deposited $Mo_{1-x}Al_xN_y$ coatings with a face-centered cubic structure and chemical compositions close to the $MoN_{0.5}$–AlN quasi-binary tie line exhibit strongly improved mechanical properties with increasing aluminium content.

II. Computational and experimental details

The respective energetic stability of face-centered cubic (c-) and hexagonal wurtzite-type (w-) solid solutions along the three quasi-binary tie lines, MoN–AlN, $MoN_{0.5}$–AlN, and $MoN_{0.5}$–$AlN_{0.5}$, was calculated using density functional theory (DFT) as implemented in the Vienna Ab initio Simulation Package (VASP) [19, 20].

The energy of formation, E_f, was determined with respect to the elemental constituents, fcc-Al, bcc-Mo and molecular nitrogen, applying the following Eq. (1) [21]:

$$E_f = \frac{1}{\sum_i n_i}(E_{tot} - \sum_i n_i E_i) \quad (1)$$

Here E_{tot} and E_i are the total energy of the compound and its elemental constituents, respectively, as determined from DFT, while n_i denotes the number of atoms of species i. For a stability comparison between different structure types the configurational entropy can be neglected, since at a given concentration the configurational entropy is the same and independent of the structure type. Supercells with different chemical compositions were constructed using the special quasi-random structure (SQS) approach [22]. The high cooling rates in PVD and the fact that no heat treatment was applied, in combination with the absence of super-structure reflections in our XRD data, make ordering rather unlikely. Therefore, ordering tendencies were not investigated in our simulations. Wurtzite-type phases were studied with 2x2x4 supercells using a 6x6x4 kpoint mesh. The cubic phases were investigated with a 2x2x1 supercell (along the MoN–AlN and $MoN_{0.5}$–AlN tie lines) and 2x2x2 supercells (along the $MoN_{0.5}$–$AlN_{0.5}$ tie line) using 4x4x8 and 4x4x4 kpoint meshes, respectively. All computations were performed with the projector augmented wave method and the generalized gradient approximation (PAW-GGA) using an energy cutoff of 700 eV. Together with the chosen kpoint mesh, these settings guaranteed for an accuracy of a few meV/atom.

A modified Leybold Heraeus magnetron sputtering system Z400 was used to deposit Mo–Al–N thin films in Ar and N_2 atmosphere (purity above 99.999% for both gases). Mo-rich Mo–Al–N thin films were synthesised from a molybdenum target (99.97% purity, Ø75 mm) by covering the race track with different numbers of small Al-cubes (99.85 % purity, 3 × 3 × 3 mm^3). Al-rich Mo–Al–N coatings were prepared from an aluminum target (99.5% purity, Ø75 mm), where small Mo-cubes (99.99% purity, 3 × 3 × 3 mm^3) uniformly covered the race track. Primarily to the deposition processes, the chamber was evacuated to a high vacuum of $p_{base} \leq 5 \cdot 10^{-4}$ Pa. The sputter depositions were performed with a constant total pressure, p_T, of 0.35 Pa and a N_2-to-total pressure ratio of p_{N2}/p_T = 0.32, based on our previous study [1]. All depositions were carried out with a target current of 0.4 A DC while keeping the substrates at floating potential (~ -15 V) and at 450±20 °C.

The crystal structures of the as-deposited thin films were analysed by X-ray diffraction (XRD), using a Philips X'Pert diffractometer with monochromatic Cu *Kα* radiation in Bragg Brentano geometry. The stress-free lattice parameters were obtained with the "$\sin^2\psi$" method [23] using a PANalytical Empyrion diffractometer in glancing angle mode with an angle of incidence γ = 2°.

The film growth morphology was investigated by scanning electron microscopy (SEM) of fracture cross-sections. Energy dispersive X-ray spectroscopy (EDS) allowed for a chemical characterization of the thin films. The EDS measurements were calibrated with Mo–N thin film standards that have been characterized by elastic recoil detection analyses [1]. Mechanical properties, such as indentation modulus and hardness were determined by nanoindentation using an ultra-micro indentation system (UMIS) equipped with a Berkovich type indenter. The obtained load-displacement curves were evaluated after Oliver and Pharr [24] as described in detail in Refs. [1] and [25].

III. Results

Figures 1a, b, and c present the energy of formation, E_f, of $Mo_{1-x}Al_xN_y$ with face-centered cubic (red squares) and wurtzite-type (green hexagons) crystal structures along the three quasi-binary tie lines, MoN–AlN, $MoN_{0.5}$–AlN, and $MoN_{0.5}$–$AlN_{0.5}$, respectively. Solid solutions along the MoN–AlN quasi-binary tie line, hence, with fully occupied N-sublattices, energetically prefer the wurtzite-type structure, w-$Mo_{1-x}Al_xN$, over the whole composition range, see Fig. 1a. Solid solutions along the $MoN_{0.5}$–AlN tie line exhibit a crossover between cubic- and wurtzite-type $Mo_{1-x}Al_xN_{0.5(1+x)}$ at Al-contents of x ~0.45 (see Fig. 1b), where lower Al-contents favor the cubic structure. Compositions along the $MoN_{0.5}$–$AlN_{0.5}$ tie line, hence, with half-occupied N-sublattices over the whole composition range, provide a crossover between cubic-structured and wurtzite-type $Mo_{1-x}Al_xN_{0.5}$ at x ~0.65.

The energies of formation for the cubic and wurtzite-type solid solutions $Mo_{1-x}Al_xN$, $Mo_{1-x}Al_xN_{0.5(1+x)}$, and $Mo_{1-x}Al_xN_{0.5}$, are very similar over a wide concentration range. These x-regions (with ≤ 50 meV/at differences between the polynomial fits to the cubic and wurtzite-type data

points) are 0.3–0.75 for $Mo_{1-x}Al_xN$, 0.3–0.6 for $Mo_{1-x}Al_xN_{0.5(1+x)}$, and 0.55–0.8 for $Mo_{1-x}Al_xN_{0.5}$, see the vertical dashed lines within Figs. 1a, b, and c, respectively, Consequently, within these Al-contents, the preference for cubic or wurtzite-type phases is very sensitive to small changes in structure and atomic arrangements.

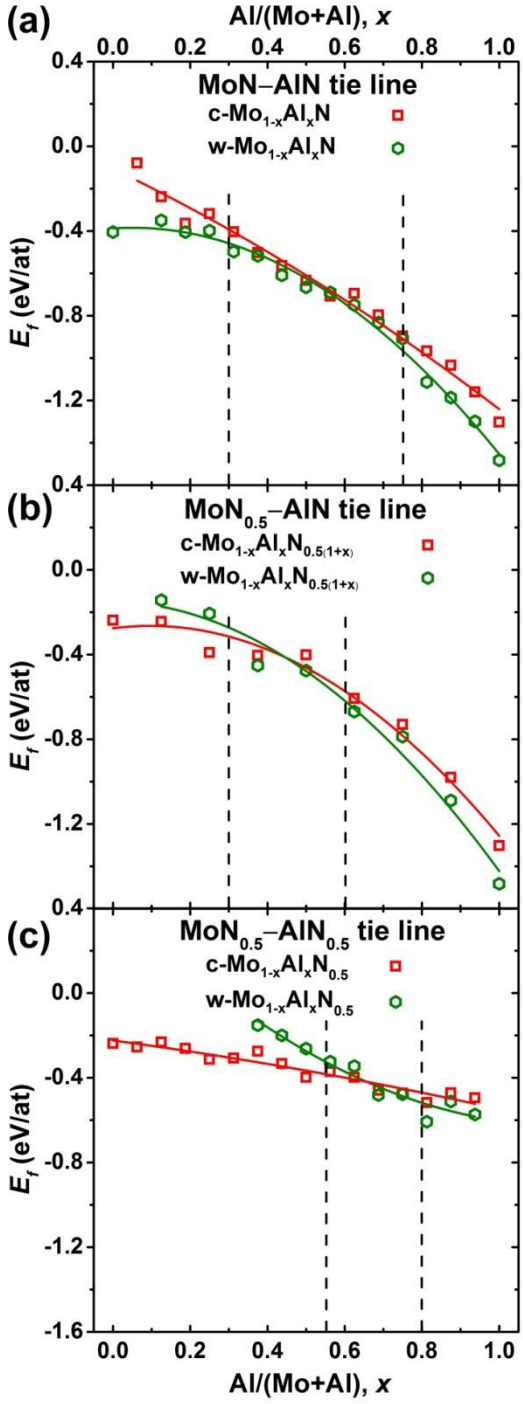

Fig. 1. First principle calculations of the energy of formation, E_f, for cubic and wurtzite-type $Mo_{1-x}Al_xN_y$ along the quasi-binary tie lines MoN–AlN (a), $MoN_{0.5}$–AlN (b), and $MoN_{0.5}$–$AlN_{0.5}$ (c). Red squares and green hexagons represent E_f of cubic and wurtzite-type structures, respectively. The colored solid lines represent second order polynomial fits of the individual data points. The vertical, dashed lines indicate the regions with ≤ 50 meV/at differences between these fits for cubic and wurtzite-type phases.

Our *ab initio* data clearly suggest increasing Al-solubility of the cubic phase with increasing N-vacancy content, Figs. 1a, b, and c, respectively. Therefore, we have selected the relatively low N_2-to-total pressure ratio of 0.32 during sputtering of our $Mo_{1-x}Al_xN_y$ coatings, which guaranties the formation of single-phase cubic-structured $MoN_{0.5}$ [1]. For lower nitrogen partial pressures, the Mo–N coatings also contain metallic Mo-based phases and for higher nitrogen partial pressures, the N-vacancy concentration decreases.

The nitrogen content of our sputtered $Mo_{1-x}Al_xN_y$ coatings increases nearly linearly from 35 to 49 at.% with increasing Al-content x from 0 to 0.79, following the $MoN_{0.5}$–AlN quasi-binary tie line, see Fig. 2. Thus, the relationship between y and x can be described with $y = 0.5(1+x)$ and $Mo_{1-x}Al_xN_{0.5(1+x)}$ solid solutions are formed, corresponding to the results obtained for $Mo_{1-x}Cr_xN_{0.5(1+x)}$ [1]. This chemical variation suggests that the theoretical vacancy content of the nitrogen sublattice continuously decreases from 50% ($MoN_{0.5}$) to 0% (AlN) when Al substitutes for Mo.

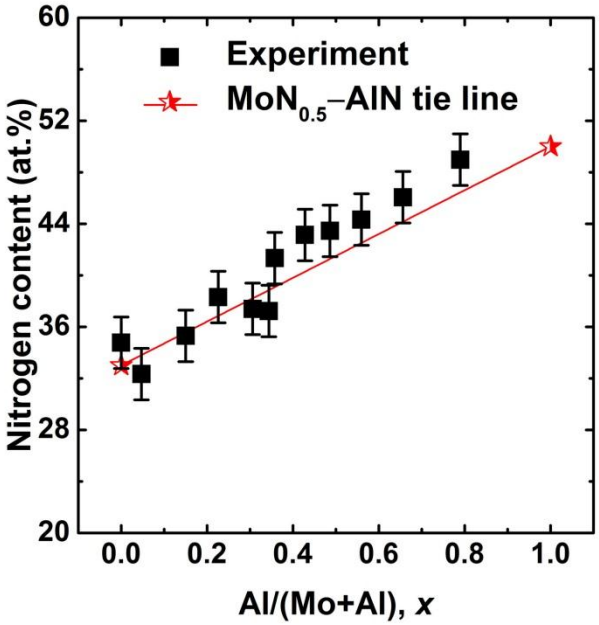

Fig. 2. Nitrogen content of our sputtered $Mo_{1-x}Al_xN_y$ coatings as a function of their Al-content, x.

XRD analyses prove that our $Mo_{1-x}Al_xN_y$ coatings crystallize in a face-centered cubic structure with preferred (200)-orientation for Al/(Mo+Al)-ratios up to ~0.57, see Fig. 3a. Higher aluminium contents energetically prefer the formation of wurtzite-type $Mo_{1-x}Al_xN_y$ solid solutions. Both phases, cubic and wurtzite-type $Mo_{1-x}Al_xN_y$ coexist with x between 0.67 and 0.79, and the coating is predominantly wurtzite-type structured (with traces of the cubic phase) for $x = 1$. Figure 3b is the corresponding color-coded XRD intensity map, based on our 13 different $Mo_{1-x}Al_xN_y$ coatings. This graphical representation is obtained by using a linear interpolation scheme between the experimentally obtained XRD patterns.

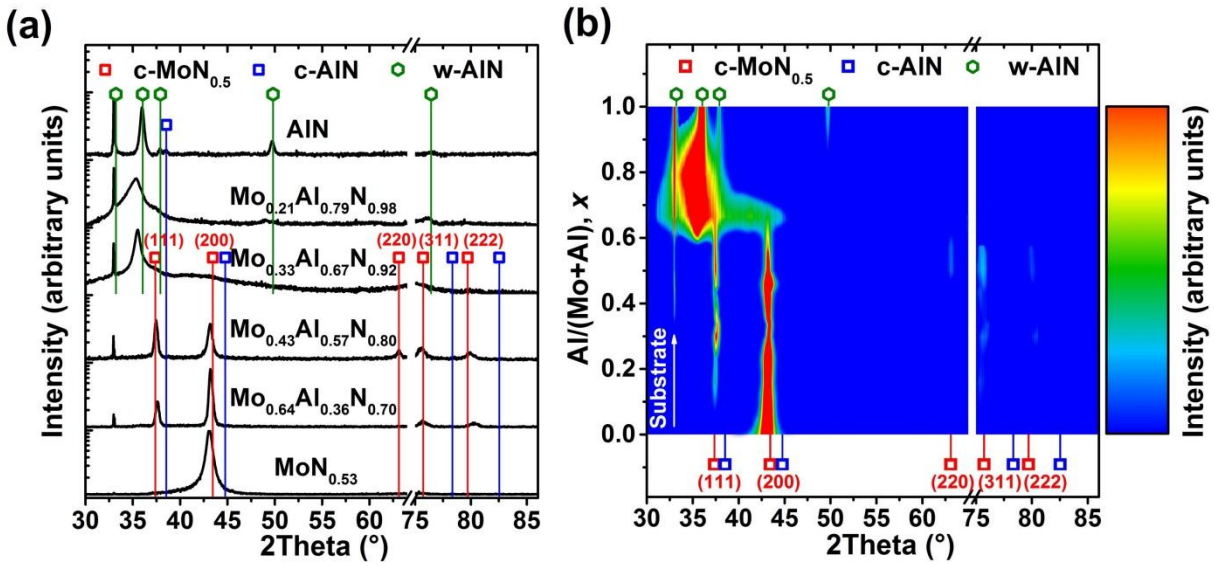

Fig. 3. The logarithmic-scaled XRD patterns of significant $Mo_{1-x}Al_xN_y$ coatings (a) and color-coded XRD intensities of all $Mo_{1-x}Al_xN_y$ coatings (b) with indicated peak positions for c-$MoN_{0.5}$ (ICDD 00-025-1366), c-AlN (ICDD 00-046-1200), and w-AlN (ICDD 00-025-1133). The narrow reflex at $2\theta \approx 33°$ corresponds to the Si-substrate (the second order diffraction).

The stress-free lattice parameters of the experimentally obtained single-phased cubic-structured $Mo_{1-x}Al_xN_y$ coatings only slightly decrease from 4.18±0.02 to 4.16±0.02 Å with increasing Al-content x from 0 to 0.57, see Fig. 4. The comparison with the *ab initio* obtained averaged lattice parameters of face-centered cubic solid solutions along the three quasi-binary tie lines, MoN–AlN (1), $MoN_{0.5}$–AlN (2), and $MoN_{0.5}$–$AlN_{0.5}$ (3), shows an almost identical behavior with $MoN_{0.5}$–AlN (2) quasi-binary tie line. This suggests again (in addition to EDS analyses, Fig. 2) that c-$Mo_{1-x}Al_xN_{0.5(1+x)}$ solid solutions are formed. Only these c-$Mo_{1-x}Al_xN_{0.5(1+x)}$ structures (along the $MoN_{0.5}$–AlN (2) quasi-binary tie line) provide lattice parameters with only a small dependence on the Al-content, comparable to the experimental data. This nearly unaltered lattice parameter, despite the replacement of large Mo atoms by small Al atoms, results from the counter-balance by additional nitrogen atoms. In contrast, the calculated lattice parameters for the vacancy-free c-$Mo_{1-x}Al_xN$ solid solutions (along the MoN–AlN (1) quasi-binary tie line), as one might expect, decrease continuously with increasing Al-concentration, but also do not obey the linear Vegard's rule.

SEM investigations of fracture cross-sections of our coatings, Fig. 5, clearly show dense columnar growth morphologies, especially for the single-phased c-$Mo_{1-x}Al_xN_{0.5(1+x)}$ coatings with $x \leq 0.57$. The column boundaries are less defined for coatings with x between 0.57 and 0.79, containing cubic and wurtzite-type phases as presented above, see Fig. 3. The single-phase wurtzite-type structured coatings, with $x = 0.79$ and 1, exhibit a fine fibrous growth morphology and strongly reduced coating thicknesses due to the pronounced reduction in deposition rate with increasing Al-content. The deposition rate estimated from the cross-section images is with about 1.25 nm/s (for Al-contents x below 0.25) relatively high, but significantly decreases to ~0.2 nm/s (for w-AlN with traces of the cubic phase) with increasing x, see Fig. 6. The reduction in deposition rate with increasing Al-content is mainly based on the increasing poisoning effect

of the target material, because AlN has a significantly lower conductivity as the Mo–N phases formed at the target surface.

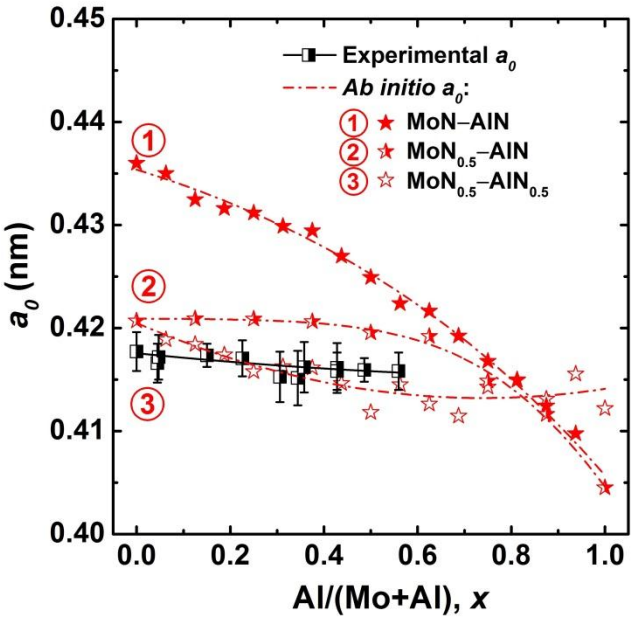

Fig. 4. Stress-free lattice parameters, a_0, of single-phased cubic-structured c-$Mo_{1-x}Al_xN_y$ coatings and cubic-structured solid solutions, $Mo_{1-x}Al_xN$, $Mo_{1-x}Al_xN_{0.5(1+x)}$, and $Mo_{1-x}Al_xN_{0.5}$, along the MoN–AlN (1), $MoN_{0.5}$–AlN (2), and $MoN_{0.5}$–$AlN_{0.5}$ (3) quasi-binary tie lines, respectively.

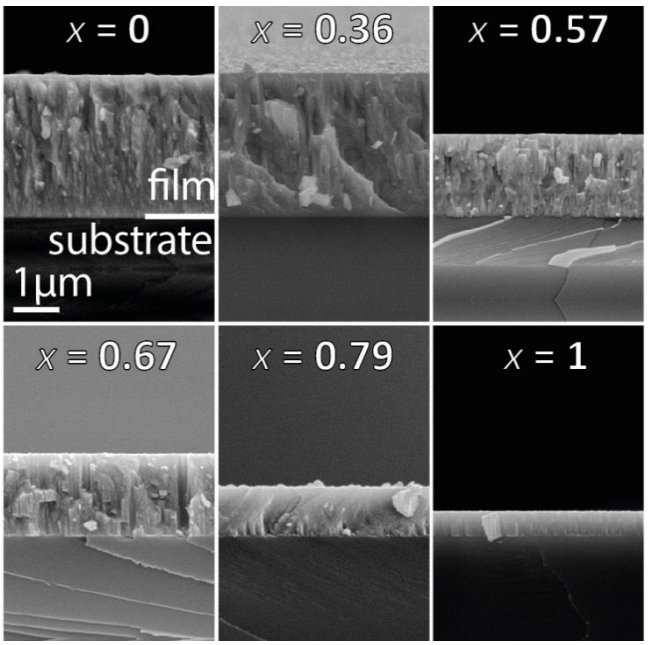

Fig. 5. SEM fracture cross-sections of significant $Mo_{1-x}Al_xN_y$ coatings with Al/(Mo+Al)-ratios, x, at the borders of the cubic (x = 0 and 0.57) and within the cubic phase region (x = 0.36) as well as $Mo_{1-x}Al_xN_y$ coatings, containing wurtzite-type phases (x = 0.67, 0.79 and 1).

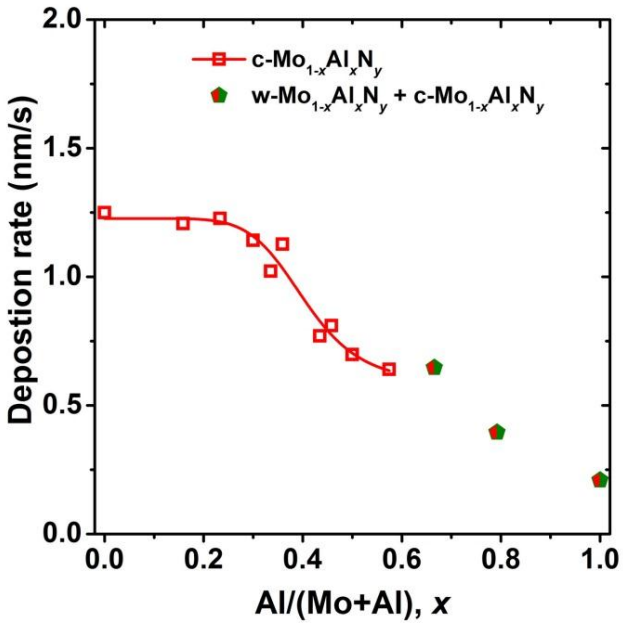

Fig. 6. Deposition rate of our $Mo_{1-x}Al_xN_y$ coatings as a function of their Al-content, *x*.

The nanoindentation hardnesses, *H*, of our face-centered cubic c-$Mo_{1-x}Al_xN_{0.5(1+x)}$ coatings increases from ~33 to 38 GPa with increasing Al-content, see Fig. 7. The highest hardness (38.3±1.7 GPa) of all coatings studied is obtained for c-$Mo_{0.43}Al_{0.57}N_{0.80}$ – the single-phase cubic-structured coating with the highest Al-content. The hardnesses of the coatings containing hexagonal wurtzite-type phases are between 22 and 25 GPa.

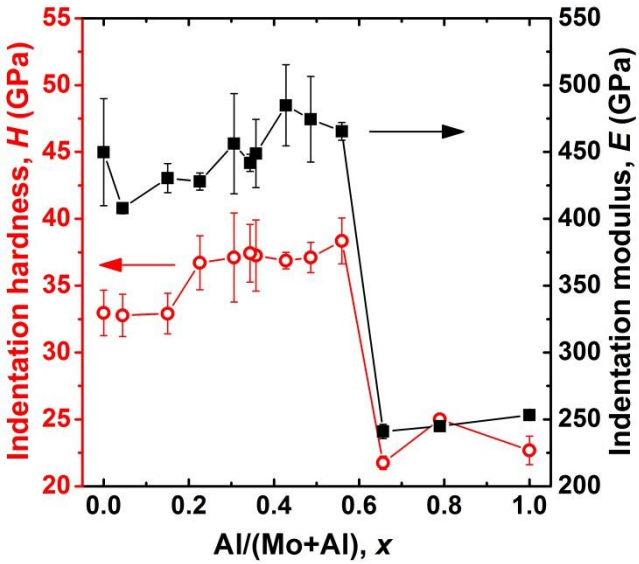

Fig. 7. Indentation hardness, *H*, (left axis, red open circles) and indentation modulus, *E*, (right axis, black solid squares) of our $Mo_{1-x}Al_xN_y$ coatings as a function of their Al-content, *x*.

The indentation moduli of our single-phase cubic-structured coatings are between 410 and 480 GPa, but decrease to ~245 GPa for coatings containing hexagonal wurtzite-type phases Hence, their dependence on composition and crystal structure is very similar to the hardness evolution.

IV. Discussion

Chemical analyses of our sputtered $Mo_{1-x}Al_xN_y$ coatings (Fig. 2) in combination with their structural investigations (Figs. 3a and b) suggest that cubic-structured $Mo_{1-x}Al_xN_y$ solid solutions are formed for Al-contents $x \leq 0.57$. Whereas $Mo_{0.43}Al_{0.57}N_{0.80}$ is still single-phase cubic-structured, $Mo_{0.33}Al_{0.67}N_{0.92}$ already contains wurtzite-type phases, and $Mo_{0.21}Al_{0.79}N_{0.98}$ is already single-phase wurtzite-type structured, compare Figs. 3a and b. With increasing Al-content, x, the N-content, y, also increases with a close to linear dependence following $y = 0.5(1+x)$. Thus, the chemical composition of the solid solutions is best described by c-$Mo_{1-x}Al_xN_{0.5(1+x)}$, i.e. along the $MoN_{0.5}$–AlN quasi-binary tie line. The N-sublattice of their NaCl-type cubic structure is only half-populated for $MoN_{0.5}$ (hence, 50% of the N-sites are vacant), but fully populated for AlN. Consequently, the substitution of Mo by Al leads to a reduction in N-vacancies.

In excellent agreement with these chemical results, also the stress-free lattice parameters of our cubic-structured coatings can best be described by *ab initio* calculations along the $MoN_{0.5}$–AlN quasi-binary tie line, Fig. 4. The small but nearly constant overestimation of ~0.7% by *ab initio* is a well-known shortcoming of GGA [26]. The experimental and computational lattice parameters of c-$Mo_{1-x}Al_xN_{0.5(1+x)}$ only slightly decrease with increasing Al-content, because simultaneously also the vacant N-sites are filled. Contrary, the *ab initio* obtained lattice parameters of c-$Mo_{1-x}Al_xN_{0.5}$ and especially c-$Mo_{1-x}Al_xN$ solid solutions significantly decrease with increasing Al-content, because, their N-sublattice is unchanged when Al substitutes for Mo.

The maximum Al-content of $x = 0.57$, within our single-phase cubic-structured $Mo_{1-x}Al_xN_y$ coatings, excellently agrees with *ab initio* calculations of $Mo_{1-x}Al_xN_{0.5(1+x)}$ solid solutions. The latter exhibit Al-dependent N-vacancies along the $MoN_{0.5}$–AlN quasi-binary tie line, and energetically prefer the cubic structure for $x \leq 0.45$. Furthermore, the wurtzite-type phase is energetically preferred by only ≤ 50 meV/at for x between 0.45 and 0.6. $Mo_{1-x}Al_xN_{0.5}$ solid solutions, with constantly 50% vacant N-sites, favor the cubic structure up to even ~0.65. $Mo_{1-x}Al_xN$ solid solutions (with a fully populated N-sublattice), on the other hand, prefer the wurtzite-type structure across the whole composition range. These results suggest that N-vacancies support the formation of the cubic structure and allow for increased Al-contents within energetically preferred cubic-structured solid solutions.

The importance to stabilize the cubic structure within our $Mo_{1-x}Al_xN_y$ coatings up to high Al-contents is well represented by their mechanical properties, see Fig. 7. The hardness of single-phase cubic-structured $Mo_{1-x}Al_xN_{0.5(1+x)}$ coatings is always above 33 GPa and increases from 33.0±1.7 GPa (for c-$MoN_{0.53}$) to 38.3±1.7 GPa (for c-$Mo_{0.43}Al_{0.57}N_{0.80}$) with increasing Al-content. As soon as wurtzite-type $Mo_{1-x}Al_xN_y$ phases are formed, the hardness drops to only ~22 GPa.

Our *ab initio* and experimental studies suggest, that the high nitrogen partial pressure used during deposition of $Mo_{1-x}Al_xN_y$ thin films, as reported in [17, 18], is responsible for the observed maximum Al/(Mo+Al)-ratio of ~0.3 within cubic-structured coatings and the general hardness-decrease with increasing Al-content. Considering the additional chemical potential of

nitrogen, a high nitrogen pressure within the deposition chamber favors the formation of a fully occupied N-sublattice, hence, $Mo_{1-x}Al_xN$ solid solutions. Contrary, a nitrogen-deficient atmosphere supports the formation of N-vacancies, hence, $Mo_{1-x}Al_xN_{0.5(1+x)}$ and $Mo_{1-x}Al_xN_{0.5}$ solid solutions. Thus, a low nitrogen partial pressure allows to increase the maximum Al-content within the cubic structure, cf. Fig.1.

V. Summary and conclusions

Ab initio calculations of solid solutions along the three quasi-binary tie lines, MoN–AlN, $MoN_{0.5}$–AlN, and $MoN_{0.5}$–$AlN_{0.5}$, clearly show that the chemical stability range of the cubic structure increases (on the expanse of wurtzite-type structure) when N-vacancies are present. Whereas for $Mo_{1-x}Al_xN$ solid solutions (theoretically having no N-vacancies) the wurtzite-type structure is preferred across the entire composition range, cubic-structured c-$Mo_{1-x}Al_xN_{0.5(1+x)}$ and c-$Mo_{1-x}Al_xN_{0.5}$ solid solutions are energetically favorable even up to significantly increased Al-concentrations. Based on these results, we have chosen a low N_2-to-total pressure ratio $p_{N2}/p_T = 0.32$ for the preparation of $Mo_{1-x}Al_xN_y$ coatings. This allows the development of single-phase cubic-structured c-$Mo_{1-x}Al_xN_y$ solid solutions up to Al-contents of x ~0.57, currently the highest value reported for c-$Mo_{1-x}Al_xN_y$. With higher Al-contents, also wurtzite-type phases are formed and for $x \geq 0.79$ the coatings predominantly crystallize within the wurtzite-type structure.

Combined with structural investigations, detailed chemical studies show that the N-content, y, of our c-$Mo_{1-x}Al_xN_y$ solid solutions continuously increases from ~0.53 to 0.80 with increasing Al-content from x = 0 to ~0.57. Consequently, their chemical composition follows the $MoN_{0.5}$–AlN quasi-binary tie line, and can thus best be described as $Mo_{1-x}Al_xN_{0.5(1+x)}$, indicating that the ~50% nitrogen vacancies present in $MoN_{0.5}$ are filled (with N) when Al substitutes for Mo.

Ab initio calculations highlight that with increasing vacancy content at the nitrogen sublattice the transition from c-$Mo_{1-x}Al_xN_y$ to w-$Mo_{1-x}Al_xN_y$ shifts to higher Al-contents. The importance of maintaining the cubic structure within this material system is well represented by the hardness of our films. With increasing Al-content, the hardness increases from ~33 GPa (for c-$MoN_{0.53}$) to 38 GPa (for c-$Mo_{0.43}Al_{0.57}N_{0.80}$) as long as the coatings are single-phase cubic-structured, but drops to ~22 GPa for phase wurtzite-type structured the coatings with higher Al-contents, containing hexagonal wurtzite-type phases.

Based on our detailed *ab initio* calculations in combination with experimental studies we can conclude that nitrogen vacancies (or vacancies in general) have a significant and determining role for the stabilization of various phases. Within the Mo–Al–N material system, nitrogen vacancies are essential to stabilize the cubic structure up to very high Al-contents, which are necessary pre-requisites for high thermal stability and strength.

Acknowledgements

The financial support by the START Program (Y371) of the Austrian Science Fund (FWF) is gratefully acknowledged. The authors are thankful to the XRC, USTEM, and VSC of the TU Wien.

References

[1] F.F. Klimashin, H. Riedl, D. Primetzhofer, J. Paulitsch, P.H. Mayrhofer. Composition driven phase evolution and mechanical properties of Mo–Cr–N hard coatings, Journal of Applied Physics 118 (2015) 025305.

[2] M. Ürgen, O. Eryilmaz, A. Cakir, E. Kayali, B. Nilüfer, Y. Işik. Characterization of molybdenum nitride coatings produced by arc-PVD technique, Surface and Coatings Technology 94 (1997) 501-506.

[3] G. Gassner, P.H. Mayrhofer, K. Kutschej, C. Mitterer, M. Kathrein. Magnéli phase formation of PVD Mo–N and W–N coatings, Surface and Coatings Technology 201 (2006) 3335-3341.

[4] P.H. Mayrhofer, A. Hörling, L. Karlsson, J. Sjölén, T. Larsson, C. Mitterer, L. Hultman. Self-organized nanostructures in the Ti-Al-N system, Applied Physics Letters 83 (2003) 2049-2051.

[5] C. Wüstefeld, D. Rafaja, V. Klemm, C. Michotte, M. Kathrein. Effect of the aluminium content and the bias voltage on the microstructure formation in $Ti_{1-x}Al_xN$ protective coatings grown by cathodic arc evaporation, Surface and Coatings Technology 205 (2010) 1345-1349.

[6] D. McIntyre, J. Greene, G. Håkansson, J.E. Sundgren, W.D. Münz. Oxidation of metastable single-phase polycrystalline $Ti_{0.5}Al_{0.5}N$ films: Kinetics and mechanisms, Journal of Applied Physics 67 (1990) 1542-1553.

[7] V. Anikin, I. Blinkov, A. Volkhonskii, N. Sobolev, S. Tsareva, R. Kratokhvil, A. Frolov. Ion-plasma Ti-Al-N coatings on a cutting hard-alloy tool operating under conditions of constant and alternating-sign loads, Russian Journal of Non-Ferrous Metals 50 (2009) 424-431.

[8] H. Willmann, P. Mayrhofer, P.Å. Persson, A. Reiter, L. Hultman, C. Mitterer. Thermal stability of Al–Cr–N hard coatings, Scripta Materialia 54 (2006) 1847-1851.

[9] K. Bobzin, E. Lugscheider, R. Nickel, N. Bagcivan, A. Krämer. Wear behavior of $Cr_{1-x}Al_xN$ PVD-coatings in dry running conditions, Wear 263 (2007) 1274-1280.

[10] Q. Xia, H. Xia, A.L. Ruoff. Pressure-induced rocksalt phase of aluminum nitride: A metastable structure at ambient condition, Journal of Applied Physics 73 (1993) 8198-8200.

[11] S. PalDey, S. Deevi. Single layer and multilayer wear resistant coatings of (Ti, Al) N: a review, Materials Science and Engineering: A 342 (2003) 58-79.

[12] P. Mayrhofer, D. Music, J. Schneider. Ab initio calculated binodal and spinodal of cubic $Ti_{1-x}Al_xN$, Applied Physics Letters 88 (2006) 071922.

[13] D. Holec, F. Rovere, P.H. Mayrhofer, P.B. Barna. Pressure-dependent stability of cubic and wurtzite phases within the TiN–AlN and CrN–AlN systems, Scripta Materialia 62 (2010) 349-352.

[14] A. Sugishima, H. Kajioka, Y. Makino. Phase transition of pseudobinary Cr–Al–N films deposited by magnetron sputtering method, Surface and Coatings Technology 97 (1997) 590-594.

[15] P.H. Mayrhofer, D. Music, T. Reeswinkel, H.G. Fuß, J.M. Schneider. Structure, elastic properties and phase stability of $Cr_{1-x}Al_xN$, Acta Materialia 56 (2008) 2469-2475.

[16] J. Šůna, J. Musil, P. Dohnal. Control of macrostress σ in reactively sputtered Mo–Al–N films by total gas pressure, Vacuum 80 (2006) 588-592.

[17] J. Yang, Z. Yuan, Q. Liu, X. Wang, Q. Fang. Characterization of Mo–Al–N nanocrystalline films synthesized by reactive magnetron sputtering, Materials Research Bulletin 44 (2009) 86-90.

[18] J. Xu, H. Ju, L. Yu. Microstructure, oxidation resistance, mechanical and tribological properties of Mo–Al–N films by reactive magnetron sputtering, Vacuum 103 (2014) 21-27.

[19] G. Kresse, J. Furthmüller. Efficient iterative schemes for ab initio total-energy calculations using a plane-wave basis set, Physical Review B 54 (1996) 11169.

[20] G. Kresse, J. Hafner. Ab initio molecular dynamics for liquid metals, Physical Review B 47 (1993) 558.

[21] H. Euchner, P. Mayrhofer. Vacancy-dependent stability of cubic and wurtzite $Ti_{1-x}Al_xN$, Surface and Coatings Technology (2015).
[22] A. Van de Walle, P. Tiwary, M. De Jong, D. Olmsted, M. Asta, A. Dick, D. Shin, Y. Wang, L.-Q. Chen, Z.-K. Liu. Efficient stochastic generation of special quasirandom structures, Calphad 42 (2013) 13-18.
[23] D. Rafaja, C. Wüstefeld, C. Baehtz, V. Klemm, M. Dopita, M. Motylenko, C. Michotte, M. Kathrein. Effect of internal interfaces on hardness and thermal stability of nanocrystalline $Ti_{0.5}Al_{0.5}N$ coatings, Metallurgical and Materials Transactions A 42 (2011) 559-569.
[24] W.C. Oliver, G.M. Pharr. An improved technique for determining hardness and elastic modulus using load and displacement sensing indentation experiments, Journal of materials research 7 (1992) 1564-1583.
[25] A.C. Fischer-Cripps. Critical review of analysis and interpretation of nanoindentation test data, Surface and Coatings Technology 200 (2006) 4153-4165.
[26] A. Khein, D.J. Singh, C.J. Umrigar. All-electron study of gradient corrections to the local-density functional in metallic systems, Physical Review B 51 (1995) 4105.

5.4. *Ab initio*-guided development of super-hard Mo–Al–Cr–N coatings

Abstract

The *ab initio*-guided adjustment in N_2-partial pressure during reactive magnetron sputtering allowed the preparation of single-phase cubic-structured $Mo_{1-x-y}Al_xCr_yN_z$ coatings with Al-contents up to even x~0.6. Combining with low Cr-concentrations, aluminium enrichment was found to significantly enhance the material strength. The highest hardness *H* of 41.2 ± 2.9 GPa in combination with low indentation modulus *E* of 440 ± 15 GPa GPa is obtained for $Mo_{0.39}Al_{0.52}Cr_{0.09}N_{0.98}$, possessing also the highest H/E- and H^3/E^2-ratios of 0.1 and 0.36, respectively. Further Al-enrichment (x >~ 0.6) favours, however, the hexagonal phase formation, leading to a drastic drop of hardness to ~20 GPa. Therefore, the combination of excellent mechanical properties with high Al-content suggests fcc-$Mo_{1-x-y}Al_xCr_yN_z$ exhibits high potential for severe applications.

Keywords

Superhardness, Mo–Al–Cr–N, reactive sputtering, nitrogen vacancies, mechanical properties

I. Introduction

The application area of hard cubic molybdenum nitride, γ-$MoN_{0.5}$, showing also excellent tribological properties due to formation of Magnéli phase, is restricted to the temperatures below 500 °C [1]. At elevated temperatures, the relatively weak bonds between molybdenum and nitrogen – resulting from filling the antibonding electron states [2] – easily lead to loss of nitrogen and pronounced oxidation, where the volatile MoO_3 forms. Improved thermal stability and oxidation resistance is very often obtained by alloying with aluminum and/or chromium. These, easily form very dense protective oxide scales, Al_2O_3, Cr_2O_3 or even mixtures thereof $(Al,Cr)_2O_3$. Synthesis of a single-phased quaternary materials also increases the mixing entropy, leading to high thermal stability as reported for high entropy alloys [3, 4].

Based on previous studies on the binary Mo–N system [5] and its ternaries Mo–Al–N [6] and Mo–Cr–N [7], we developed quaternary Mo–Al–Cr–N coatings with the highest Al content dissolved in a cubic structured Mo–N based phase. The key-parameter for this development is the knowledge-driven incorporation of N-vacancies at the N-sublattice of the NaCl based cubic structure. Thereby, even super-hard coatings could be developed.

II. Experimental details

The quaternary Mo–Al–Cr–N thin films were synthesised using a modified magnetron sputtering system Leybold Heraeus Z400, in mixed Ar and N_2 glow discharges (both gases with purity above 99.999%). Three different powder metallurgically prepared targets (99.95% purity,

Ø75 mm, PLANSEE SE) were used: the two most common Cr/Al-compositions with 40/60 at.%-ratio ($Cr_{0.4}Al_{0.6}$) and 30/70 at.%-ratio ($Cr_{0.3}Al_{0.7}$), and a target with Mo/Al of 40/60 at.%-ratio ($Mo_{0.45}Al_{0.55}$), which was especially developed by PLANSEE SE based on our recent findings [6]. In order to synthesize quaternary nitrides, additional small cubes (4, 8, 12, 16, 20, or 36 pieces with a size of 3x3x3 mm^3) of the alloying elements (either Mo, Cr, or Cr/Al compounds with 15/85 and 40/60 at.%-ratio, all with 99.95% purity) were uniformly arranged on the race track of the targets. All depositions were prepared at a constant 0.4 A target current (DC), floating potential at the substrates (~ -15V), and constant substrate temperature of 450 ± 20 °C. Prior to every deposition process, the chamber was evacuated to a high vacuum of $p_{base} \leq 5 \cdot 10^{-4}$ Pa. During all sputter deposition processes the total pressure, p_T, of 0.35 Pa and N_2-to-total pressure ratio, p_{N2}/p_T, of 0.32 were kept constant. Single-crystal silicon and austenite steel substrates were ultrasonically pre-cleand in acetone and alcohol (for 5 mins) and r.f. plasma etched using following parameters $p_{etching}$(Ar) ≈ 2 Pa, 350 V, 50 kHz, 2656 ns. After each deposition process, the substrates were cooled down to at least 90-100 °C before venting the deposition chamber, in order to minimize the surface chemistry alterations [8].

Phase analysis was carried out by means of X-ray diffractometry (XRD) in Bragg-Brentano geometry using monochromized CuK_α radiation (λ = 1.5418 Å). The stress-free lattice parameters are obtained by applying the "$sin^2\psi$" method [9] combined with glancing angle XRD measurements – angle of incidence γ = 2°. Fracture cross-sections of our thin films deposited on Si-substrates are investigated by scanning electron microscopy (SEM) to study the film growth morphology and deposition rates. The chemical compositions of our coatings are evaluated based on energy dispersive X-ray spectroscopy (EDX, or EDS) and Mo–N thin film standards that have been characterized with elastic recoil detection analyses [7, 10].

Indentation hardness, *H*, and modulus, *E*, of our thin films are obtained by evaluating the load-displacement curves of nanoindentation tests (Berkovich diamond tip and load range of 3 to 30 mN) after the Oliver and Pharr method [11], described in detail in Refs. [7] and [12]. The instrument was calibrated using fused silica with an elastic modulus *E* of 72.5 GPa [13]. To verify the accuracy of the measurements and the indentation equipment, a few reference samples (listed in table 1, see p.24) were tested.

III. Results and discussion

The elemental composition analysis reveals that the coatings contain 5-7 at.% less Al than the target's composition ($Cr_{47}Al_{0.53}$, $Cr_{37}Al_{0.63}$, and $Mo_{0.45}Al_{0.55}$ in the film vs. $Cr_{40}Al_{0.60}$, $Cr_{30}Al_{0.70}$, and $Mo_{40}Al_{0.60}$ in the target, respectively), and is explained by means of the poisoning effect resulting in formation of the non-conductive compounds (apparently aluminium nitride) on the target's surface [14] and partly due to the different sputtering yields (compare that for Cr and Al at ~400-500 eV Ar^+-energy [15]). Please note, in order to simplify the further discussion, hereafter we operate with the closest quasi-binary tie lines and describe the average chemical compositions of our Mo–Al–Cr–N thin films along the quasi-binary sections $Cr_{0.5}Al_{0.5}N$–$MoN_{0.5}$ and $Cr_{0.4}Al_{0.6}N$–$MoN_{0.5}$ when using the $Cr_{0.4}Al_{0.6}$ and $Al_{0.3}Cr_{0.7}$ targets, respectively, with addition

of Mo-cubes, see the corresponding dash-dotted lines in the AlN–$MoN_{0.5}$–CrN ternary phase field, Fig. 1a. The Cr/Al-ratios within the coatings remain almost at ~0.6 and ~0.9, respectively, depending on the target used.

Similar, when using the $Mo_{0.4}Al_{0.6}$ target and putting Cr-cubes at the race track, the composition follows the quasi-binary section $Mo_{0.45}Al_{0.55}N$–CrN, see the corresponding dash-dotted line in Fig. 1a. Again, the Mo/Al-ratio remains nearly at ~0.8.

As expected, when adding cubes of $Cr_{0.15}Al_{0.85}$, or $Cr_{0.4}Al_{0.6}$ at the $Mo_{0.45}Al_{0.55}$ target during deposition addition of these Al-containing cubes results in Al-contents, *x*, above 0.6 for the quaternary $Mo_{1-x-y}Al_xCr_yN_z$ coatings (the quasi-binary sections are not indicated in Fig. 1a).

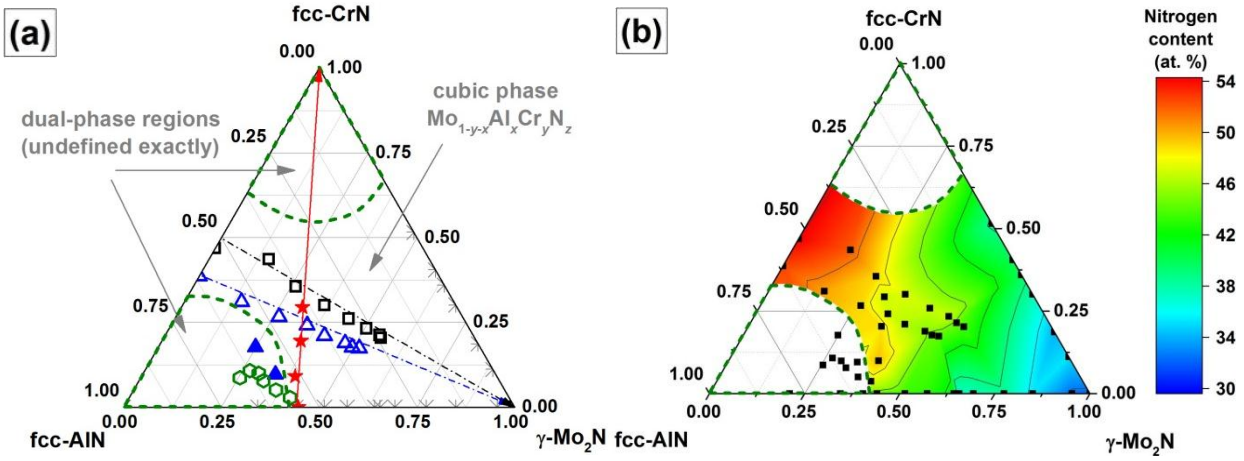

Fig. 1. Development of the elemental composition within the Mo–Al–Cr–N system: metal fraction (a) and nitrogen content (b). Evolution of the elemental metal fraction along the intermetallic tie lines $Cr_{0.5}Al_{0.5}N$–$MoN_{0.5}$ (black line and empty squares), $Cr_{0.4}Al_{0.6}N$–$MoN_{0.5}$ (blue line and empty triangles) $Mo_{0.45}Al_{0.55}N$–CrN (red line and stars), as well as Al-containing cubes $Cr_{0.15}Al_{0.85}$ (green filled hexagons) or $Cr_{0.4}Al_{0.6}$ (blue filled triangles) at the $Mo_{0.45}Al_{0.55}$ target. The grey symbols on the quasi-binary tie lines $MoN_{0.5}$–CrN and $MoN_{0.5}$–AlN represent the results of our recent investigations. The green dotted lines separated the region of single-phased cubic-structured quaternary nitrides from the dual-phased structured coatings with hexagonal structures.

The nitrogen content (Fig.1b) increases nearly linearly from ~35 at.% (for $MoN_{0.53}$) to over 50 at.% (for Cr–Al–N) with decreasing Mo-content. However, coatings produced from the $Mo_{0.4}Al_{0.6}$ target, exhibit a slightly deviation from this tendency, showing a Me:N stoichiometry of nearly 1:1 with ~49-50 at.% nitrogen, especially for low Cr-contents. The nearly linear dependence of increasing N-content and decreasing Mo-content, excellently agrees with our earlier studies on the ternary material systems Mo–Cr–N [7] and Mo–Al–N [6].

Structural investigations reveal a polycrystalline single-phase cubic structure for all coatings prepared from the $Cr_{0.4}Al_{0.6}$ and $Cr_{0.3}Al_{0.7}$ targets with the addition of Mo-cubes – Figs. 2a and b, respectively – as well as for all coatings prepared from the $Mo_{0.4}Al_{0.6}$ target with the addition of Cr-cubes – Fig. 3c. Consequently, single-phase cubic structured $Mo_{1-x-y}Al_xCr_yN_z$ coatings are obtained, as long as their chemical composition follows the three quasi-binary tie lines: $Cr_{0.5}Al_{0.5}N$–$MoN_{0.5}$, $Cr_{0.4}Al_{0.6}N$–$MoN_{0.5}$, and $Mo_{0.45}Al_{0.55}N$–CrN, compare Figs. 1 and 3. When

adding the $Cr_{0.15}Al_{0.85}$ or $Cr_{0.40}Al_{0.60}$ cubes at the $Mo_{0.4}Al_{0.6}$ target, all quaternary coatings also contain the hexagonal phase, because their Al-content *x* is always above 0.6 (see for example Fig. 3a and b, representing the coatings prepared by alloying with $Cr_{0.15}Al_{0.85}$.

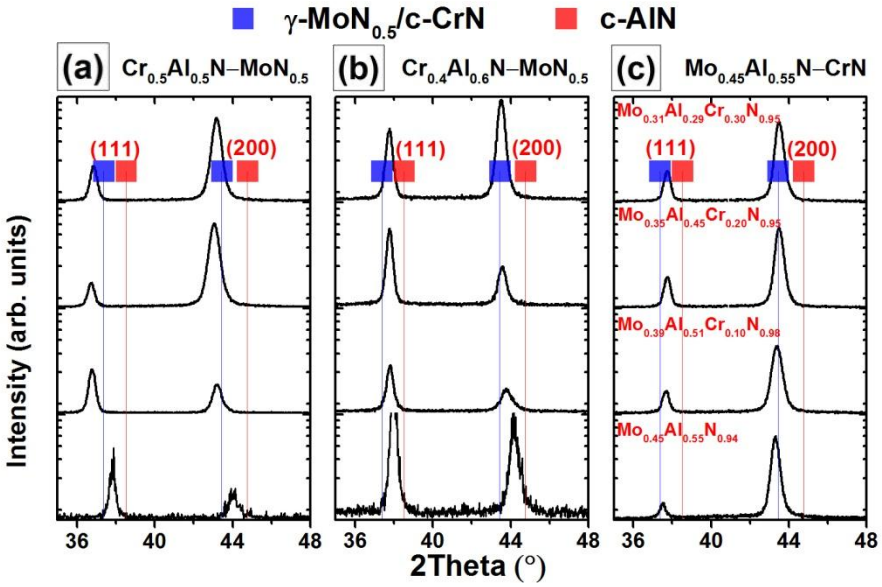

Fig. 2. The logarithmic scaled XRD patterns, revealing the phase composition of the cubic-structured quaternary Mo–Al–Cr–N coatings with the elemental composition developing along the quasi-binary tie lines $Cr_{0.5}Al_{0.5}N$–$MoN_{0.5}$ (a), $Cr_{0.4}Al_{0.6}N$–$MoN_{0.5}$ (b) $Mo_{0.45}Al_{0.55}N$–CrN (c). The indicated phases are c-$MoN_{0.5}$ (ICDD 00-025-1366), c-AlN (ICDD 00-046-1200). The characteristic c-CrN lines (ICDD 01-077-0047) are omitted by virtue of the similar lattice size with c-$MoN_{0.5}$. The break in the 2θ-range 67-71° hides the strong Si-substrate-reflex.

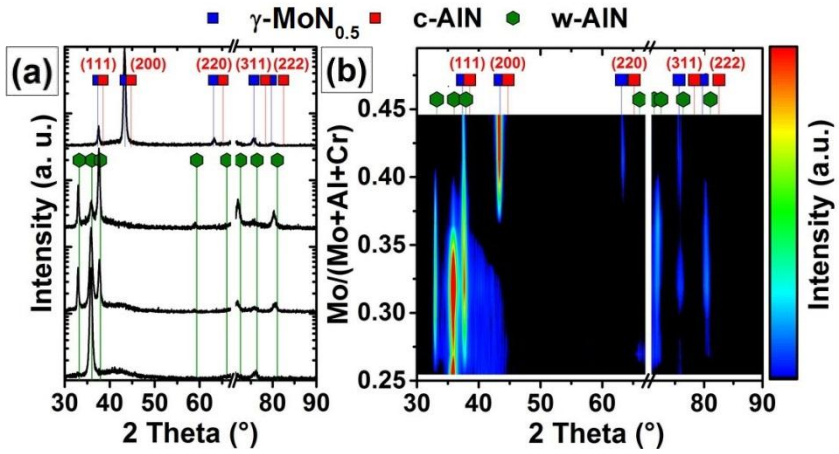

Fig. 3. XRD patterns (logarithmic scale) of coatings produced using $Mo_{0.4}Al_{0.6}$ target and $Cr_{0.15}Al_{0.85}$ cubes on its race track (a) and the intensity map composed of 7 XRD patterns. The indicated phases are c-$MoN_{0.5}$ (ICDD 00-025-1366), c-AlN (ICDD 00-046-1200), and w-AlN (ICDD 00-025-1133). The characteristic c-CrN lines (ICDD 01-077-0047) are omitted by virtue of the similar lattice size with c-$MoN_{0.5}$. The break in the 2θ-range 67-71° hides the strong Si-substrate-reflex.

The stress-free lattice parameter, a_0, correlates almost linearly with the Mo-content as well, but, in contrast to the N-content, is the smaller, the less molybdenum contains the solid solution $Mo_{1-x-y}Al_xCr_yN_z$ (Fig.4a). So, from the largest value of 4.177 ± 0.019 Å (γ-$MoN_{0.53}$), a_0

decreases to 4.112 ± 0.013 Å ($Cr_{0.47}Al_{0.53}N_{1.19}$) or 4.103 ± 0.016 Å ($Cr_{0.39}Al_{0.61}N_{1.11}$), when using $Cr_{0.4}Al_{0.6}$ and $Cr_{0.3}Al_{0.7}$ targets, respectively.

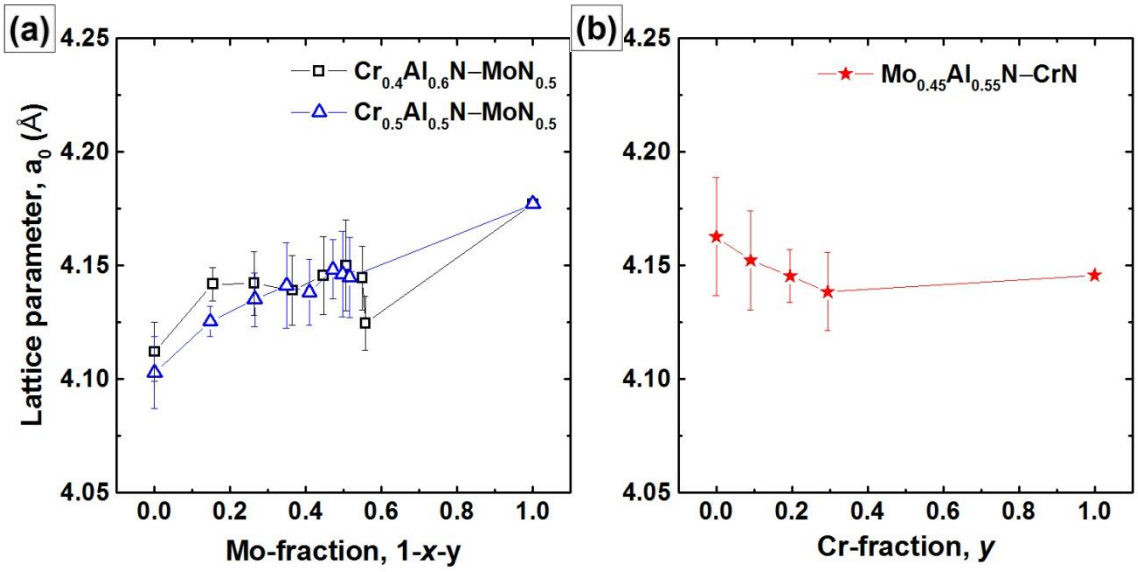

Fig. 4. The stress-free lattice parameter of quaternary Mo–Al–Cr–N coatings with the elemental composition, developing along the quasi-binary tie lines $Cr_{0.5}Al_{0.5}N–MoN_{0.5}$ and $Cr_{0.4}Al_{0.6}N–MoN_{0.5}$ (a), and $Mo_{0.45}Al_{0.55}N–CrN$ (b).

All single-phase cubic-structured quaternary $Mo_{1-x-y}Al_xCr_yN_z$ coatings exhibit indentation hardnesses, *H*, above 30 GPa (Fig. 5a). The lower values belong to coatings synthesized from the $Cr_{0.4}Al_{0.6}$ target, hence, coatings with low Al-contents, *x*, between 0.24 and 0.53 along the $Cr_{0.5}Al_{0.5}N–MoN_{0.5}$ tie line. Higher Al-contents in the target ($Cr_{0.3}Al_{0.7}$) and thus higher Al-contents in the coatings (*x* = 0.31 – 0.61), lead to significantly higher indentation hardnesses of our single-phase cubic-structured quaternaries of ~34-37 GPa, see Fig. 5a.

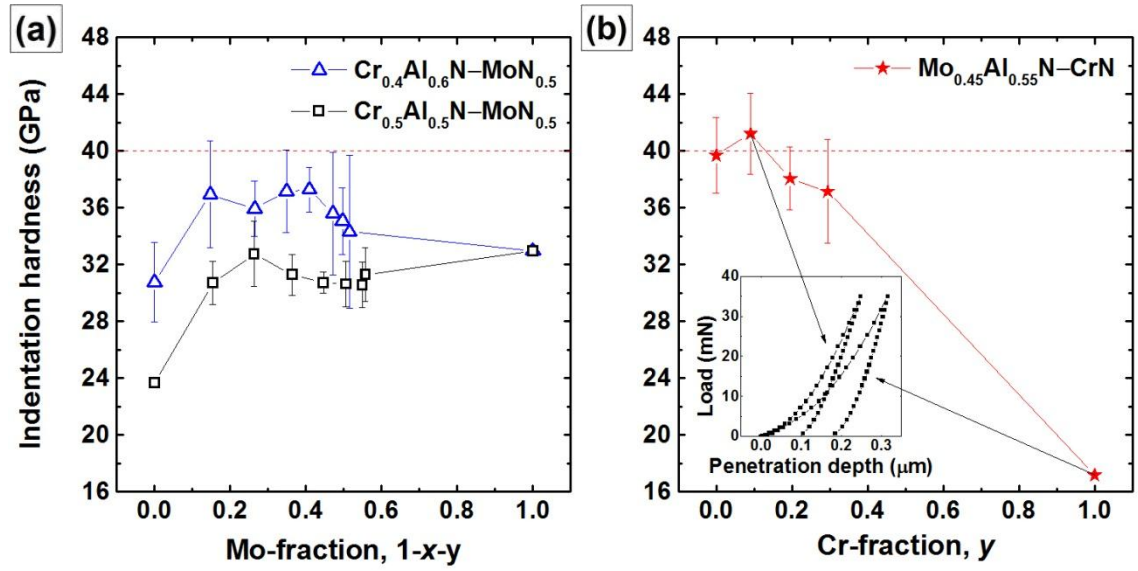

Fig. 5. Indentation hardness of quaternary Mo–Al–Cr–N coatings with the elemental composition, developing along the quasi-binary tie lines $Cr_{0.5}Al_{0.5}N–MoN_{0.5}$ and $Cr_{0.4}Al_{0.6}N–MoN_{0.5}$ (a), and $Mo_{0.45}Al_{0.55}N–CrN$ (b). The inset in the subfigure (b) illustrates the load-displacement curves at the maximum 35 mN load for the hardest and softest coatings, respectively.

When using the $Mo_{0.4}Al_{0.6}$ target – which has been developed by PLANSEE based on our previous *ab initio* and experimental studies [6] – and adding Cr-cubes, the hardness even increases to 41.2 ± 2.9 GPa for $Mo_{0.39}Al_{0.52}Cr_{0.09}N_{0.98}$. But also for the other compositions along this $Mo_{0.45}Al_{0.55}N$–CrN tie line, the hardnesses are around 40 GPa, Fig. 5b. Consequently, super-hard nitride coatings are accessible even without the formation of nanocomposites.

The quaternary coatings, prepared from the $Mo_{0.4}Al_{0.6}$ target with the addition of Al-containing cubes, have only hardnesses between 18 and 21 GPa, because they also contain the hexagonal Al-rich phase as their Al-contents, *x*, are always above 0.6.

The indentation moduli, *E*, (Fig. 5) show a similarly behaviour as the hardnesses. Also here, the indentation moduli are highest for the quaternary coatings along the $Mo_{0.45}Al_{0.55}N$–CrN tie line with low Cr-contents (which exhibit also the highest hardnesses). Generally, the Cr-rich cubic-structured solid solutions with *y* above 0.5 exhibit the lowest indentation moduli (300 – 400 GPa).

Many important mechanical and tribological properties are directly connected to the indentation hardness and elastic modulus, like strength and stiffness, respectively [13]. Generally, the abrasion wear is inversely proportional to hardness [16]. However, more useful are parameters including both, the hardness and elastic modulus, like: H/E, corresponding to elastic strain to failure [17], and H^3/E^2, corresponding to the resistance to plastic deformation [18]. High H/E and H^3/E^2 ratios can often be associated with a good wear resistance [17] and an improved toughness [16] of the coatings. In order to prevent brittle fracture, coating and substrate should be close in their elastic modulus [13]. Most of our single-phase cubic-structured $Mo_{1-x-y}Al_xCr_yN_z$ coatings possess H/E-ratios close to 0.08 or H^3/E^2-ratios close to 0.2. Slightly lower values are obtained for the Cr-rich compositions, Fig. 6a and b, but the Mo-rich quaternaries – deposited from the $Mo_{0.4}Al_{0.6}$ target with the addition of small fractions of Cr – reach H/E-ratios of 0.1 or H^3/E^2-ratios above 0.3. Especially, the hardest coating ($Mo_{0.39}Al_{0.52}Cr_{0.09}N_{0.98}$ with H = 41.2 ± 2.9 GPa) also exhibits the highest H^3/E^2-ratio of 0.36. Consequently, this super-hard material exhibits also the highest resistance to plastic deformation, H^3/E^2, which is often used to characterize ductility [16].

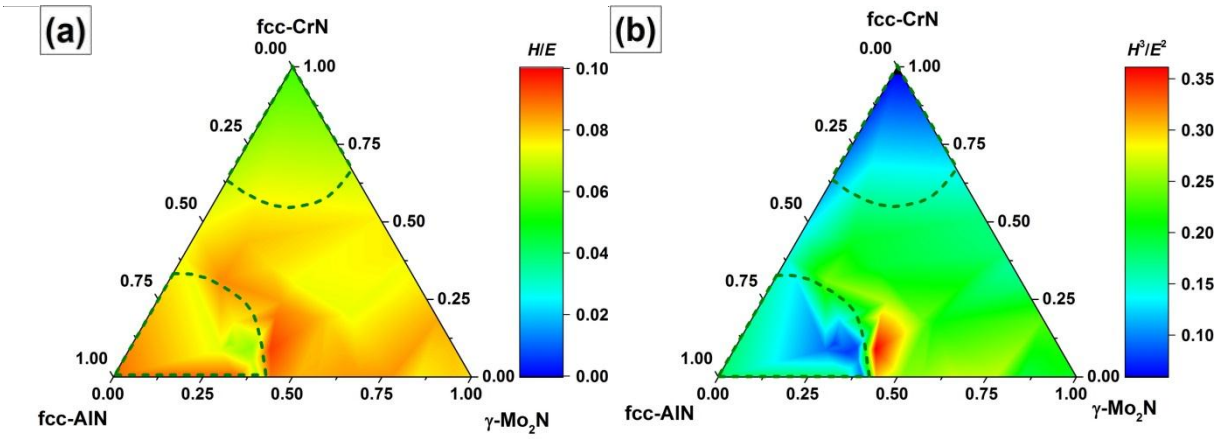

Fig. 6. The color-filled maps of H/E- (a) and H^3/E^2-ratios (b) composed of over 50 values for individual binary, ternary, and quaternary coatings within the Mo–Al–Cr–N system. The green dashed lines separate the regions of concentrations, where w-AlN-based coatings form.

IV. Summary and conclusions

Based on our recent *ab initio* and experimental studies of the binary system Mo–N, its ternaries Mo–Al–N and Mo–Cr–N, quaternary Mo–Al–Cr–N coatings were developed combining the single-phase cubic structure with high Mo- and Al-contents, superhardness ($H \geq 40$ GPa), and H/E ratios above 0.1.

Several single-phase cubic-structured quaternary Mo–Al–Cr–N coatings were developed with chemical compositions along the three quasi-binary tie lines $Cr_{0.5}Al_{0.5}N$–$MoN_{0.5}$, $Cr_{0.4}Al_{0.6}N$–$MoN_{0.5}$, and $Mo_{0.45}Al_{0.55}N$–CrN. When aiming for high Mo-contents, it is important to keep the N_2-partial pressure low during magnetron sputtering, as the vacancies at the N-sublattice stabilize the cubic structure of these nitrides. The hardest coatings are obtained with chemical compositions along the quasi-binary tie lines, $Cr_{0.4}Al_{0.6}N$–$MoN_{0.5}$, and $Mo_{0.45}Al_{0.55}N$–CrN, when Mo- and Al-contents are high ($x \geq 0.25$, $y \leq 0.25$ of the fcc-$Mo_{1-x-y}Al_xCr_yN_z$ phase).

If the Al-content, x, of the quaternaries is above 0.6, also hexagonal Al-rich phases are formed, leading to lower hardness values (down to 20 GPa). Such compositions were obtained by preparing coatings from the $Mo_{0.4}Al_{0.6}$ targets with the addition of $Cr_{0.4}Al_{0.6}$ and $Cr_{0.15}Al_{0.85}$.

The hardest coating among all quaternaries studied, is the single-phase cubic-structured $Mo_{0.39}Al_{0.52}Cr_{0.09}N_{0.98}$ with H = 41.2 ± 2.9 GPa. This even super-hard coating, which was prepared from a powder metallurgically prepared $Mo_{0.4}Al_{0.6}$ target with Cr-addition, also provides the highest H/E- and H^3/E^2- ratios of 0.1 and 0.36, respectively. The combination of these excellent mechanical properties with the high Al-content is a strong indicator for excellent performance during severe applications.

ACKNOWLEDGEMENTS

The financial support by the START Program (Y371) of the Austrian Science Fund (FWF) is gratefully acknowledged. The authors are thankful to the XRC, USTEM, and VSC of the TU Wien.

REFERENCES

[1] G. Gassner, P.H. Mayrhofer, K. Kutschej, C. Mitterer, M. Kathrein. Magnéli phase formation of PVD Mo–N and W–N coatings, Surface and Coatings Technology 201 (2006) 3335-3341.
[2] L. Toth. Refractory Materials, Transition Metal Carbides and Nitrides (vol. 7). San Diego, Academic Press, 1971.
[3] S. Veprek. Recent search for new superhard materials: Go nano!, Journal of Vacuum Science & Technology A: Vacuum, Surfaces, and Films 31 (2013) 050822.
[4] I. Blinkov, A. Volkhonskii, V. Anikin, M. Petrzhik, D. Derevtsova. Phase composition and properties of wear resistant Ti-Al-Cr-Zr-Nb-N coatings manufactured by the arc-physical deposition method, Inorganic Materials: Applied Research 2 (2011) 261-267.
[5] F.F. Klimashin, N. Koutná, H. Euchner, D. Holec, P.H. Mayrhofer. Computational and experimental studies on Mo–N hard coatings (manuscript in final preparation).
[6] F.F. Klimashin, H. Euchner, P.H. Mayrhofer. Computational and experimental studies on structure and mechanical properties of Mo–Al–N, Acta Materialia 107 (2016) 273-278.
[7] F.F. Klimashin, H. Riedl, D. Primetzhofer, J. Paulitsch, P.H. Mayrhofer. Composition driven phase evolution and mechanical properties of Mo–Cr–N hard coatings, Journal of Applied Physics 118 (2015) 025305.
[8] G. Greczynski, S. Mráz, L. Hultman, J. Schneider. Venting temperature determines surface chemistry of magnetron sputtered TiN films, Applied Physics Letters 108 (2016) 041603.
[9] D. Rafaja, C. Wüstefeld, C. Baehtz, V. Klemm, M. Dopita, M. Motylenko, C. Michotte, M. Kathrein. Effect of internal interfaces on hardness and thermal stability of nanocrystalline $Ti_{0.5}Al_{0.5}N$ coatings, Metallurgical and Materials Transactions A 42 (2011) 559-569.
[10] Y. Zhang, H.J. Whitlow, T. Winzell, I.F. Bubb, T. Sajavaara, K. Arstila, J. Keinonen. Detection efficiency of time-of-flight energy elastic recoil detection analysis systems, Nuclear Instruments and Methods in Physics Research Section B: Beam Interactions with Materials and Atoms 149 (1999) 477-489.
[11] W.C. Oliver, G.M. Pharr. An improved technique for determining hardness and elastic modulus using load and displacement sensing indentation experiments, Journal of materials research 7 (1992) 1564-1583.
[12] A.C. Fischer-Cripps. Critical review of analysis and interpretation of nanoindentation test data, Surface and Coatings Technology 200 (2006) 4153-4165.
[13] A.C. Fischer-Cripps. Nanoindentation, Springer, 2011.
[14] J.A. Thornton. High rate sputtering techniques, Thin Solid Films 80 (1981) 1-11.
[15] N. Laegreid, G.K. Wehner. Sputtering Yields of Metals for Ar+ and Ne+ Ions with Energies from 50 to 600 ev, Journal of Applied Physics 32 (1961) 365.
[16] X.-z. Ding, X. Zeng, Y. Liu. Structure and properties of CrAlSiN Nanocomposite coatings deposited by lateral rotating cathod arc, Thin Solid Films 519 (2011) 1894-1900.
[17] A. Leyland, A. Matthews. On the significance of the H/E ratio in wear control: a nanocomposite coating approach to optimised tribological behaviour, Wear 246 (2000) 1-11.
[18] T. Tsui, G. Pharr, W. Oliver, C. Bhatia, R. White, S. Anders, A. Anders, I. Brown. Nanoindentation and nanoscratching of hard carbon coatings for magnetic disks. MRS Proceedings, vol. 383: Cambridge Univ Press, 1995. p.447.

5.5. Vacancy-driven evolution of microstructure and mechanical properties of hard coatings along quasi-binary the tie-line Mo–N–Ta–N

Abstract

Recently we showed, that cubic structured Mo–N and Ta–N exhibit an inherent driving force for vacancies at the nitrogen and metal sublattices, respectively. To investigate their interaction and effects on mechanical properties, we have developed – based on *ab initio* calculations – ternary $Mo_{1-x}Ta_xN_z$ coatings. When using low N_2-partial pressures during reactive magnetron sputtering, single-phase cubic-structured solid solutions develop, with chemical compositions close to the quasi-binary tie line $MoN_{0.5}$–$Ta_{0.75}N$. However, the highest Ta-containing ternary $Mo_{1-x}Ta_xN_z$ coating (x = 0.76), also exhibits a small fraction of a hexagonal phase. Our *ab initio* results furthermore suggest, that for Ta-contents x below 0.55 within $Mo_{1-x}Ta_xN_z$, the formation of nitrogen-vacancies is energetically preferred. For higher Ta-contents, the formation of metal-vacancies is energetically preferred. This is also the critical Ta-content up to which the hardness *H* increases, from 31.4 ± 1.6 GPa for $MoN_{0.53}$ to 35.8 ± 2.5 GPa for $Mo_{0.45}Ta_{0.55}N_{0.81}$. Simultaneously, their indentation moduli *E* even slightly decreases (from 435 ± 27 GPa for $MoN_{0.53}$ to 414 ± 43 GPa for $Mo_{0.45}Ta_{0.55}N_{0.81}$). Consequently, their resistance against plastic deformation H^3/E^2 even increases to ~0.27. For higher Ta-contents (up to the maximum of x = 0.69 within the single-phase cubic-structured ternaries $Mo_{1-x}Ta_xN_z$ investigated), *H* and *E* decrease to 31.3 ± 3.8 GPa and 378 ± 29 GPa, respectively. Based on our results we can conclude, that by combining materials with a driving force for metal or nitrogen vacancies, both vacancy structures can be designed and thus also their mechanical and elastic properties.

Key words

Vacancies, Mo–Ta–N, hardness

Physical vapor deposition (PVD) techniques in combination with low substrate temperatures allow for the generation of various defects, metastable, supersaturated, and even thermodynamically instable structures. In particular vacancies – nearly present in any PVD processed materials (even to a very large extent) – significantly influenced structure and properties. But these important defects are extremely difficult to quantify experimentally [1]. However, the combination of computational and experimental materials science is an excellent tool in understanding the impact of vacancies on, e.g., phase stability and properties of (nonstoichiometric) transition metal nitrides [2, 3] or borides [4]. Motivated by the previous studies on the vacancy-rich substoichiometric nitrides (with nitrogen/metal-ratio <1) and our recent *ab initio* results within MoN_z and Ta_xN [5], which have an inherent driving force for nitrogen and metal vacancies, respectively, we have developed ternary $Mo_{1-x}Ta_xN_z$ coatings. The combination of computational and experimental materials science allows for deeper insights to the complex nature of this material system uniting both vacancy-type formers, MoN_z and Ta_xN, being rich in structural defects [6].

Here we focus, experimentally as well as computationally, on cubic-structured solid solutions. *Ab initio* obtained results of cubic structured $Mo_{1-x}Ta_xN_z$ – containing various point defects – are used to describe our coatings, prepared with low N_2-partial pressure during magnetron sputtering of Mo–Ta targets.

The MoN_z, Ta_xN, and the eleven different ternary $Mo_{1-x}Ta_xN_z$ thin films were synthesised using a modified magnetron sputtering system Leybold Heraeus Z400, in mixed Ar and N_2 dc glow discharges (both gases with purity above 99.999%). Mo-rich thin films were synthesised using a molybdenum target (99.97% purity, Ø75 mm) and placing various amounts of small Ta-discs (99.95% purity, Ø6 x 3 mm) at the race track. Correspondingly, the Ta-rich compositions were obtained by using a tantalum target (99.95% purity, Ø75 mm), where various amounts of small Mo-discs (99.97% purity, Ø5 x 3 mm) are uniformly placed at the race track. All depositions were prepared at a constant dc target current of 0.4 A, floating potential at the substrates (~ -15V), and constant substrate temperature of 450 ± 20 °C. Prior to every deposition process, the chamber was evacuated to a high vacuum of $p_{base} \leq 5 \cdot 10^{-4}$ Pa. During all sputter deposition processes the total pressure, p_T, of 0.35 Pa and nitrogen partial pressure, p_{N2}/p_T, of 0.32 were kept constant. Single-crystal silicon and austenite steel substrates were ultrasonically pre-cleaned in acetone and alcohol (for 5 minutes) and r.f. plasma etched using the following parameters: p(Ar) ≈ 2 Pa, 350 V, 50 kHz, 2656 ns. Before venting the deposition chamber, after each deposition processes, the substrates were cooled down below 100 °C, in order to minimize the surface chemistry alterations [7].

X-Ray diffraction was performed in symmetric Bragg-Brentano and asymmetric glancing angle (γ = 2°) geometries. The stress-free lattice parameters, a_0, and dimensions of the coherently scattering domains were obtained using $sin^2\psi$ method [8] and Williamson-Hall plot, respectively. The scanning electron microscopy (SEM) morphological investigations were performed using the Schottky emitter that results in the spatial resolution of ~2 nm. Energy dispersive X-ray spectroscopy (EDX) was used for chemical investigations of the coatings, quantification of the results is obtained with a Mo–N thin film standard that has been investigated by elastic recoil detection analysis [9]. The nanoindentation measurements were carried out with an UMIS equipped with a Berkovich diamond tip and a load range 3-45 mN. The evaluation of the film-only indentation hardness and modulus is given in details in Refs. [9, 10].

The calculated energies of formation for different vacancy-containing structures (Fig. 1a, μ_N = 0) suggest the preferred formation of vacancies at the metal sublattice, i.e., along the quasi-binary $Mo_{0.75}N$–$Ta_{0.75}N$ tie line. However, the binary MoN_z with 50% vacant N-sublattice (γ-$MoN_{0.5}$), as well as the binary $Ta_{0.94}N_{0.94}$ with Schottky defects (δ-$Ta_{1-z}N_{1-z}$), exhibit nearly the same low energy of formation. Based on the Schottky defects, i.e. vacancies at both sublattices, the same stoichiometry and charge neutrality is retained. When shifting the nitrogen chemical potential to negative values (μ_N = -0.5), which can be used to mimic N_2-poor conditions during sputtering [5], these binaries γ-$MoN_{0.5}$ and δ-$Ta_{1-z}N_{1-z}$ become energetically preferred, Fig. 1b. The results furthermore suggest (when using a linear interpolation between $MoN_{0.5}$ and $Ta_{0.75}N$, indicated in Fig. 1 by a dotted line) comparable energies of formation between compositions

along the quasi-binary tie lines $MoN_{0.5}$–$TaN_{0.5}$, $MoN_{0.5}$–TaN, $MoN_{0.5}$–$Ta_{0.94}N_{0.94}$ (with Schottky defects for TaN), and $MoN_{0.5}$–$Ta_{0.75}N$.

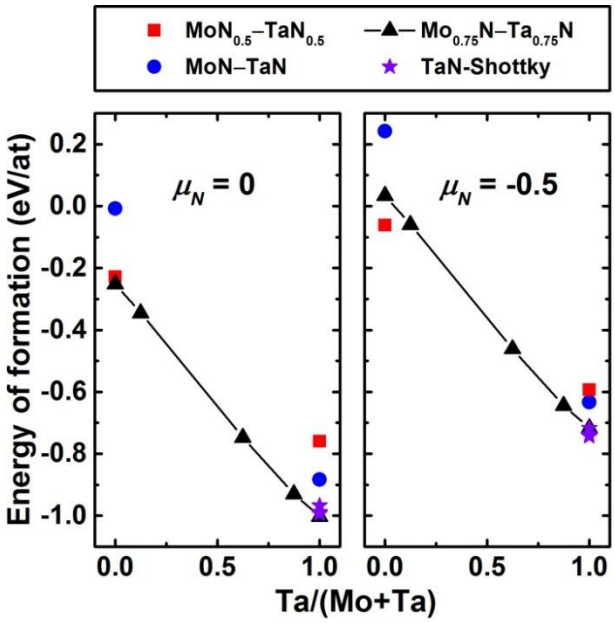

Fig. 1. Energy of formation of single-phase solid solutions $Mo_{1-x}Ta_xN_y$ with different defect structures as a function of the Ta/(Mo+Ta)-ratio and at varying nitrogen chemical potential from μ_N = 0 to -0.5.

The chemical composition of our $Mo_{1-x}Ta_xN_z$ coatings, sputtered in a low N_2-containing atmosphere, follows the quasi-binary $MoN_{0.5}$–TaN tie line for Ta/(Ta+Mo)-ratios, *x*, below 0.55, see Figs. 2a and b. Of course, the chemical composition gives no information about the vacancies formed and especially about the formation of Schottky defects. Consequently, chemically the quasi-binary $MoN_{0.5}$–TaN tie line is equivalent to $MoN_{0.5}$–$Ta_{0.96}N_{0.96}$.

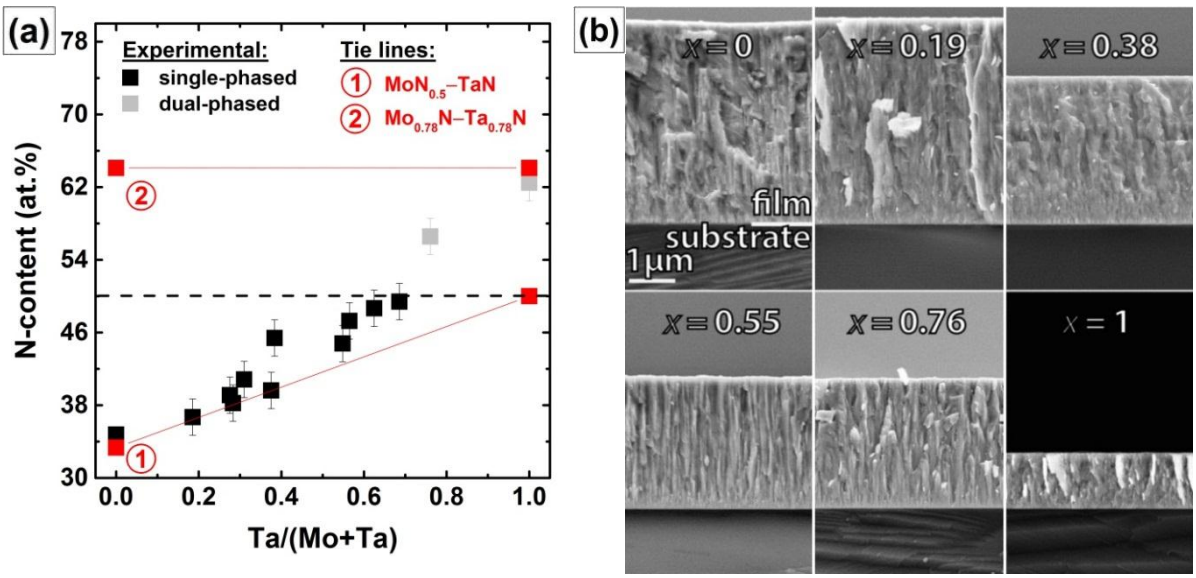

Fig. 2. EDX obtained N-content as a function of the Ta/(Mo+Ta)-ratio (a) and SEM fracture cross-sections of the significant $Mo_{1-x}Ta_xN_y$ coatings with x = 0, 0.19, 0.38, 0.55, 0.76, 1 (b).

All coatings prepared exhibit a dense columnar microstructure and smooth surface, Fig. 2b. With increasing Ta content the deposition rate decreases, especially for Ta-contents above x = 0.76 drastically.

XRD investigations, in Bragg-Brentano and glancing angle configurations, reveal the formation of cubic-structured solid solutions $Mo_{1-x}Ta_xN_y$ with preferred (200) orientation and fine coherently scattering domains (CSD) of ~23 ± 8 nm for Ta-contents x below 0.76, see the corresponding XRD patterns in Figs. 3a and b, respectively. For a Ta-content of x = 0.76, the maximum of our ternary $Mo_{1-x}Ta_xN_y$ coatings, also a small XRD peak for the hexagonal phase can be detected, especially when using glancing angle XRD, Fig. 3b. The Mo-free, binary TaN coating exhibits pronounced XRD peaks from hexagonal and cubic phases. The overall phase evolution of our $Mo_{1-x}Ta_xN_y$ coatings is presented by an intensity map composed of all XRD patterns recorded with Bragg-Brentano geometry, Fig. 3c.

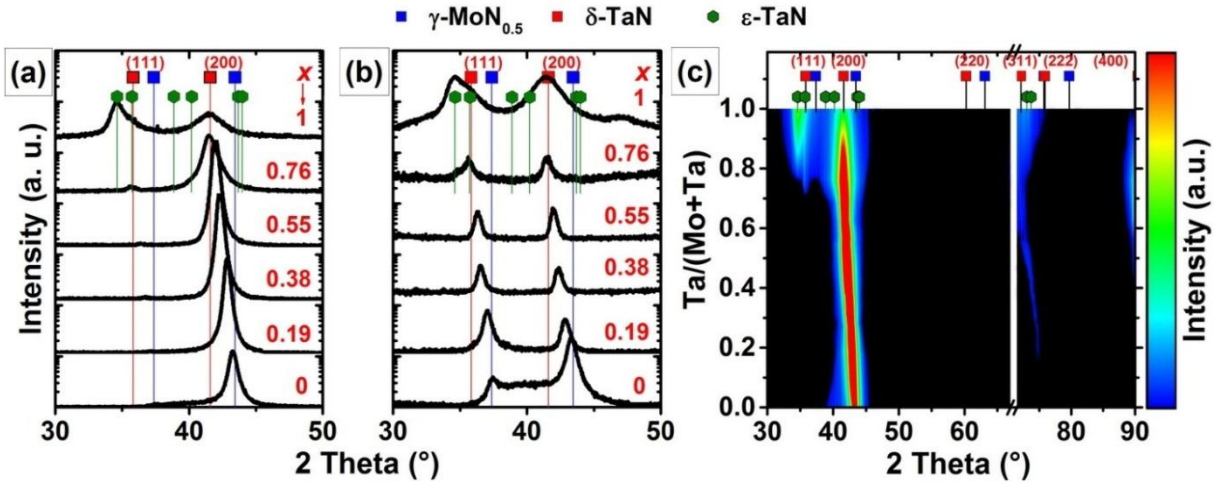

Fig. 3. XRD symmetric (a) and asymmetric (b) scan patterns of significant $Mo_{1-x}Ta_xN_y$ coatings and intensity map for symmetric scan, composed of 13 different $Mo_{1-x}Ta_xN_y$ coatings using linear interpolation function in between (c).

Our *ab initio* obtained lattice parameters for cubic-structured γ-$MoN_{0.5}$ and TaN binary nitrides, Fig. 4, are in excellent agreement with earlier reports, i.e. 0.420 nm (as compared to 0.420 nm [11]) for γ-$MoN_{0.5}$, 0.442 nm (0.442 nm [12]) for the defect-free TaN. Also $Ta_{0.94}N_{0.94}$, with ~6% Schottky defects, exhibits a comparable lattice parameter to the defect-free TaN.

The stress-free lattice parameter, a_0, of our $Mo_{1-x}Ta_xN_y$ solid solutions increases nearly linearly with increasing Ta-content x to 0.76, following the *ab initio* obtained a_0-values for cubic structures along the $MoN_{0.5}$–$Ta_{0.94}N_{0.94}$ quasi-binary tie line, Fig. 4, tie line 1. The experimentally obtained lattice parameter a_0 increases from 0.417 ± 0.002 to 0.436 ± 0.002 nm with increasing Ta-content from 0 to 0.76, respectively. The nearly constant overestimation with *ab initio* by ~0.8% is related to GGA [13], also reported recently for single-phase cubic-structured Mo–Al–N [14]. These results, in combination with the chemical composition suggest the increasing population of vacant N-sites (with nitrogen) when increasing the Ta-content up to x = 0.76. The formation of metal vacancies, which could also give a comparable variation in chemistry, would result in a much flatter lattice parameter variation with Ta, see tie line 2 in Fig. 4.

The highest Ta-containing $Mo_{1-x}Ta_xN_y$ coating (x = 0.76) exhibits also the largest lattice parameter of 0.433 ± 0.002 nm for the cubic phase.

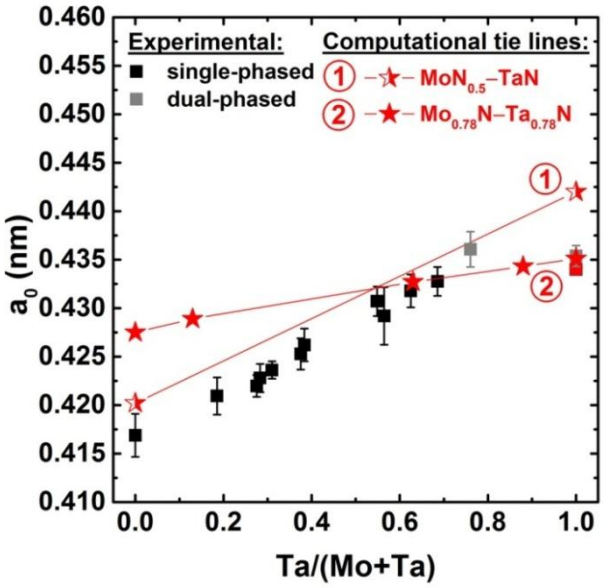

Fig. 4. Stress-free lattice parameter for the ternary $Mo_{1-x}Ta_xN_y$ solid solutions (black squares) and dual-phased Mo–Ta–N coatings (grey square) as well as *ab initio* obtained quasi-binary tie lines along $MoN_{0.5}$–$Ta_{1-y}N_{1-y}$ (1) and $Mo_{0.75}N$–$Ta_{0.75}N$ (2).

The indentation hardness of our coatings significantly increases to H = 35.8 ± 2.5 GPa with increasing Ta-content to x = 0.55. With a further increase in Ta content the hardness of our ternary $Mo_{1-x}Ta_xN_y$ coatings significantly decreases again to ~30 GPa. Only the binary Ta–N coating exhibits a higher hardness of 36.3 ± 5.3 GPa, see Fig. 5. However, the indentation modulus even slightly decreases from 435 ± 27 to 414 ± 43 GPa upon increasing the Ta-content up to 0.55. A further increase in Ta content of our ternaries leads to a more pronounced reduction to 378 ± 29 GPa Again, only the binary TaN exhibits again a higher indentation modulus of 440 ± 36 GPa.

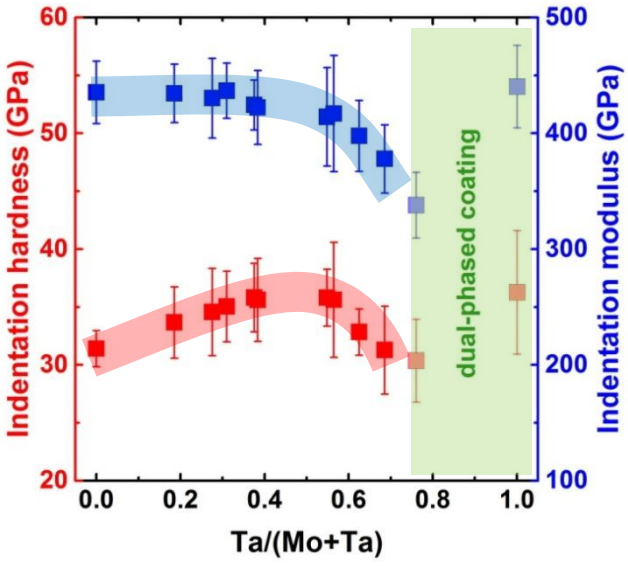

Fig. 5. Indentation hardness (red, left axis) and modulus (blue, right axis) of studied solid solutions $Mo_{1-x}Ta_xN_y$. The values for x = 0.69 and 1 are obtained from the dual-phased coatings.

Based on these dependences of hardness *H* and indentation modulus *E* with the Ta-content, in combination with the lattice parameter and chemical variations, we suggest that the single-phase cubic-structured $Mo_{1-x}Ta_xN_y$ coatings exhibit a different vacancy structure development. The Mo-rich compositions (for Ta-contents *x* below 0.55) are in favour of vacancies at the nitrogen sublattice where with increasing Ta-content also Schottky defects will form (as suggested by *ab initio*). Contrary, the Ta-rich compositions (for Ta-contents *x* above 0.55) also favour the formation of vacancies at the metal sublattice.

Consequently, the structure evolution within our single-phase cubic-structured $Mo_{1-x}Ta_xN_y$ solid solutions can best be described with the chemical formula $Mo_{1-x}Ta_xN_{0.5(1-x)}$, for Ta contents *x* below 0.55. In addition to this description, which is also reported for $Mo_{1-x}Cr_xN_{0.5(1-x)}$ [9], also Schottky defects are preferred. On the other hand, Ta-rich cubic compositions (Ta-contents *x* above 0.55) can best be described with the chemical formula $Mo_{0.75(1-x)}Ta_{0.75x}N$, indicating substitutions of the metal ions at the partially vacant metal sublattice.

Based on our previous *ab initio* and experimental reports, we developed single-phase cubic structured $Mo_{1-x}Ta_xN_y$ coatings up to Ta-contents of $x = 0.69$. For higher Ta-contents also the formation of hexagonal phases during PVD can be detected. The chemical compositions for Ta-contents $x \leq 0.55$ can best be described along the quasi-binary tie line $MoN_{0.5}$–TaN, whereas for higher Ta-contents the $MoN_{0.5}$–$Ta_{0.78}N$ tie line is approached. These results, in combination with the lattice parameter variation and mechanical properties suggest that the formation of nitrogen vacancies is preferred for $x \leq 0.55$. Higher Ta-contents favour the formation of metal vacancies. Up to this critical value of $x = 0.55$, the hardness increases to ~36 GPa for $Mo_{0.45}Ta_{0.55}N_{0.63}$ and the indentation modulus only slightly decreases from ~435 to ~414 GPa. Due to different dependence of *H* and *E* with increasing Ta-content, the hardest coating also exhibits the highest *H*/*E*-ratio among the coatings studied.

Our results clearly show the power of vacancy structures on structure stabilisation and mechanical properties. With the help of ternary $Mo_{1-x}Ta_xN_y$ coatings, along the MoN_z–Ta_xN system, both vacancy types (at the metal- or/and the nitrogen-sublattice) could be adjusted leading to coatings with excellent mechanical properties.

The financial support by the START Program (Y371) of the Austrian Science Fund (FWF) is gratefully acknowledged. The authors are thankful to the XRC and USTEM of the TU Wien.

References

[1] L. Toth. Transition Metal Carbides and Nitrides (Academic, New York, 1971), and references therein (1992) 87.

[2] F.F. Klimashin, H. Euchner, P.H. Mayrhofer. Computational and experimental studies on structure and mechanical properties of Mo-Al-N, Acta Materialia (2016).

[3] H. Euchner, P. Mayrhofer. Vacancy-dependent stability of cubic and wurtzite $Ti_{1-x}Al_xN$, Surface and Coatings Technology (2015).

[4] H. Euchner, P. Mayrhofer, H. Riedl, F. Klimashin, A. Limbeck, P. Polcik, S. Kolozsvari. Solid solution hardening of vacancy stabilized $Ti_xW_{1-x}B_2$, Acta Materialia 101 (2015) 55-61.
[5] N. Koutná, D. Holec, F.F. Klimashin, P.H. Mayrhofer. First-principle study on the energetic properties of point defects in cubic MoN and TaN (manuscript in final preparation), (2016).
[6] A.I. Gusev, A.A. Rempel, A.J. Magerl. Disorder and order in strongly nonstoichiometric compounds: transition metal carbides, nitrides and oxides, Springer Science & Business Media, 2013.
[7] G. Greczynski, S. Mráz, L. Hultman, J. Schneider. Venting temperature determines surface chemistry of magnetron sputtered TiN films, Applied Physics Letters 108 (2016) 041603.
[8] D. Rafaja, C. Wüstefeld, C. Baehtz, V. Klemm, M. Dopita, M. Motylenko, C. Michotte, M. Kathrein. Effect of internal interfaces on hardness and thermal stability of nanocrystalline $Ti_{0.5}Al_{0.5}N$ coatings, Metallurgical and Materials Transactions A 42 (2011) 559-569.
[9] F.F. Klimashin, H. Riedl, D. Primetzhofer, J. Paulitsch, P.H. Mayrhofer. Composition driven phase evolution and mechanical properties of Mo–Cr–N hard coatings, Journal of Applied Physics 118 (2015) 025305.
[10] A.C. Fischer-Cripps. Critical review of analysis and interpretation of nanoindentation test data, Surface and Coatings Technology 200 (2006) 4153-4165.
[11] H. Jehn, P. Ettmayer. The molybdenum-nitrogen phase diagram, Journal of the Less Common Metals 58 (1978) 85-98.
[12] R. Rachbauer, D. Holec, P. Mayrhofer. Phase stability and decomposition products of Ti-Al-Ta-N thin films, Applied Physics Letters 97 (2010) 151901.
[13] A. Khein, D.J. Singh, C.J. Umrigar. All-electron study of gradient corrections to the local-density functional in metallic systems, Physical Review B 51 (1995) 4105.
[14] F.F. Klimashin, H. Euchner, P.H. Mayrhofer. Computational and experimental studies on structure and mechanical properties of Mo–Al–N, Acta Materialia 107 (2016) 273-278.

6. Outlook

There are still a lot of open questions related to the functionality of the produced materials. Empirical criteria are excellent approach in material selection, though they have to be proved in every particular case, including our Mo-based nitrides. For instance, regarding the high-temperature applications, could the N–Mo bonds be strengthened? Do the vacancies with their (calculated) high activation energy for migration contribute to the thermal stability? Will the thermal stability furthermore improved due to rise of configurational entropy? Do the vacancies in Mo-based N-deficient materials lower also the thermal conductivity so that these materials can be treated as thermal barriers? Another question, if exposed to the oxide-containing atmosphere, do the dense oxide scales of Al_2O_3, Cr_2O_3, and complex oxides improve the material oxidation resistance? Or to prove, regarding the tribological behaviour, whether the high ionic potential φ will result in formation of shear-sensitive, lubricious oxides with low melting point (e.g. MoO_3, CrO_2) additionally to the lubricious Magnéli phases, allowing, hence, dry machining process. Another question arises here from the contradictory information, referring MoO_3 to either volatile oxides, easily vaporizing and leading to Mo-impoverishment, or lubricious oxide, contributing to the improved tribological behaviour. Regarding the predicted improved toughness for our super-hard quaternary nitride having VEC per unit cell of 9.4, will it be proved through a further empirical criterion, i.e., elastic constants G/B and C_{12}-C_{44}, as well as directly (experimentally), through fracture toughness measurements? And, finally, material performance under real conditions is of particular interest. Still, our results strongly suggest that molybdenum-based cubic-structured nitrides, and in particular the super-hard quaternary fcc-$Mo_{0.39}Al_{0.52}Cr_{0.09}N_{0.98}$, have high potential for various high-demanding applications.